Scholars' Mine

Summer 2013

A computational study of driven micro-cavities in supersonic flat plate flow

Thomas Ryan Rehmeier

Department:

A COMPUTATIONAL STUDY OF

DRIVEN MICRO-CAVITIES

IN SUPERSONIC FLAT PLATE FLOW

by

THOMAS RYAN REHMEIER

A THESIS

Presented to the Faculty of the Graduate School of the

MISSOURI UNIVERSITY OF SCIENCE AND TECHNOLOGY

In Partial Fulfillment of the Requirements for the Degree

MASTER OF SCIENCE IN AEROSPACE ENGINEERING

2013

Approved by

Dr. David W. Riggins, Advisor
Dr. Serhat Hosder
Dr. James A. Drallmeier

ABSTRACT

Driven micro-cavities embedded in the wall beneath turbulent supersonic boundary layers are analyzed using two-dimensional computational fluid dynamics. This concept is a passive flow control technique in which very small cavities formed by arrays of thin vertical walls are oriented transverse to the flow direction and underlie the boundary layer. The purpose is to reduce or eliminate skin friction drag. Various micro-cavity configurations were analyzed at locations (0.1 m and 1 m) downstream of the leading edges of flat plates, for free-stream Mach numbers of 1.2, 2.0, and 3.0. Results focus on net drag reduction achieved, cavity flow-field effects, perforation effects in vertical cavity walls, cavity scale effects, mesh refinement issues, and the stability of the solutions.

Skin friction drag was eliminated over micro-cavity regions for all configurations tested. Drag in these regions was due to pressure effects on vertical walls and exhibited a linear increase with downstream distance. Drag reductions as high as 18-20% (compared to a reference flat plate section) were obtained for 52-cavity geometries at Mach 2.0 and Mach 3.0 downstream of the 10 cm and 1 m flat plates, respectively. Perforation of the cavity walls showed no effect on net drag reduction for these cases. Stability issues were observed when using a fine grid mesh for the Mach 2.0 case, with significant oscillations seen in the drag. A parametric investigation in which cavity scale, number, and wall configuration were varied was also performed for two free-stream Mach numbers of 1.2 and 3.0. Drag reductions between 18-40% were seen for these cases. It is shown that drag reduction was reduced with increasing cavity length and that the steadiness of the solution increases with the number of vertical cavity walls present.

ACKNOWLEDGMENTS

The author would like to thank Dr. David Riggins for his invaluable guidance, expertise, and above all, patience in the completion of this work. Without his constant support and scheduling accommodations, timely completion of this work would not have been possible. The author's gratitude for Dr. Riggins' continued advice and friendship cannot be overstated. Further thanks go to Dr. Serhat Hosder and Dr. James Drallmeier for their contributions to the author's educational experience at both the graduate and undergraduate level and for serving on the committee to review this material.

Thank you to the Missouri University of Science and Technology Department of Mechanical and Aerospace Engineering for its financial support through the Graduate Teaching Assistantship.

Finally, thank you to my family and friends for their unwavering encouragement and support throughout this experience.

TABLE OF CONTENTS

LIST OF ILLUSTRATIONS

LIST OF TABLES

NOMENCLATURE

Symbol	Description
$c_{f,x}$	Local Skin Friction Coefficient
D	Drag
δ	Boundary Layer Thickness
H	Cavity Height
h	Perforation Height
L	Length of Simulation Domain
L_{LE}	Leading Edge Length
L_{TE}	Trailing Edge Length
M_∞	Free-Stream Mach Number
N	Number of Cavities
P_∞	Free-Stream Static Pressure
Re	Reynolds Number
T_∞	Free-Stream Static Temperature
u	Local Velocity in the X-Direction
U_∞	Free-Stream Velocity
w	Cavity Width
x	X-Distance from Initial Incoming Boundary Layer Profile
$x_{upstrem}$	X-Distance from Origin on Upstream Flat Plate
y	Y-Coordinate

1. INTRODUCTION

1.1. CONCEPT MOTIVATION

Concepts and techniques that can generate reductions in fluid dynamic drag are of significant interest for the design and optimization of future aerospace systems. Substantial decreases in the drag experienced by a vehicle, without incurring undue system penalties associated with the drag reduction, would provide attendant increases in vehicle performance and fuel economy, as well as potentially improved operability characteristics. Fluid dynamic drag generally comes from a combination of two sources: pressure drag (drag associated with pressure acting on the aerodynamic surfaces of an aerospace vehicle) and skin friction drag. Summation of the pressure drag and skin friction drag yields the net overall aerodynamic drag force acting on a solid surface.

The purpose of the present work is to investigate the feasibility of potentially reducing (or eliminating) turbulent skin friction drag on flat surfaces in supersonic flows by suitably tailoring the structural details of the surface, specifically by generating very small and successive fluid separation zones within micro-cavities embedded in the surface of the vehicle. These cavities are oriented transverse to the bulk fluid motion. Specifically of interest here is the performance of this concept in terms of potential drag reductions and stability characteristics for low to mid supersonic free-stream Mach numbers. A representative schematic of the concept investigated in the present work is shown in Figure 1.1.
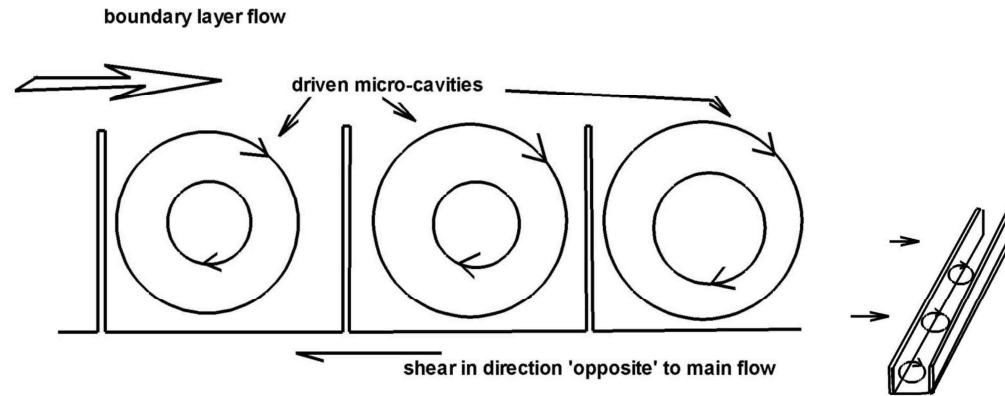
Figure 1.1. Driven Micro-Cavity Section Side View (Left) and Oblique View (Right) of a 3-D Cavity Channel

The cavities described have thin vertical walls with heights representing a small fraction of the boundary layer thickness. The boundary layer flow over these cavities then drives clockwise fluid vortices between these vertical cavity walls. In principle, these vortices will generate frictional forces acting in the direction opposite to that of the boundary layer flow. This has the potential to reduce or completely eliminate skin friction drag, or even generate a net contribution to thrust (skin friction drag becoming 'negative'). Frictional forces acting on the vertical cavity walls do not contribute to net drag since frictional forces on vertical surfaces do not act in the axial (drag) direction. As depicted in Fig. 1.1, the cavities are essentially successive parallel channels oriented in the direction transverse to the incoming flow. This simplifies the present work, as it allows two dimensional representations of the cavity and boundary layer flows for preliminary investigation.

Although the skin friction will in principle be much reduced (or even become 'negative') in such a concept, unfortunately, as the flow drives the clockwise vortices within the cavities, there will be inevitable variations in pressure within a given driven

cavity and from upstream cavity to adjacent downstream cavity. Specifically this pressure difference may be manifested across a given vertical wall, hence yielding a potential drag force. This phenomenon is depicted in Figure 1.2, where the net effect is shown as causing a pressure drag in the axial direction. This pressure-induced drag is a force component that would not be experienced by a simple flat plate at zero angle of attack.
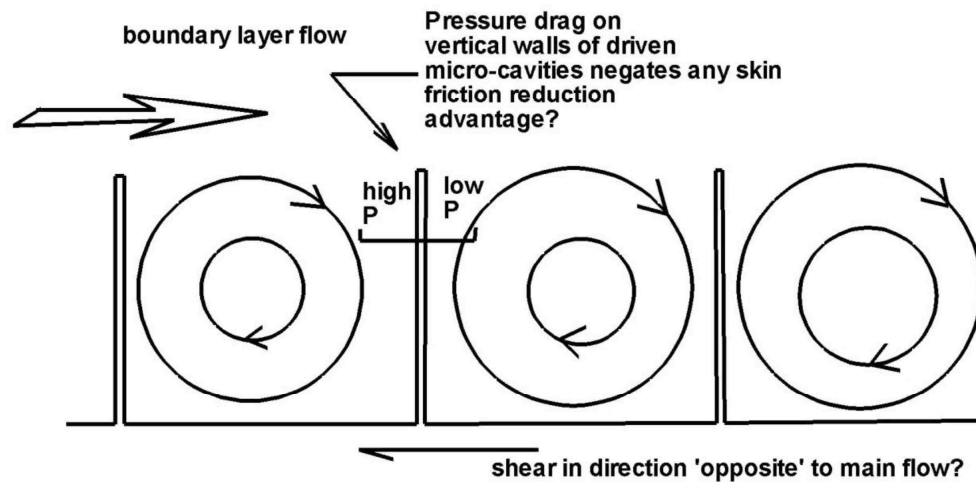
Figure 1.2. Schematic of Pressure Drag Generation on Vertical Cavity Walls

For the concept of driven micro-cavities as proposed in this investigation to be viable, the net overall drag experienced over the region of the plate as modified with embedded micro-cavities must be less than that of an unmodified flat plate of equal length. It is then essential to determine if the net pressure drag force experienced by the cavities outweighs the benefit of the skin friction reduction caused by the vortices, or vortex systems, associated with the cavities.

A specific technique for reducing the pressure drag associated with the cavities that is developed and investigated within the present work is to use perforations (slots) in the cavity walls, as shown in Figure 1.3. The purpose of such perforations would be to potentially promote fluid interaction between cavities, i.e., allow pressure equilibration between adjacent cavities, and hence provide reductions in the pressure component of drag over regions with cavities.

Another important consideration for the concept of driven micro-cavities for drag reduction is the stability, or lack of stability, for a boundary layer moving over a surface with embedded micro-cavities. Possible transient fluid interaction between the driven micro-cavity region and the boundary layer flow above it must not cause substantial (transient) instability in the boundary layer flow. Specifically, vortex shedding from the cavities and significant flow turning of the upper (above cavity) flow must be limited. Due to the fact that the cavities under consideration in the present concept are very small with respect to the boundary layer thickness, their role in terms of generating destabilization of the boundary layer is not definite. The present study provides some preliminary assessment of this issue.

The current investigation utilizes two-dimensional computational fluid dynamics (CFD) simulations of simplified geometries composed of smooth flat plates with embedded micro-cavity structures underlying supersonic turbulent boundary layers, in order to provide a parametric investigation into potential drag reductions associated with this concept and concept variations. Three different free-stream Mach numbers are considered; Mach 1.2, 2.0, and 3.0. Note that, in fact, a very large number of parameters are important in the characterization of this concept, including the cavity physical scale

with respect to the boundary layer, aspect ratio of the cavities, number of cavities, details of the extent of the cavity walls (perforated versus unperforated), upstream boundary layer development, etc. This study represents a preliminary feasibility study of the concept with a limited number of selected parameters varied and a limited number of concept variations examined. In addition, no considerations are made in the present study with regards to the manufacturability, cost, and/or weight and heat transfer penalties inevitably associated with embedded micro-cavities.
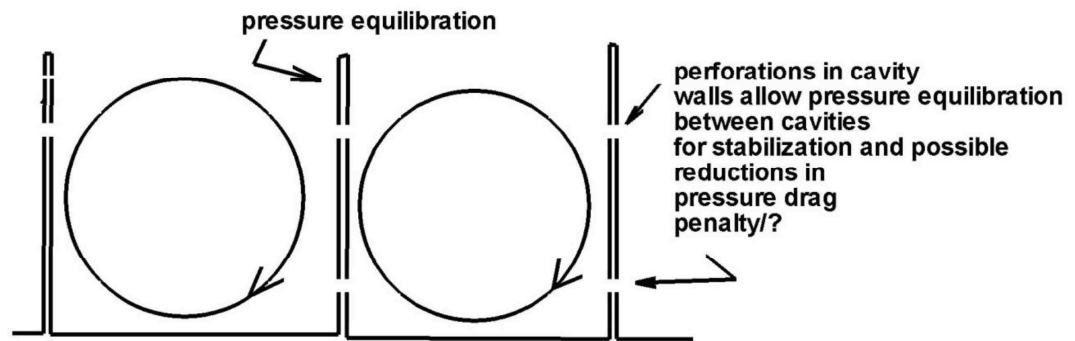
Figure 1.3. Schematic Showing Potential Effects of Perforating Cavity Walls

1.2. THESIS OUTLINE

This thesis is divided into seven main parts. First, Section 1 is the introduction and provides a general description of the concept investigated and a literature review of related work. Section 2 describes the CFD code, physical modeling, and methodologies used for this study and outlines the basic geometries studied, boundary conditions used, and geometric constraints, as well as describes the upstream marching simulations used to generate inflow boundary layer profiles for elliptic computational domains containing

micro-cavity geometries. In Section 3, a detailed study (in terms of discussion of flow physics, visualization, etc.) is conducted using a baseline grid for a 52-cavity geometry in which various cavity wall parameters are examined. This section provides results for two free-stream Mach numbers (Mach 2 and Mach 1.2) and compares drag performances of cavity configurations to that of an unmodified reference flat plate. Section 4 provides similar results for a single configuration with a large number of cavities, specifically a 208-cavity region at a free-stream Mach number of 2.0. Section 5 re-examines the test case presented in Section 3, except using a more refined mesh. Section 6, provides drag reductions (as measured from unmodified reference flat plates) and stability results obtained from a parametric investigation using mesh sequencing with coarse, baseline, and fine grids. Variations in cavity spacing, cavity region sizes, and other input parameters are examined in this section. This section provides results for free-stream Mach numbers of 1.2 and 3.0. Finally Section 7 provides a summary of the investigation and gives recommendations for future work.

1.3. LITERATURE REVIEW

A wide range of passive drag reduction techniques have been proposed, studied, and employed on fluid dynamic and aerodynamic surfaces, with significant emphasis in terms of applications involving aerospace vehicle design. However, such techniques have also been used in a wide variety of non-aerospace applications, including improving commercially available products. Passive drag reduction is also seen in natural biological systems. The classic example of passive flow control for a common application is the dimpling of a golf ball in order to induce turbulence, thereby reducing pressure drag

associated with separation. Examples of passive flow control devices in nature are seen on the wings of butterflies, as well as on the skin of sharks. Lang and Hidalgo[1,2] found that the bristled geometry of shark skin is capable of creating an interlocking web of vorticity, a web essentially composed of embedded vortices, that produces an effect similar to the dimples on the golf ball, hence reducing pressure drag associated with separation. In addition, the micro-geometry of the grooves/cavities in shark skin produces an effective slip velocity that increases momentum of the boundary layer flow near the skin and hence acted as a boundary layer control mechanism that results in a reduction in skin friction drag. Hao et al.[3] experimentally investigated laminar drag reduction in hydrophobic micro-channels and found decreases in channel pressure of up to 30% with effective slip velocities reaching 10% of the centerline velocity in the channel.

Another passive drag reduction technique extensively investigated is the use of riblets, i.e. raised ridges aligned in the direction of the flow, as depicted in Figure 1.4. Walsh[4] provides a very comprehensive study in the use of riblets as a method of viscous drag reduction in boundary layers. Shark skin also exhibits riblet-like configurations. Work with riblets in high-speed flows has also been conducted by Duan and Choudhari[5]. The maximum total drag reduction (compared to a reference flat plate) using riblets has been observed to be between 4-8% in these and most other riblet studies. The essential mechanism behind the drag reduction obtained using riblets is still under investigation but is usually attributed to a suppression in lateral transport of near-wall streamwise vortices, which in turn reduces effective turbulent shearing at the surface.
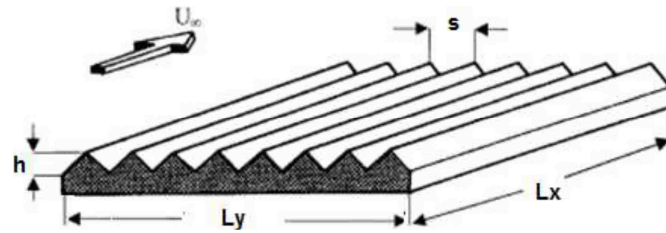
Figure 1.4. Riblets Geometry Aligned in the Direction of the Flow[5]

Active flow control techniques such as micro-blowing, supersonic micro-jet injections, and controlled energy injections, have been used to reduce drag and suppress unsteadiness and resonance issues, delay separation, etc. in flow over cavity and cavity-like geometries, generally larger than of interest in the current work. The reader is directed to the studies of Hwang[6], Zhuang et al.[7], and Lazar et al.[8] for further information regarding active flow control in such flows.

Several investigations have been conducted using thick blocks arranged transverse to the flow, shown in Figure 1.5, as opposed to utilizing thin cavity walls as proposed in the current work. Wang[9] analyzed slip coefficients for cavities with such finite-thickness cavity walls. His findings indicated that for the highest slip (lowest resistance) shallow cavities were better in terms of reducing drag, and he notes that this is somewhat contrary to intuition that would seemingly indicate that deep cavities would produce the most slip. Huang[10] , in a similar geometry, found that the flow is decelerated in the inter-block regions and eventually forced to reverse near the wall, resulting in overall separation of the flow.
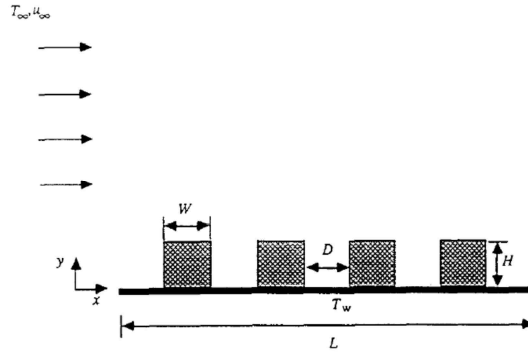
Figure 1.5. Finite-Thickness Porous Cavity Blocks[10]

Subjects of further passive drag reduction techniques include flow over plates that include embedded shapes or have roughened surfaces. Hwang's[11] work analyzed subsonic flow over a plate with circular holes of various sizes, orientations, and patterns, shown in Figure 1.6. The study found that turbulent skin friction was most effectively reduced for holes with a 0.6 aspect ratio oriented at 15° from the flow direction. Ekoto et al.[12] examined the effect of large scale roughness for supersonic boundary layers over 3-D plates with raised squares, noting the dominance of a pressure force acting in the x-direction. Lang and Melnick[13] conducted another experimental study of both laminar and turbulent flow over embedded hexagonal shaped cavities, depicted in Figure 1.7. Partial effective slip increased up to 30% in the cavities and increases in momentum of the fluid acted as a passive separation control mechanism. A patent was also awarded to Lang[14] for this surface patterning technique.
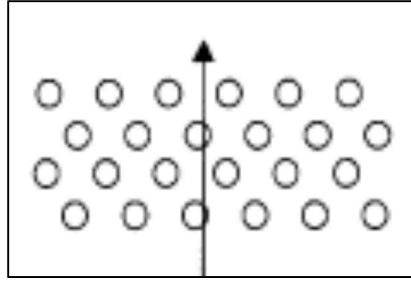
Figure 1.6. Flat Plate with Holes in Flow Direction[11]
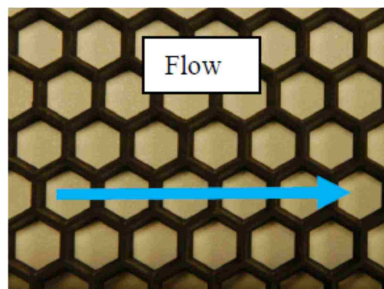
Figure 1.7. Embedded Hexagonal Shaped Cavities[13]

Previous works most closely related to the present work include the use of cavities in a transverse orientation to the flow. Gatski and Grosch[15] performed a computational of steady laminar and incompressible flow over a single embedded cavity, as shown in Figure 1.8. Results obtained showed negligible reduction in drag for the single cavity when compared to a flat plate; however, the presence of an embedded vortex contributed to an overall favorable pressure gradient from the cavity. It was postulated in this study that multiple cavities have the potential to reduce drag provided such cavities are optimally spaced and sized.
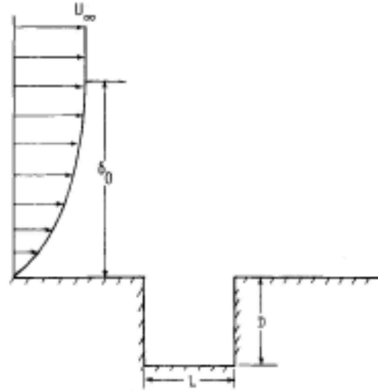
Figure 1.8. Boundary Layer Flow Over an Embedded Cavity in Transverse
Orientation to the Incoming Flow[15]

Umazame et al.[16] obtained a patent for the concept of using cavities and grooves as a passive drag reduction technique closely related to the current study. A schematic of the general physical principle is shown in Figure 1.9. The flow on the bottom of the cavity is reversed, i.e., flowing in the opposite direction of the boundary layer flow. This reversal in the velocity profile generates a reduction in the skin friction drag. A numerical study by Madi-Arous et al.[17] analyzes the reattachment phenomenon of flow entering and exiting the cavity and found that three zones of recirculation exist in each cavity, the primary one behind the upstream step and two secondary zones located in the bottom corners.

B : Body
x : Flowing Direction of Fluid
S : Surface
M: Groove
R : Reversed Flow
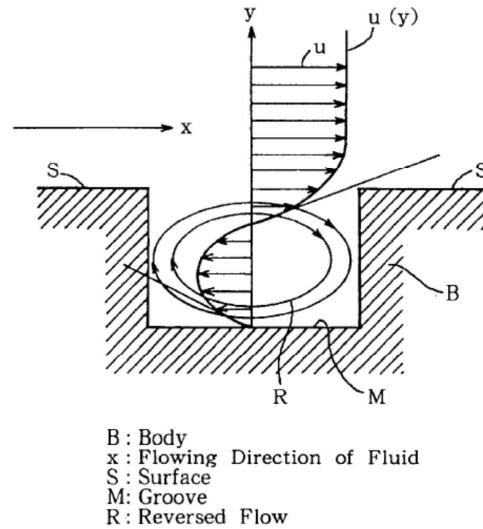
Figure 1.9. Schematic of Velocity Profile with Reversal in Flow at the Bottom of the Embedded Cavity[16]

Lang and Hidalgo[18] performed both experimental and computational tests on an embedded cavity region with multiple cavities with thin walls in very low speed flow. A reduction in drag coefficient was sustained over the first eight cavities, but no additional investigation of reductions for any longer lengths was done. Instabilities in the flow were observed near the fourth and fifth cavities during experimental testing that weren't seen in computational tests.

A recent work in cavities in transverse orientation to the flow was conducted by Leibenguth[19]. This work modeled 2-D Couette flow over single-embedded cavity geometries with various inclination angles of the cavity walls. Very low speed flows were considered with $0.01 \leq Re \leq 100$. This work found that regardless of the cavity wall aspect ratio or inclination angles, the drag reduction potential decreased with lower Re. Further, as the distance between the bounding top plate and the cavity region increased, the drag reduction potential decreased. Leibenguth's work, however, did not include any

results for external flow, only internal Couette flow. He concludes that future work is needed in exploring boundary layer flow over multiple embedded cavities.

1.4. SCOPE OF PRESENT WORK

The present study examines two-dimensional supersonic external turbulent flow over multiple wall-embedded thin-walled micro-cavities aligned in the transverse direction to the flow. This investigation differs from previous works in that it is believed to be the first study focusing upon high-speed (supersonic Mach number) boundary flows over such multiple micro-scaled cavities. Furthermore, a concept is investigated here in which the cavity walls are perforated in order to attempt to control and equilibrate pressure and flow patterns inside the cavity region. The primary objective of the present work is to provide information on whether such driven micro-cavities may be able to potentially produce effective drag reductions on surfaces in high-speed flow without significantly destabilizing the outer boundary layer flow. In addition, the effects of perforating cavity walls are of interest in terms of potentially reducing drag, increasing flow stabilization associated with embedded micro-cavities, and allowing the tailoring of the circulatory patterns within the micro-cavity region.

2. CFD TOOLS, METHODOLOGY, AND PROFILE DEVELOPMENT

2.1. VULCAN CFD CODE

All CFD results presented in this work were generated using the VULCAN (Viscous Upwind ALgorithm for Complex Flow ANalysis) code version 6.2.0.[20] VULCAN is a turbulent, non-equilibrium, chemically reacting Reynolds Averaged Navier-Stokes solver maintained by the NASA Langley Research Center. VULCAN utilizes structured, cell-centered grids and has a wide variety of user-selected options for marching simulations and for performing fully elliptic simulations, including the ability to solve using either local time-stepping or time accurate capability. It includes multi-grid and mesh-sequencing options, with the latter used extensively in the current investigation. VULCAN was used in the current study to provide both upstream marching (flat plate) boundary layer simulations and the main (downstream) fully-elliptic two-dimensional Navier-Stokes simulations for regions with embedded cavities. VULCAN has multi-block capability for facilitating parallel computations; this capability was used extensively in the current study. This code has been extensively validated on a wide range of applications, although it has been primarily utilized (and developed for) the high-speed flight regime. All simulations in the current work used the Roe flux difference scheme with third order upwind-biased MUSCL interpolation parameter kappa = 1/3 and a smooth limiter. For non-time-accurate computations (local time-stepping), a Distributed Approximate Factorization (CFL based) scheme was used; for time accurate computations, a DAF dual-time stepping scheme was utilized. Marching simulations employed DAF with manual sub-stepping.

All simulations presented in this work used the Menter Shear Stress Transport (Menter-SST) k-omega model[21,22], a two-equation eddy-viscosity turbulence model. The Menter-SST model provides a blending treatment for the turbulence such that there is realization of the benefits of a k-ω model for near-the-wall calculations while blending into the k-ε model for the outer flow. This turbulence model has been used successfully in a wide range of studies and for various flow-fields, including boundary layer studies at moderate and high speeds, and for flows with separating boundary layers. Simulations used a free-stream turbulence intensity of 1%.

Since the grid was extremely refined spatially (due to small physical scale of domain of interest which was essentially just the boundary layer and the underlying driven micro cavity regions), this study did not use available wall matching functions (i.e. the 'solve to the wall' option was utilized). Typical y+ values through most of the domain are very small (much less than 1.0). Primary interest in the current study was to simply generate representative turbulent boundary layer profiles providing wall shear for use in providing inflows into driven micro-cavity domains. Additionally, due to the very small vertical scale of the micro-cavities underlying the boundary layer, the impact of the turbulence model within the elliptic domain itself is minimal in terms of defining the very low velocity flow in the cavities themselves, at least over the lengths studied here. Essentially the typical problem in the current study was characterized by a flat plate turbulent boundary layer moving with minimal disturbance over the top of the driven cavity regions, which themselves are very short in length (for most of the geometries examined).

Inflow air was simulated as a thermally perfect gas mixture composed of 76.86% N_2 and 23.14% O_2 (by mass). Input free-stream Mach number and ambient temperature and pressure conditions varied by case study and are defined in subsequent sections. An example of a VULCAN input deck for a micro-cavity region test case is provided in Appendix A.

Degree of temporal convergence for the simulations over cavity regions was monitored primarily by examining computed drag against iteration on the finest grid level tested; it was observed that cases that converged to a single unvarying drag level utilizing local time-stepping did not change their convergence characteristics when time accurate simulations were subsequently utilized. Note, however, that some cases examined did not exhibit steady convergence, as will be discussed in following sections, with refined grids exhibiting the greatest tendency to be unsteady or oscillatory. Cases that exhibited steady convergence in terms of drag value (and hence were of greatest interest in the current study) generally displayed eight or more orders of magnitude reduction of the L2 norm of the residual; cases that oscillated about a fixed drag value generally displayed two or three orders of magnitude reduction at most.

The internal utilities within the VULCAN tool suite were used to directly monitor time (iteration) history of drag on the geometries examined; also produced by VULCAN and used extensively is a spatial descriptor of pressure and skin friction drag on a given geometry.

2.2. UPSTREAM TURBULENT BOUNDARY LAYER GENERATION

In order to generate the incoming flow profiles for the test geometries (regions with embedded cavities), upstream turbulent boundary layers were simulated by generating flow over simple flat plates. The flat plate geometry was taken to be an adiabatic wall at zero angle of attack. Due to the parabolic nature of boundary layer growth and the simplicity of the flow and geometry, a space marching scheme was used for all upstream simulations. This solution approach requires far less computational time than the solution of full elliptic Navier-Stokes equations. Four boundary layer profiles were created for testing, as outlined in Table 2.1, with varied upstream flat plate length, free-stream Mach number, and ambient temperature and pressure. The height of the solution domain for profiles US1 and US2 is very slightly less than 0.002 m, since the flat plate bottom wall for the upstream marching simulations is located at a height corresponding to the height of the micro-cavities in the downstream elliptic domains which is very small compared to overall solution domain height, as discussed subsequently. Profiles US3 and US4 required an increased height of very slightly less than 0.02 m in order to completely capture the boundary layer present over the longer upstream flat plate region modeled for those cases.

Table 2.1. Upstream Flat Plate Case Configurations

Profile	Length [m]	M_∞	T_∞ [K]	P_∞ [N/m^2]
US1	0.1	2.0	288	101,325
US2	0.1	1.2	288	101,325
US3	1.0	1.2	223	26,500
US4	1.0	3.0	223	26,500

VULCAN is able to make use of multiple processors while running a solution for a given single geometry. Each upstream flat plate case was broken up into four blocks stacked in the y-direction. The blocks were configured in this manner to most effectively make use of the parallel computing abilities of VULCAN while using the marching solution scheme. Stacking blocks in the axial (x-direction) would serve no purpose in a multi-grid parallelization strategy using a marching solution. Figure 2.1 and Figure 2.2 show the multi-block configuration used for the L = 0.1 m cases and L = 1.0 m cases, respectively. Note that the grid was equally spaced in the y-direction for the L = 0.1 m cases while it was clustered at the wall boundary for the L = 1 m cases, due to the thicker boundary layer over the embedded cavity regions modeled. The outflow profile from each block was then exported to become the fixed input (inflow) profile for the elliptic domains containing embedded cavities.
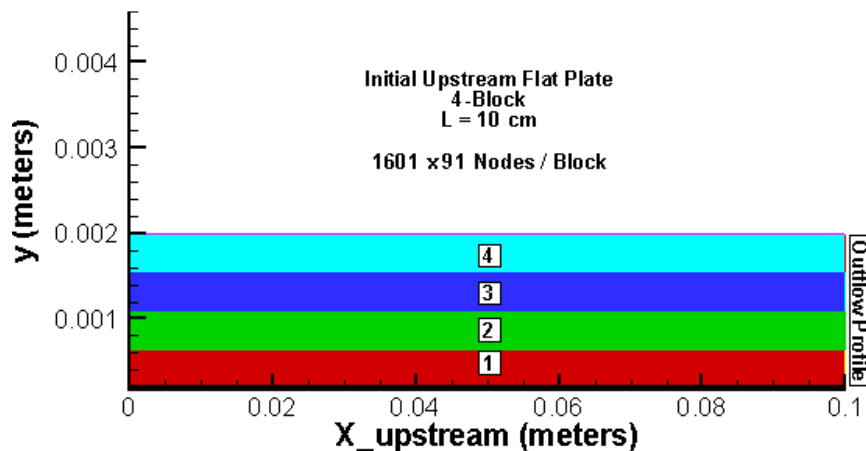
Figure 2.1. Multi-Block Configuration for L = 0.1 m Initial
Upstream Flat Plate Profile
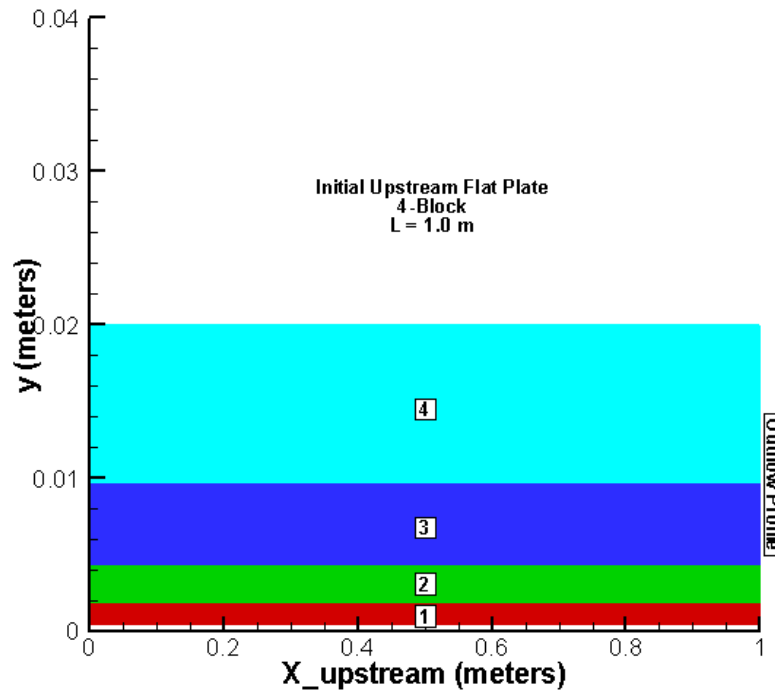
Figure 2.2. Multi-Block Configuration for L = 1.0 m Initial
Upstream Flat Plate Profile

A representative visualization of the resulting boundary layer flow is given in Figure 2.3. The profile shown is Profile US1 with a total length of 0.1 m (10 cm) with M_∞ = 2.0 flow. The Reynolds number for flow over the flat plate based on the total length is ~4.65 x 10^6. Despite the flow shown in Figure 2.3 not being a fully developed boundary layer, the output from the profile provides a reasonable simulation of a turbulent boundary layer to act as the inflow condition for subsequent simulation of the elliptic micro-cavity region.
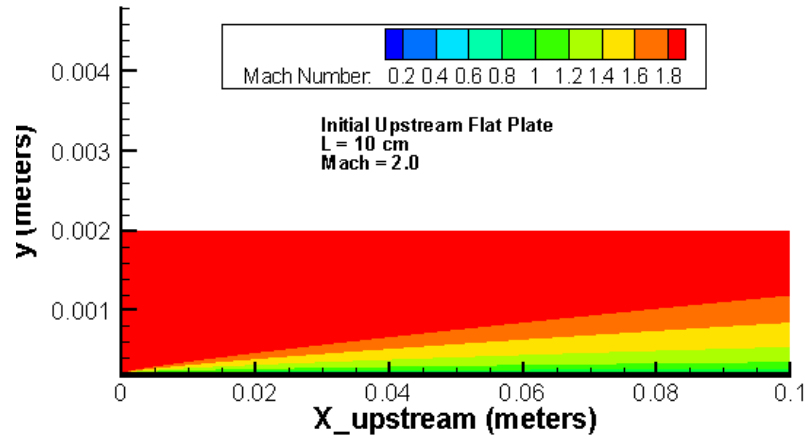
Figure 2.3. Mach Contours for Initial Upstream Flat Plate Flow Profile US1

Boundary layer thicknesses (the vertical distance between the flat plate to the point in the flow at which $u = 0.99U_\infty$) and the local skin friction coefficient values were tabulated at the $x_{upstream} = L$ location for the four upstream flat plate profiles and are presented in Table 2.2. As expected the boundary layers for the 1.0 m flat plate are significantly thicker than those for the 0.1 m flat plate. The c_f values obtained are between 6-12% higher than the theoretical values obtained using the relations in Schetz[23]. The reason for the discrepancy may lie in the scatter in data present in the empirical relations developed to provide a correlation between compressible and incompressible local skin friction coefficients, but needs to be studied in future works.

Table 2.2. Boundary Layer Thicknesses and Local Skin Friction Coefficients

Profile	δ [m]	$c_{f,x}$ (simulation)	$c_{f,x}$ (theoretical)
US1	0.001465	0.002317	0.002060
US2	0.001635	0.002937	0.002708
US3	0.012449	0.002219	0.002085
US4	0.011365	0.001372	0.001170

2.3. MICRO-CAVITY REGION GEOMETRY AND BOUNDARY CONDITIONS

This section describes the general geometric configuration of the domains used in the present study that contained embedded driven micro-cavities. All driven micro-cavity regions simulated in this work used the same general domain configuration. This consisted of a flat plate leading edge region (downstream of the outflow from the upstream marching simulation discussed in the previous section, but upstream of the region with cavities) of length L_{LE}, the cavity region itself, and finally a flat plate trailing edge of length L_{TE} (downstream of the cavity region). This allowed fully elliptic simulations of the modeled domains that sufficiently captured any upstream interactions, as well as the smooth flat plate boundary layer 're-establishment', downstream of the cavity region itself. Length of the cavity region is given in terms of N-cavities of small, medium, or large width, (width designated as w), as described below. The embedded cavity region is recessed a height (H) below the level of the upstream/downstream flat plate section bottom boundary. For all work done in this study, the ratio of cavity height to cavity width, H/w was kept constant at 4.0 (i.e., the vertical-to-horizontal aspect ratio of the cavity regions are always 4.0). This aspect ratio is based on defined individual 'cavity regions,' even for parametric studies which removed vertical walls between adjacent cavities, i.e., the effective aspect ratio from the standpoint of distance between bounding vertical walls (to cavity height) can be less than 4.0, depending on the number of 'removed' walls. However, the nominal aspect ratio based on cavity 'regions' (defined by blocks utilized within the solution procedure) always remains at 4.0, as stated. The top of each vertical cavity wall is flush with the leading and trailing flat plate sections. Actual vertical extent of the cavity walls themselves is dictated by the value of the perforation

height (h), corresponding to the distance between the bottom wall of the cavity region and the bottom edge of the cavity wall. Figure 2.4 provides a schematic of the general test case geometry with all significant measurement parameters.

There are three cavity physical scales utilized for various cases discussed in the present investigation. As noted previously, default aspect ratio of the cavities (or the defined individual cavity regions for parametric studies with 'removed' walls) is kept at 4.0. However, various test cases are considered utilizing 'small width' cavities, corresponding to H = 0.0002 m (such that cavity width, w, is 0.00005 m). 'Medium width' cavities correspond to H = 0.0005 m (such that cavity width, w, is 0.000125 m). 'Large width' cavities correspond to H = 0.002 m (such that cavity width, w, is 0.0005 m).
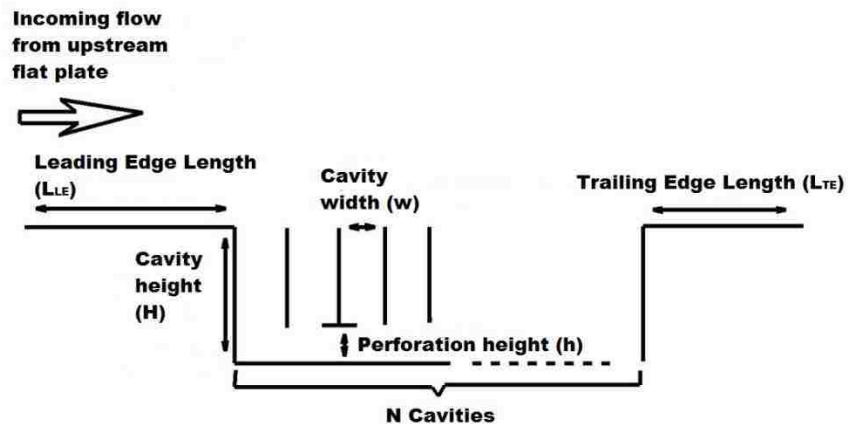
Figure 2.4. General Geometry for Driven Micro-Cavity Test Cases

For the purposes of diagraming the boundary and cut conditions, as well as the parallelization strategy used, the 52-cavity (N = 52) small width baseline grid test geometry is used as a representative example in the following discussion. Figure 2.5 shows that the 52-cavity setup is divided into 55 blocks to maximize parallel processing capabilities. Blocks 1, 2, and 55 (or N + 3 for the general case) include only the leading and trailing edge flat plates. There is always one block per individual cavity region, extending from bottom cavity wall to top boundary as shown, over the region of the domain with embedded cavities. This is true even in cases where cavity walls between adjacent cavities have been 'removed', in order to study the impact of internal walls on flow-field and drag reductions obtained.
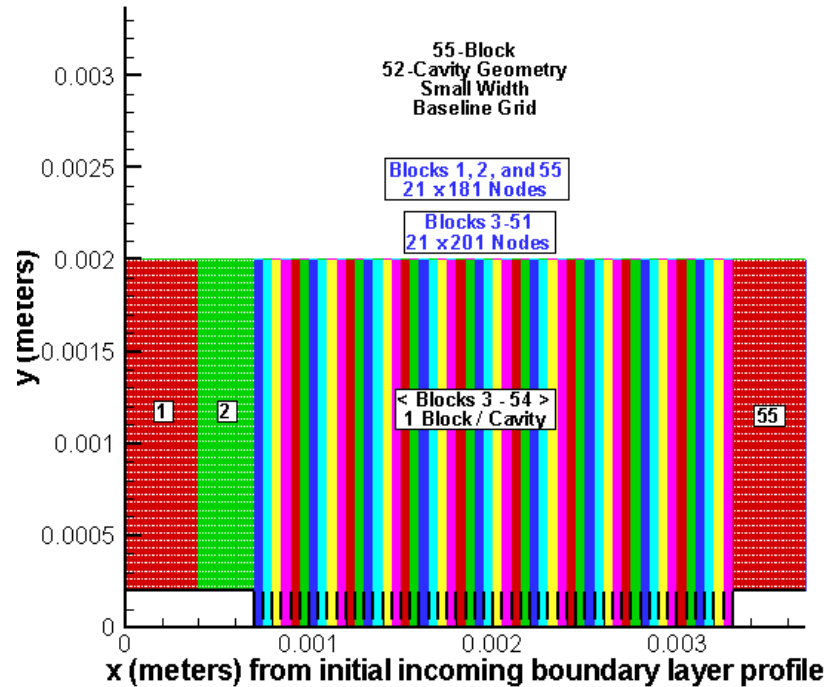
Figure 2.5. Multi-Block Layout for 52-Cavity Geometry

Boundary conditions for the example test case are presented in Figure 2.6. These input boundary conditions are common for all cases in this study. The left face of Block 1 is the INFLOW face. It includes four inflow "sub-faces" corresponding to the four output profile files generated by the upstream flat plat geometry. Recall that the blocks were stacked in the y-direction, thus the input face of the downstream test geometry required four inflow sub-faces to make up the total inflow. The top of all blocks is set as FAR-FIELD. The right face of Block 55 is designated as the OUTFLOW, here taken as extrapolation. The bottom of each block is set as ADB-WALL (adiabatic wall).
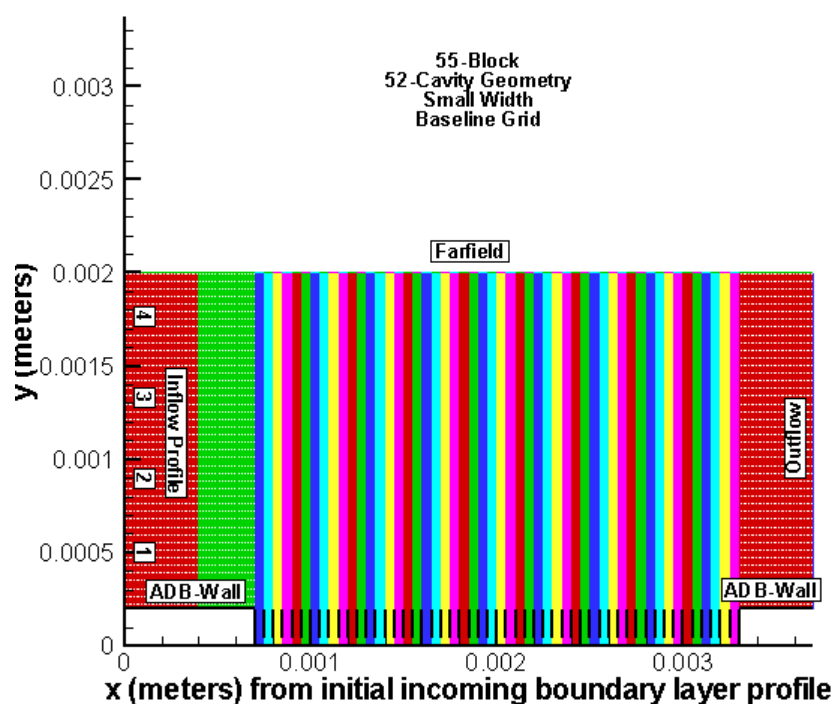
Figure 2.6. Boundary Conditions for the Micro-Cavity Test Geometry

The cavity walls are a very critical part of the geometry setup for each test case. Cavity walls are classified as either "perforated" or "unperforated" in each test case. Designation of perforated walls signifies that h > 0, while the designation of unperforated walls indicates that h = 0. Figure 2.7 and Figure 2.8 depict enlarged views of the cavity region to more adequately show the differences between the perforated and unperforated cavity walls. The walls themselves are treated as adiabatic walls and have zero thickness. For perforated walls, the adiabatic wall condition is only set for the nodes that constitute the wall itself. The region of the perforation has no boundary condition, corresponding only to a cut condition between two adjacent block faces.
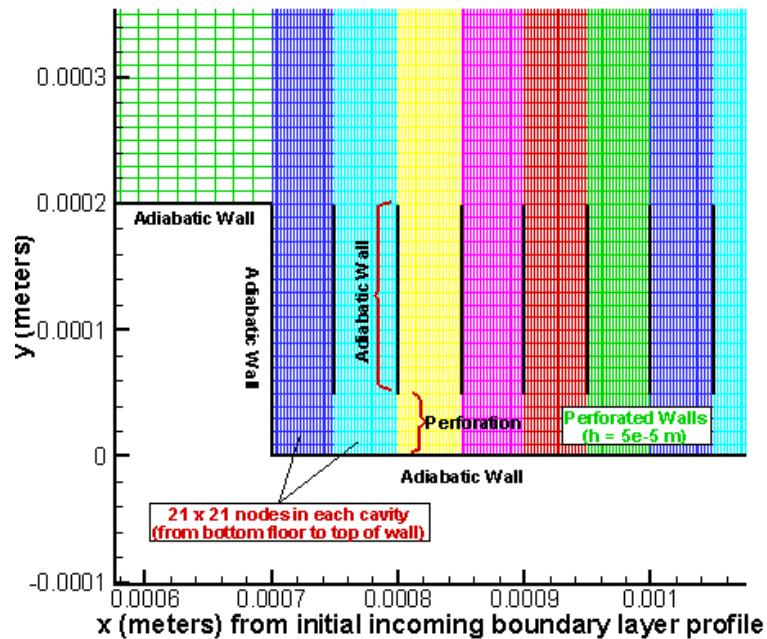
Figure 2.7. Detailed View of Perforated Cavity Wall
Geometry and Boundary Conditions
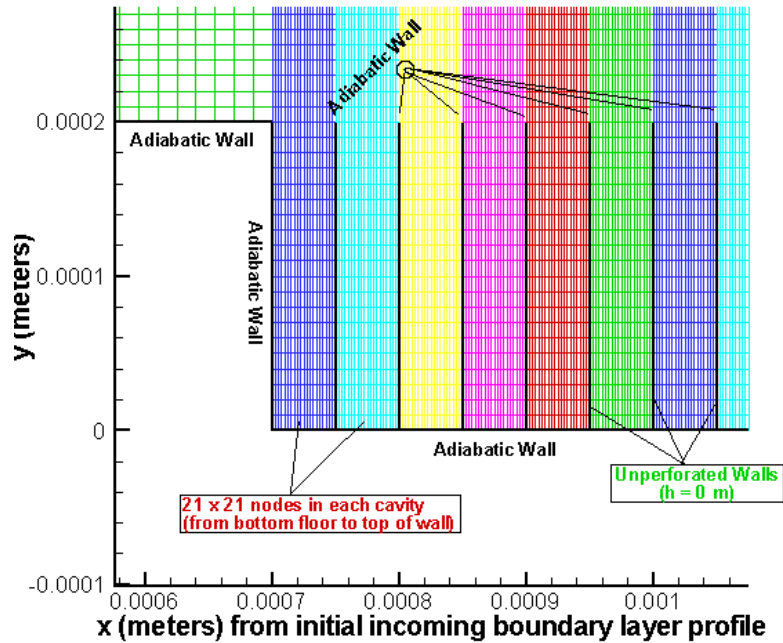
Figure 2.8. Detailed View of Unperforated Cavity Wall
Geometry and Boundary Conditions

2.4. GRID AND MESH SIZING

Three main grid densities were used for analyzing the micro-cavity domains: coarse, baseline, and fine. The coarse and fine grids will be discussed further as part of the mesh sequencing discussion in Section 6. The following discussion focuses on the baseline grid and provides representative numbers. In terms of the overall solution strategy using the baseline grid, Blocks 1, 2, and N+3 consist of 21 (horizontal, or x-direction) nodes by 181 (vertical, or y-direction) nodes. Each of the blocks in the cavity region (3 through N) consists of 21 x 201 nodes. Focusing on the embedded cavities themselves, the baseline grid contains 21 x 21 nodes in each cavity. For the small width cavity cases (described previously), these nodes are spaced evenly 2.5 x 10^{-6} m in the x-

direction and 1 x 10^{-5} m in the y-direction, such that the aspect ratio is 4. Table 2.3 summarizes the grid sizing and mesh for this study (for small width cavity cases). As noted previously, medium width cavity cases correspond to cavities scaled up 250% in size (2.5X) (both horizontally and vertically). Note, however, that the vertical height of the outer (boundary layer) flow above the embedded cavity flows remains the same between 'small width' cavities and 'medium width' cavity cases.

Table 2.3. Summary of Grid Sizes and Mesh for Micro-Cavity
Test Cases/Small Width Cavity Cases

Grid Type	Nodes in Blocks 1, 2, N + 3	Nodes in Blocks 3 to N	Nodes in Cavities	Node Spacing in X-Direction	Node Spacing in Y-Direction
Coarse	11 x 91	11 x 101	11 x 11	5.0 x 10^{-6} m	2 x 10^{-5} m
Baseline	21 x 181	21 x 201	21 x 21	2.5 x 10^{-6} m	1 x 10^{-5} m
Fine	41 x 361	41 x 401	41 x 41	1.25 x 10^{-6} m	5 x 10^{-6} m

3. 52-CAVITY REGION SMALL WIDTH BASELINE GRID RESULTS

The first case study is conducted using a 52-cavity length region with small width cavities analyzed using the baseline 21 x 21 (per cavity) node grid. This set of test cases uses a fixed inflow plane which is the exit profile from an upstream marching simulation of a boundary layer with a free-stream Mach number equal to 2.0; this plane is located ten centimeters downstream of the leading edge of the plate (profile US1 as described in Section 2). The length of the cavity region is 0.26 cm (or 2.6% of the upstream flat plate length from the leading edge). Cavity height, H, for this case using small width cavities is 0.0002, corresponding 13.65% of the thickness of the incoming boundary layer (H/δ = 0.13652). A visualization of the flow over the driven micro-cavity region is provided in Figure 3.1 in terms of Mach number contours. As displayed in this figure, but true for all steady (drag converged) cases examined, there is very little impact on the vertical distribution of velocity and Mach number through the boundary layer over the length of the overall cavity region. In this section, three cases are analyzed for the 52-cavity small width region case study: gated, unperforated, and ungated. It should be noted that all drag results presented in this work are given in units of Newtons, although, due to the two-dimensional modeling of the flow, are implicitly Newtons per meter width.
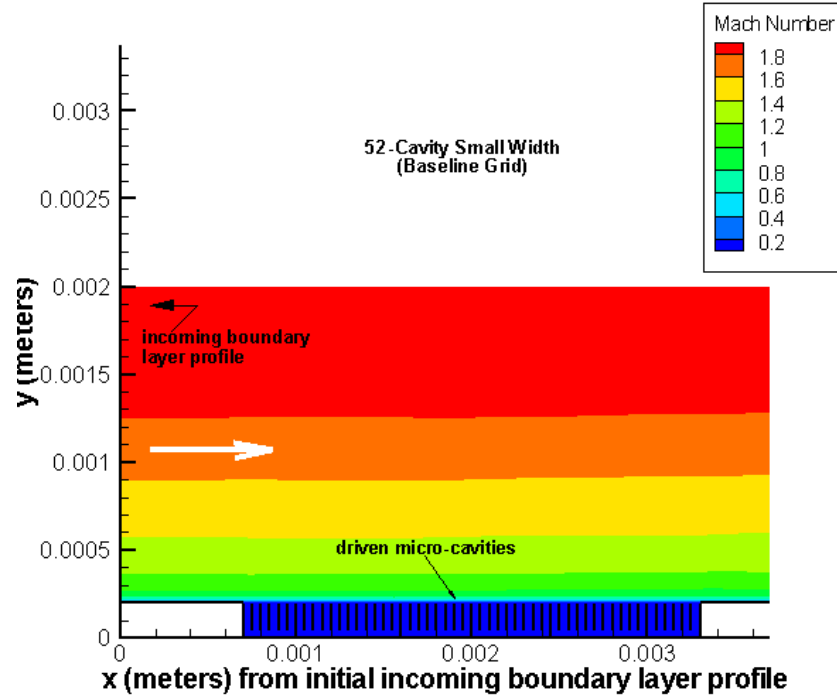
Figure 3.1. Mach Number Contours from VULCAN with Incoming Flow Over
the 52-Cavity Small Width Region

3.1. GATED CAVITY REGION

The first case in this study uses the 52-cavity small width cavity region with two

gates located at the 17th and 34th wall locations (x = 0.0016 m and x = 0.00245 m). As

discussed previously, these gates are adiabatic walls that extend to the bottom floor of the

cavity region (h = 0) while all of the rest of the cavity walls are perforated at the bottom

with (h = 6 x 10^{-5} m). The simulation began with a non-time accurate scheme with a

Courant-Friedrichs-Lewy number (CFL) beginning at 0.1, increasing to 0.5 after 10,000

cycles, and finally ramping up to 1.0 after 20,000 cycles. The solution exhibits a steady

convergence to a drag value of 2.224 N after approximately 100,000 cycles. The time

history of the drag force is shown below in Figure 3.2.
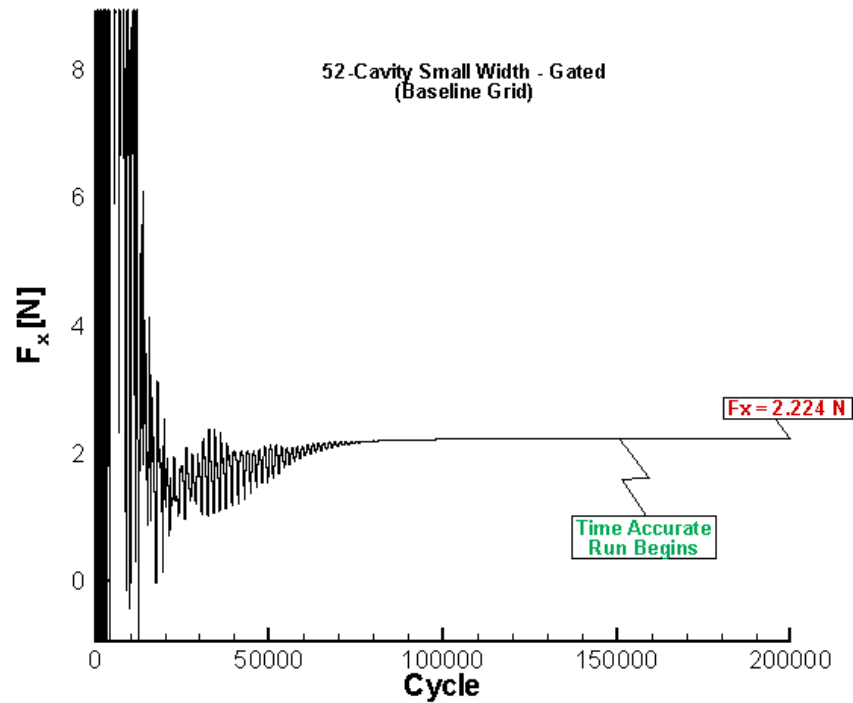
Figure 3.2. Drag Time History Plot for the Gated 52-Cavity
Small Width Mach 2 Test Case

A time-accurate solution was then run using a distributed approximating function
(DAF) with a time step of 2 nanoseconds (2.0×10^{-8} s) with 20 sub-iterations between
each step. This time-accurate simulation was started utilizing the non-time accurate
simulation at 151,000 cycles as the initial condition. As indicated in Figure 3.2, no
discernible change in the net drag value occurs when switching to the time-accurate case.
For the 52-cavity (small width cavities) region using the baseline grid, time-accurate vs.
local time stepping has no bearing on the resulting drag, i.e., once the solution converges,
drag remains constant despite changing the time scheme. This, in fact, was found to be
true for all 'steady' cases examined in the present investigation.

The CFD generated pressure contours in the region with cavities are presented in Figure 3.3. It can be seen that the strongest effects of the cavity region on the pressure field occur at the end of the cavity region where the flow must 'reestablish' on the trailing flat plate. However, there is little change in pressure overall. (Note the small levels of pressure change within the contours).
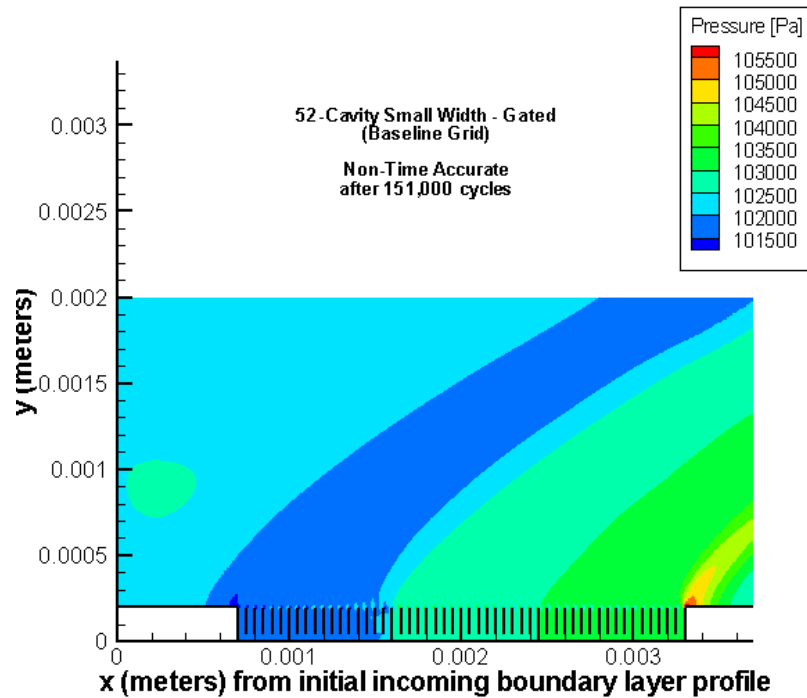
Figure 3.3. Pressure Contours for the Gated 52-Cavity
Small Width Mach 2 Test Case

The pressure field produced by the simulation, although characterized by very small changes in general, is sub-divided into four regions, for purposes of discussion. First, a pressure drop occurs at the beginning of the cavity region where the leading flat

plate section ends and the embedded cavity region begins; the flow expands slightly due to the presence of the cavities. The contours indicate that the pressure then increases slightly at both locations of the (two) gates, and reaches a local maximum at the downstream upper corner of the micro-cavity region, where the flow re-establishes back onto the downstream flat plate section.

A jet of reversed flow is established through the perforations in the cavity walls, and contributes a negative contribution to drag force (i.e., effectively a positive contribution to thrust due to the negative skin friction on the bottom wall of the cavities, associated with the jet). This jet is the result of the combined separation zones created by the flow vortices present between the cavity walls and the interaction between cavities allowed by the perforations at the bottom of vertical cavity walls. As shown in Figure 3.4, the magnitude of the reversed flow velocity is between 5 and 10 m/s, or about 1.5% of the free-stream velocity. Also shown in this figure are streamline traces, in order to visualize the patterns of recirculation within the cavity region(s).
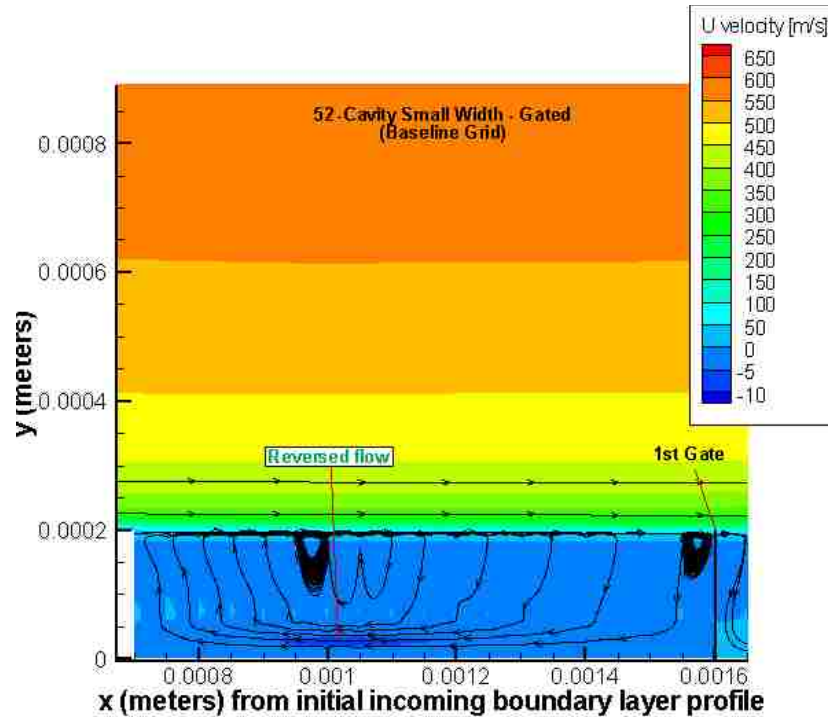
Figure 3.4. U-Velocity Contours and Flow Streamtraces for the Gated 52-Cavity Region from the Start of the Cavity Region to the First Gate

While reversed flow exists in the region between the start of the cavity region and the first gate, the flow in the region bounded between the first and second gate is not reversed. As shown in Figure 3.5, the cavities located in that region (between the two gates) actually have positive u-velocity contours and the stream line traces show flow movement mainly in the positive x-direction. Downstream of the second gate, the flow in the embedded cavities becomes reversed once again. The presence of the gates appears to break the flow up into regions of reversal and non-reversal within the overall micro-cavity region, at least for this test case.
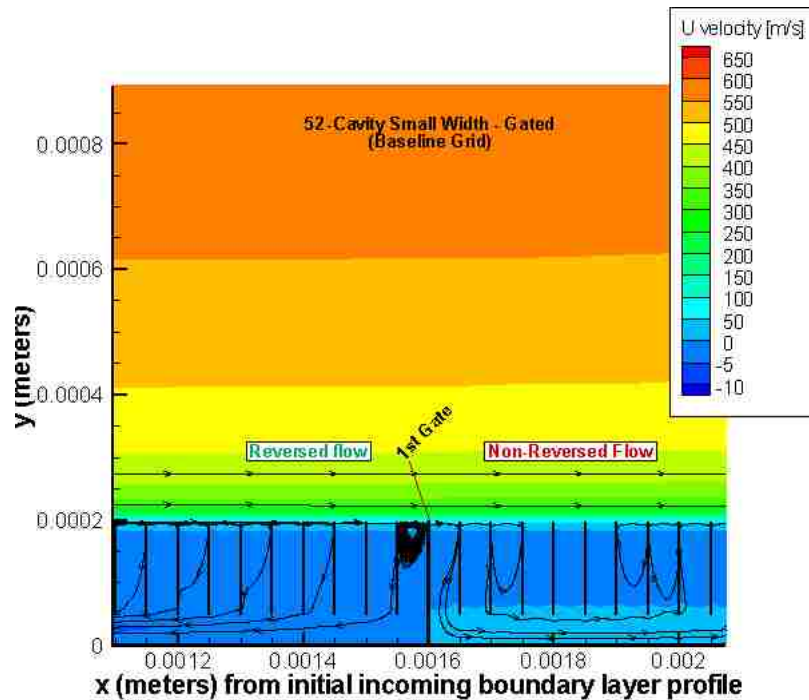
Figure 3.5. U-velocity Contours and Flow Streamtraces Indicate Both Reversed and Non-Reversed Flow Near the First Gate

Fluid flowing in the negative x-direction across portions of the overall micro-cavity region can, in fact, make the overall skin friction drag contribution 'negative' within that region. However, due to the extremely small velocities within the cavity (whether positive or negative), skin friction is essentially considered here to be zero within all cavity regions for all cases tested. This is particularly true when the magnitude of skin friction drag within the overall cavity region is compared to a reference flat plate drag and/or to pressure drag associated with vertical cavity walls.

Pressure acting on the vertical cavity walls generates a pressure drag component that is completely in the positive x-direction. Figure 3.6 shows the detailed spatially distributed (x-direction) separate contributions of both cumulative pressure and shear forces in the x direction that occur on all solid walls, for this gated 52-cavity small width

case. Note that this figure presents cumulative pressure drag as a continuous line with x distance, although there are pressure contributions to overall drag only at discrete (vertical) cavity walls; the line shown simply connects these discrete points. A sample of the post processing code used to generate Figure 3.6 is provided in Appendix B.

Figure 3.6. Breakdown of the Contributions of Skin Friction and Pressure Forces to Total Drag Over the Entire 52-Cavity Small Width Mach 2 Test Case

Pressure drag does not increase on the leading and trailing flat plates surrounding the micro-cavity region, as expected, since pressure acts only in the y-direction for a flat plate at zero angle of attack. The pressure drag drops initially at the beginning of the cavity region due to the negative pressure force on the initial (upstream) surface of the

first cavity. It then essentially increases linearly with x across the cavity region, indicating that pressure is slightly higher on the upstream side of each vertical wall than on the downstream side of each wall, with regularity to this trend with axial distance. Further investigation demonstrates that the pressure imbalance, and hence the linearly increasing pressure drag contribution as shown in Figure 3.6, is almost entirely associated with the top part of each vertical cavity wall. This phenomenon was discussed as more or less inevitable, in the introduction section of this work. The rate of increase in pressure drag for the case here is 576.7 N/m from the beginning to the end of the micro-cavity region. Presence of the two gates (vertical walls with no perforations) is evident and expected from the two spikes in the total pressure drag, but these gates have no net effect on the overall nearly linear trend of pressure drag increase across the micro-cavity region. Total cumulative drag due to pressure is generally negative (meaning a net contribution to thrust instead of drag) until the end of the cavity region is reached and the flow reestablishes upon the aft flat plate region. Upon reaching the end of the overall cavity region, the pressure significantly increases its contribution to drag due to the positive axial pressure contribution on the vertical wall associated with the aft plate region, before leveling over the downstream flat plate. Skin friction drag increases on the forward and rear flat plates, but decreases very slightly throughout the cavity region itself. This shows that there is virtually no shear occurring in the cavity region itself as discussed earlier, and that total drag within the overall cavity region is almost entirely driven by the pressure drag acting in the x-direction, associated with the vertical walls of the cavities. Considering only the cavity region itself (x = 0.0007 m to x = 0.0033 m, i.e., removing the leading and trailing flat plates), the skin-friction drag was found to be -0.009910 N.

This corresponds to a very slight positive contribution to thrust. The pressure drag was found to be 1.5700 N, making the total drag over the micro-cavity region 1.5601 N.

3.2. UNGATED CAVITY REGION

The 'ungated' cavity region simulation uses the same geometry as the case discussed in Section 3.1, except that there are no gates, i.e. all cavity walls are perforated. For this case, a non-time accurate solution was used with CFL of 1.0. The drag force history is presented in Figure 3.7. The solution exhibits a solid convergence to a fixed total drag value of 2.2212 N. This value is within 0.1% of the converged drag value found in the gated simulation.
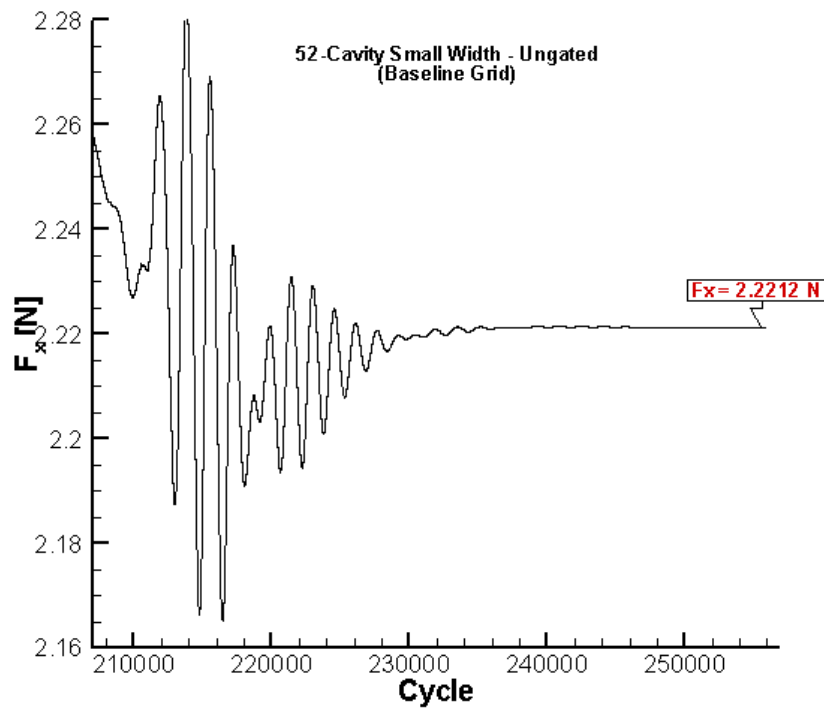
Figure 3.7. Drag Time History Plot for the Ungated 52-Cavity
Small Width Mach 2 Test Case

In the interest of reducing computational time, the initial run of the ungated simulation took the flow-field of the converged gated case (previously described) as its initial condition. The large oscillations in the drag force at the beginning of the ungated solution are therefore due to the simulation coping with the cut condition change removing the two gates. In order to ensure the validity of this technique (i.e., using the previous gated case flow-field as the initial condition for a different (ungated) configuration), a separate simulation for the ungated case beginning from free-stream initialized everywhere was done. This simulation resulted in the same final converged drag value.

Pressure contours in Figure 3.8 show that the flow-field is similar to the previous gated case in that there remain several weak but distinct pressure zones spanning the region, as previously described. The highest pressure concentration still occurs at the end of the cavity region, on the top right wall of the last cavity (where the flow reestablishes on the downstream flat plate section). Despite slight differences in the pressures upstream of the end of the cavity region when compared to the gated case, the peak pressure remains the same in both cases, reaching ~105500 Pa which is only 3% greater than the inflow (free-stream) pressure value.
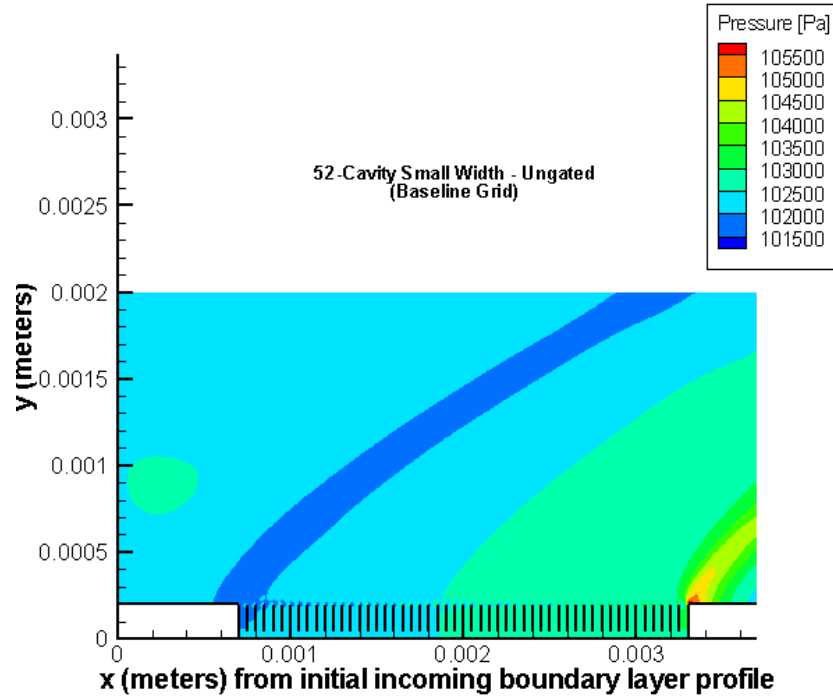
Figure 3.8. Pressure Contours for the Ungated 52-Cavity
Small Width Mach 2 Test Case

As with the gated case, the ungated results show a jet of reversed flow passing through the perforations, as depicted in Figure 3.9. The absence of gates allows the reversed flow to propagate throughout the entire cavity region, rather than being sub-divided into separate regions. However, the maximum magnitude of the u-velocity of the reversed flow remains around 10 m/s, as with the gated case, i.e. is very small.
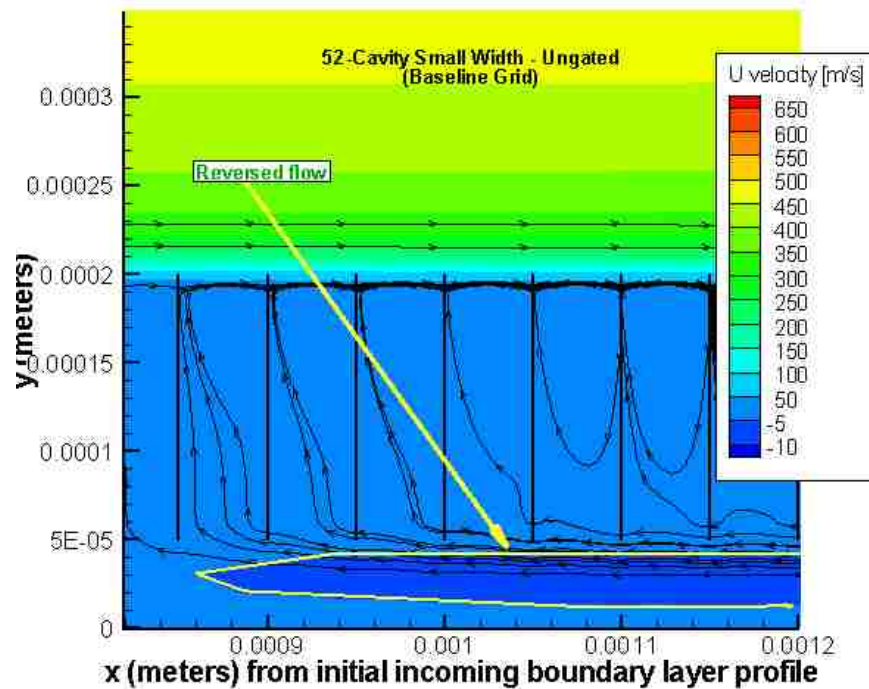
Figure 3.9. U-Velocity Contours and Flow Streamtraces for the Ungated 52-Cavity Small Width Mach 2 Test Case

Figure 3.10 shows the separate axial distribution of cumulative pressure and shear forces acting on the solid surfaces for this configuration. The skin friction drag exhibits the same behavior for the ungated case as that of the gated case previously discussed; linear increases on the leading and trailing edge, and a very slight decrease across the cavity region. Pressure drag retains roughly the same linear relationship with x as noted in the gated case, increasing at a rate of 588.427 N/m. The absence of the two gates is clearly shown (note that the two spikes at gate locations shown in the gated case disappear), but the cumulative value of pressure drag and its overall trend do not differ significantly between the two cases.

Figure 3.10. Breakdown of the Contributions of Skin Friction and Pressure
Forces to Total Drag Over the Ungated 52-Cavity Small Width Mach 2 Test Case

Skin friction and pressure across the cavity region for the ungated case were found to be -0.026841 N and 1.5822 N, respectively. Skin friction drag decreased (contributed greater thrust) very slightly compared to the gated case, while the pressure drag increased very slightly. The total drag over the region is 1.5553 N, thus exhibiting less than one-tenth of a percent change from the gated test case. These results show that the lack of gates does contribute to a decreased skin friction drag; however the increase in pressure drag cancels out that effect, resulting in a nearly identical final total drag value between the two cases.

3.3. UNPERFORATED CAVITY REGION

The unperforated simulation extended all vertical cavity walls to the 'floor' of the cavity region (h=0 for all walls), making all walls essentially "gated". The same non-time accurate scheme with a CFL of 1.0 was used in this case. As was done with the ungated solution, the final converged flow-field from the gated test case was used as the initial flow-field (initial condition) for the unperforated simulation. The resulting drag history is given in Figure 3.11. Total drag converges to 2.2249 N after approximately 60,000 iterations. This drag value is within 0.04% of the drag for the gated case and within 0.2% for the ungated case. A time accurate scheme was used after convergence with local time stepping was reached; there was no change in the final drag result.
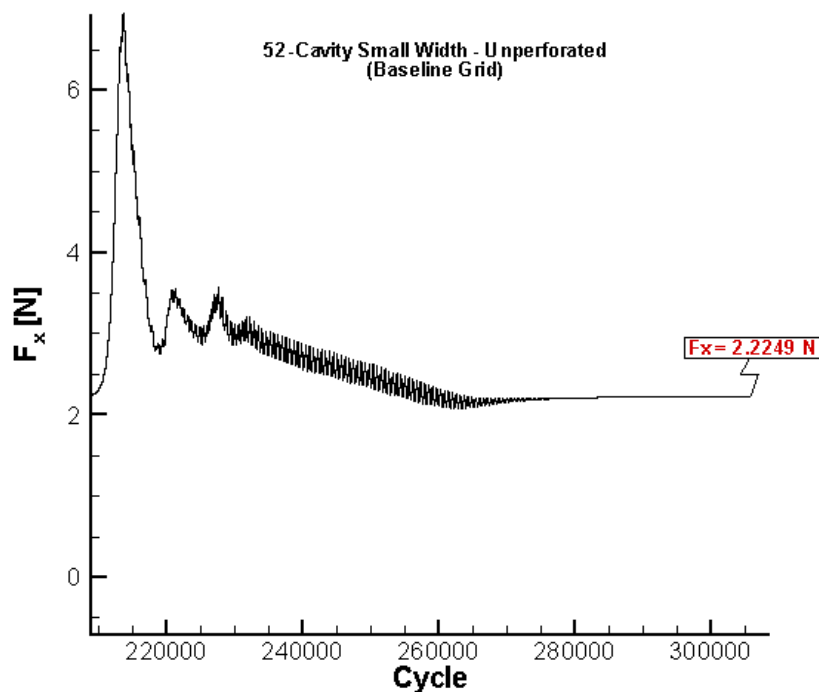
Figure 3.11. Drag Time History Plot for the Unperforated 52-Cavity
Small Width Mach 2 Test Case

The pressure contours for the unperforated case presented in Figure 3.12 exhibit nearly the same characteristics as noted and discussed in the ungated case. There is a similar pattern of weak pressure increases, with the main difference being that the pressure increase seems to initiate (or migrate) further upstream for the unperforated case. Again, the local region of the highest pressure occurs in the final cavity on the right upper wall, but the pressure there is still is only 3% greater than the free-stream pressure. The overall increase in pressure across the cavity region is virtually the same for the three cases presented: gated, ungated, and unperforated.
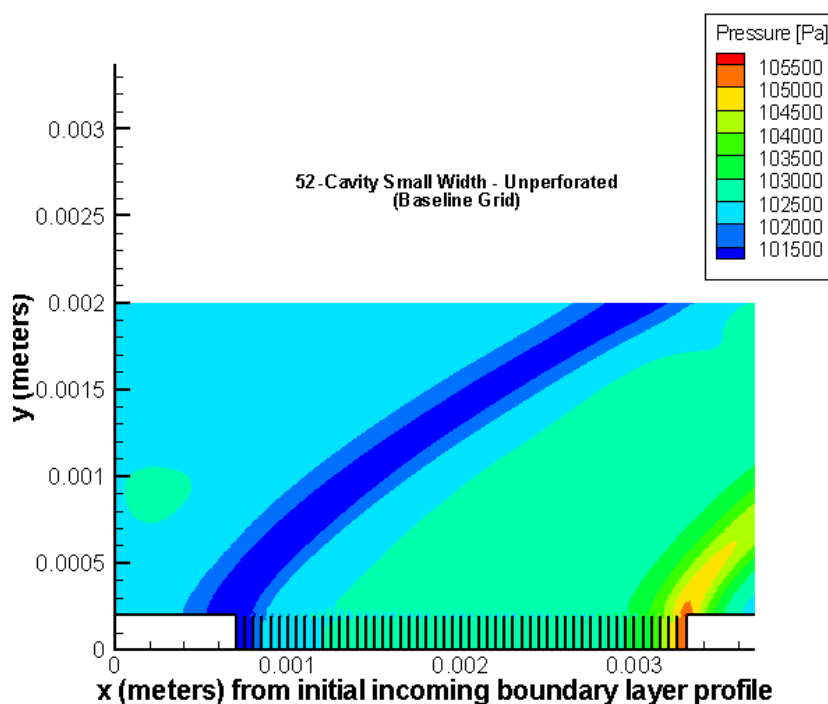
Figure 3.12. Pressure Contours for the Unperforated 52-Cavity
Small Width Mach 2 Test Case

The most significant difference shown visually between the unperforated case and the gated/ungated case is expected; the lack of the reversed flow jet. Without perforations in the cavity walls, cavity flows are isolated from one another and distinct clock-wise flow vortices establish within each cavity region. Figure 3.13 shows streamtraces of the flow in the cavity regions. The well-defined and repeating vortices rotate in the clockwise direction inside each of the cavities, meaning that there is a certain amount of flow reversal present. However, there is no significant region of negative u-velocity developing due to the inhibiting effect of the cavity walls. It is further shown in Figure 3.12 that the vortices in the individual cavities are strongest near the top of the cavities, where the greatest shear from the outer flow is present.
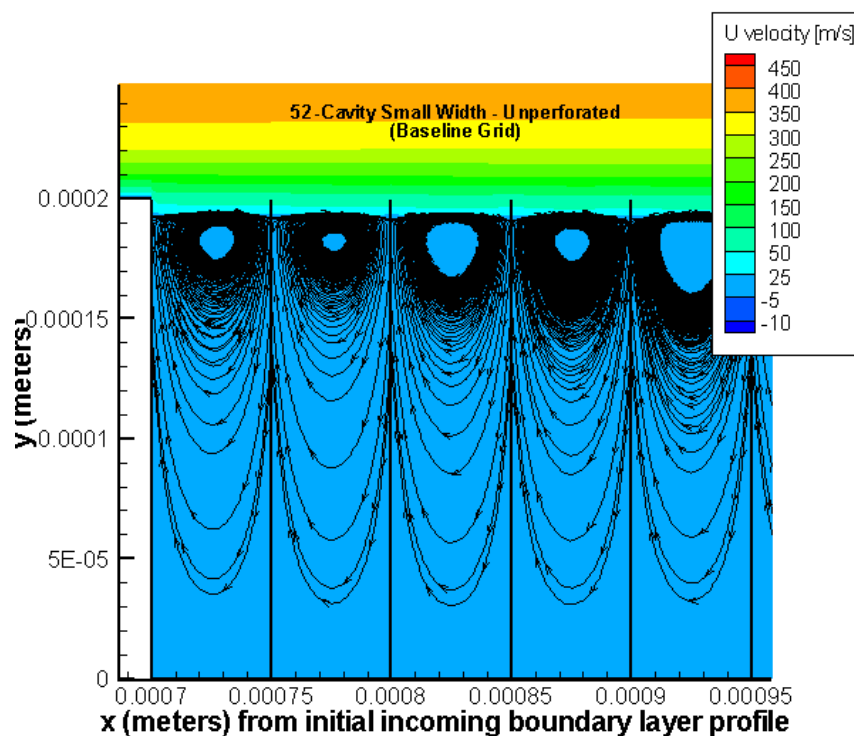
Figure 3.13. U-Velocity Contours and Flow Streamtraces for the Unperforated 52-Cavity Small Width Mach 2 Test Case

The cumulative distributions of pressure and skin friction drag forces on walls of the unperforated configuration is separately plotted in Figure 3.14. Note that the large drop in pressure drag seen at the beginning of the overall micro-cavity region for cases with perforated vertical walls does not appear, since the right vertical wall of the first cavity for the unperforated case extends to the floor of the micro-cavity region. Similarly, the large increase in pressure drag seen at the end of the overall micro-cavity region for perforated cases also disappears. However, the overall linearly increasing pressure trend remains the same from beginning to end of the micro-cavity region, as does the skin friction drag decrease across the overall cavity region (although it exhibits only a very slight decrease).
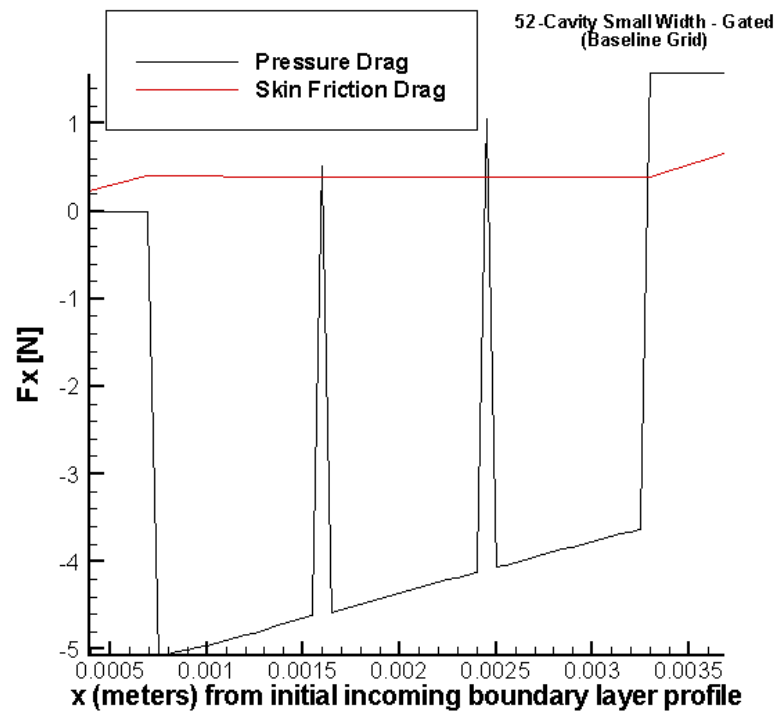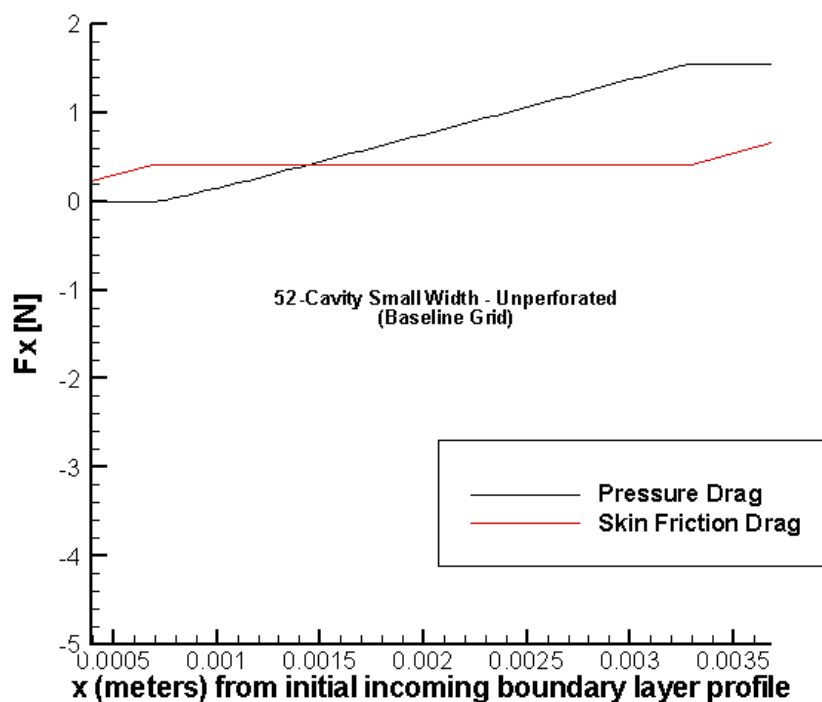
Figure 3.14. Breakdown of the Contributions of Skin Friction and Pressure Forces to Total Drag Over the Unperforated 52-Cavity Small Width Test Case

Skin-friction drag across the overall cavity region itself was found to be 0.000032 N (i.e. effectively zero). Pressure drag was 1.5556 N. This skin friction value, although very small, is the highest of the three cases examined in this section, due to the inability of the reversed flow jet to form when vertical walls separating cavities are not perforated. The pressure drag for the unperforated case is the lowest of the three cases, but has the similar linear relationship as the gated and ungated cases, increasing at a rate of 596.6 N/m across the overall cavity region. Note that this rate is greater than seen in the gated and ungated cases, yet pressure drag is lowest of the three for this case. This suggests that the downstream pressure spike at the end of the cavity region in cases with perforated cavities causes an increased jump in pressure drag. The minor changes in the skin friction and pressure drag cancel out however, as the end resultant total drag force for the unperforated case remains within 0.1% of both previous (perforated) cases.

3.4. COMPARISON TO FLAT PLATE RESULTS

The primary focus of this study is to determine whether the driven micro-cavity region can perform better in terms of experiencing less overall drag than an unmodified (no embedded micro-cavities) flat plate. In order to generate the skin friction drag associated with a reference (unmodified) flat plate boundary layer over the same length as the micro-cavity regions studied, an additional flat plate marching simulation was performed (see Section 2 of this thesis) using the increased length (from leading edge of the flat plate, but including the length of the domain for the elliptic simulations with the micro-cavities). The reference flat plate skin friction drag for the section of domain length as modeled in simulations of the embedded micro-cavity concept could then be

readily computed. Here, for the purpose of direct comparison with drag only within the overall micro-cavity region itself, the skin friction drag over the leading and trailing flat plate regions of the micro-cavity region were then subtracted as well, i.e., only reference skin friction drag over the length of the micro-cavity region itself (0.0026 m) was used for comparisons to micro-cavity drag results. Results for each of the three previous cases versus reference flat plate section drag values are tabulated in Table 3.1.

Table 3.1. 52-Cavity Small Width Region Drag Comparison of Baseline Grid Cases

Case	Viscous Drag [N]	Pressure Drag [N]	Total Drag [N]	Total Drag (Flat Plate) [N]	Drag Reduction [%]
Gated	-0.009910	1.5700	1.5601	1.906	18.1503
Ungated	-0.026841	1.5822	1.5553	1.906	18.3984
Unperforated	-0.000032	1.5556	1.5556	1.906	18.3841

Total skin friction drag on the reference flat plate section of length equal to the region with micro-cavities is 1.906 N. In each of the three cases considered with micro-cavities, the skin friction drag contributed a very small negative component to the overall drag (a net gain in thrust). All effective drag in the gated, ungated, and unperforated cases is therefore attributed to pressure forces acting on the vertical cavity walls. Total drag over the driven micro-cavity region is ~1.56 N. All test cases with cavities therefore had significant drag reductions as measured from a reference flat plate boundary layer; these drag reductions were approximately 18%.

3.5. REDUCED MACH NUMBER RESULTS

In order to study the effect of Mach number on drag reduction results, the same three test cases (gated, ungated, perforated) were conducted using a reduced free-stream Mach number of 1.2. All other input parameters including a 10 cm upstream flat plate, the configuration geometry itself and grid resolution remain unchanged (i.e. 'small width' cavities were used with the 'baseline' grid resolution). Additionally, the same computational methodology was used. For all three test cases with micro-cavities previously considered at a free-stream Mach of 2.0, the time history of the overall drag demonstrated definite convergence to a converged single drag value. This remains true only for the unperforated case using the fine grid when the free-stream Mach is equal to 1.2. For that case the total drag is 1.0209 N. Figure 3.15 and Figure 3.16 show the gated and ungated drag versus iteration plots, for free-stream Mach of 1.2, respectively.
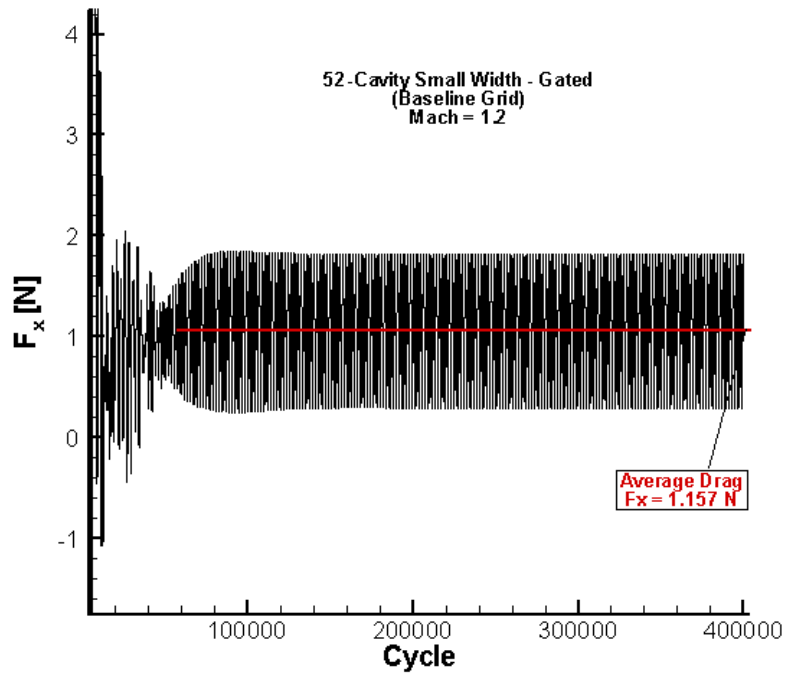
Figure 3.15. Drag Time History Plot for the Gated 52-Cavity
Small Width Mach 1.2 Test Case
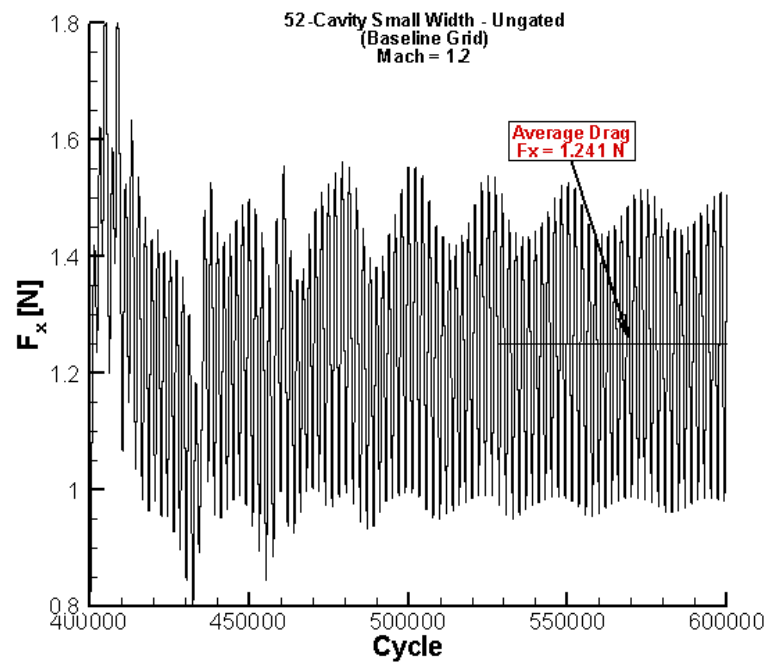
Figure 3.16. Drag Time History Plot for the Ungated 52-Cavity
Small Width Mach 1.2 Test Case

Significant oscillations are present in the drag result for the gated and ungated cases. The average drag value, however, seemingly remains constant as the oscillations become regular. This shows that the flow is exhibiting 'quasi-steady' characteristics. Average drag value for the gated simulation is 1.157 N (13% higher than the unperforated case). Average drag for the ungated simulation is 1.241 N (22% higher than the unperforated).

The trends observed previously for the Mach 2.0 case generally hold for the Mach 1.2 case in terms of decreased skin friction drag inside the micro-cavity region itself (essentially zero), and pressure drag component increasing linearly with x across the region with micro-cavities. Since only a 'quasi-steady' (oscillatory about a fixed value) result exists for drag for the gated and unperforated cases, chatter exists in the resulting cumulative drag forces axial distribution plots shown in Figure 3.17 and Figure 3.18.
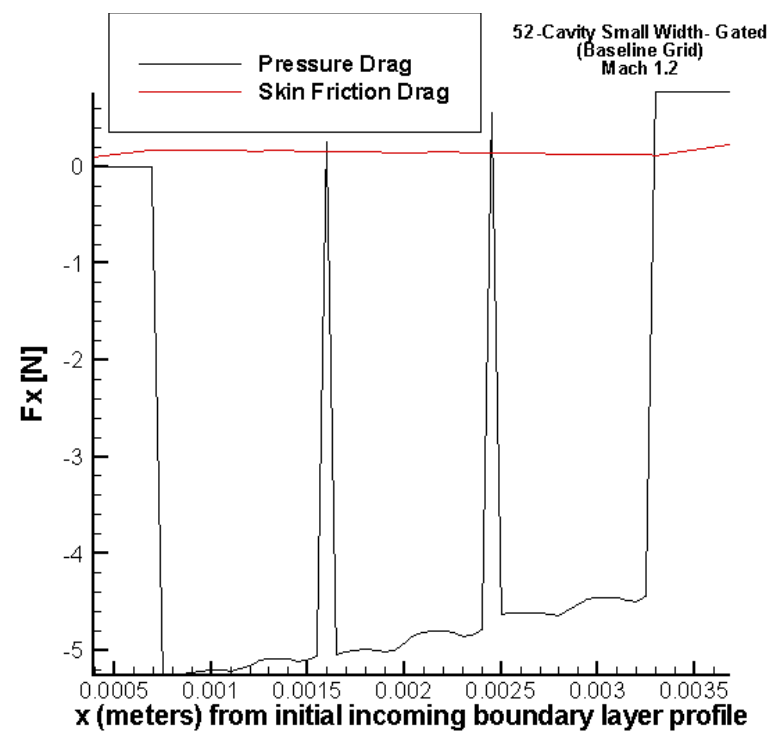
Figure 3.17. Breakdown of the Contributions of Skin Friction and Pressure Forces to Total Drag Over the Gated 52-Cavity Small Width Mach 1.2 Test Case
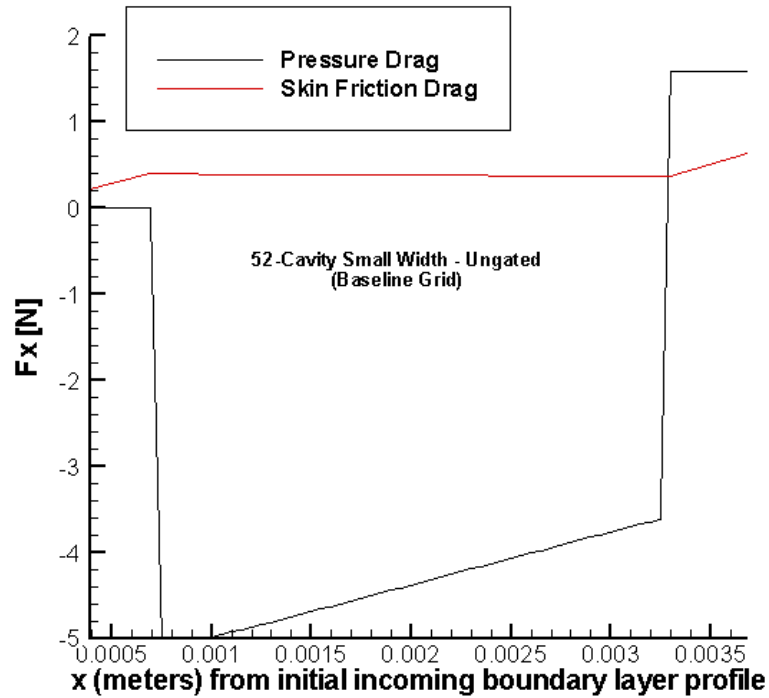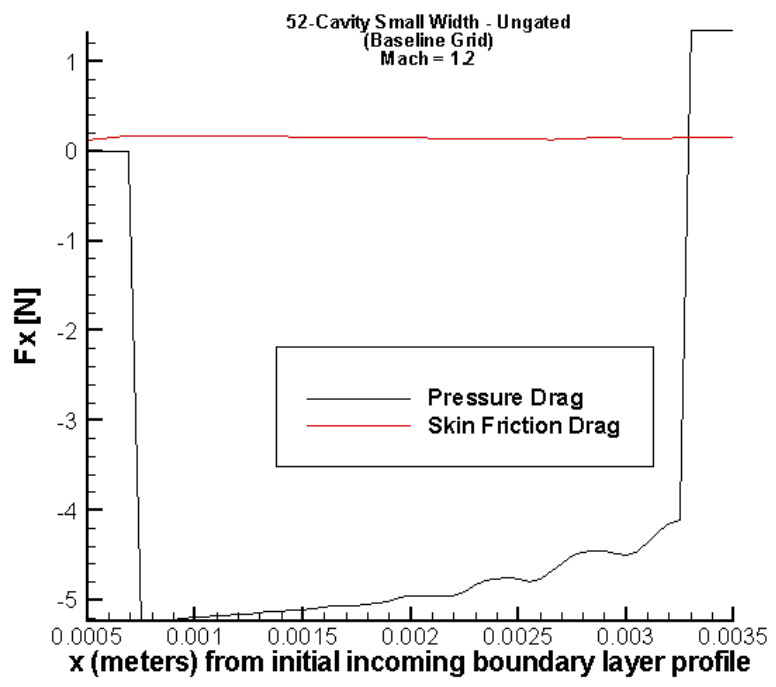

Figure 3.18. Breakdown of the Contributions of Skin Friction and Pressure Forces to Total Drag Over the Ungated 52-Cavity Small Width Mach 1.2 Test Case

The chatter is most evident in the pressure drag in the cavity. These figures serve only to show qualitatively the decomposition of drag forces. The results displayed are only a snapshot in time of the oscillatory drag value and do not represent a time-averaged drag result. However, Figure 3.17 and 3.18 demonstrate that the cumulative pressure and shear distributions behave in a generally similar manner as seen in the Mach 2.0 cases.

The total time-averaged drag values for each of the three Mach 1.2 cases as well as a reference total drag for a flat plate section over the same length are tabulated in Table 3.2. The drag associated with the leading and trailing edge sections of the elliptic domain length has been subtracted from the results for cases with micro-cavities and for the reference flat plate section drag values,, i.e. only drag values acting over the micro-cavities, or the reference length of the micro-cavity region, is considered and compared in this table.

Table 3.2. Drag Comparison of Baseline Grid Cases for Mach 1.2 Flow

Case	Total Drag [N]	Total Drag (Flat Plate) [N]	Drag Reduction [%]
Gated	0.8539	0.878	2.745
Ungated	0.9372	0.878	(6.742)
Unperforated	0.717058	0.878	18.3305

The unperforated case, the only Mach 1.2 case in the present section that converged to a single fixed value of drag (no oscillatory behavior), outperforms the reference flat plate in terms of achieving a reduction in drag of 18.3305%, which is nearly the exact same result as obtained for Mach 2.0 free-stream flow. The gated case exhibits a 2.745% reduction in total drag from a reference flat plate length for this Mach

1.2 flow. Finally, the ungated case has 6.742% greater drag than the reference flat plate section. The reduced Mach number seems to have an adverse effect on the convergence, or transitory behavior, of the gated and ungated cases, and skews the total overall drag results upward. The fully converged unperforated case performs the same for the two free-stream Mach numbers.

4. 208-CAVITY SMALL WIDTH BASELINE GRID RESULTS

This section provides results from a case study that utilized an overall cavity region four times the length of that used in the test cases presented in Section 3 (i.e. increased the number of cavities, and hence the length of the cavity region, by a factor of four). This was done to study the relationship between overall cavity region lengths and drag reduction potential. The 208-cavity (small cavity width) geometry is analyzed using the 211-block 21 x 21 (in cavity) node baseline grid. This case uses the same free-stream conditions ($M_\infty = 2.0$, $T_\infty = 288$ K, $P_\infty = 101325$ N/m^2) and the same boundary layer profile (as generated by a marching simulation to a location 10 cm from the leading edge of a flat plate) as the 52-cavity (small width) cases presented in the previous section. The length of the cavity region is 0.0104 m (1.04 cm). Only one test case, the gated configuration, was analyzed using the 211 block 208-cavity geometry due to computational resources required. A total of 11 gates are used in this case, with gates evenly spaced at the 17th, 34th, etc. walls (i.e., at x = 0.0016 m, 0.00245 m, 0.0033 m, 0.00415 m, 0.005 m, 0.00585 m, 0.0067 m, 0.00755 m, 0.0084 m, 0.00925 m, and 0.0101 m). All other vertical cavity walls were perforated. Flow Mach contours are presented for this converged case in Figure 4.1.
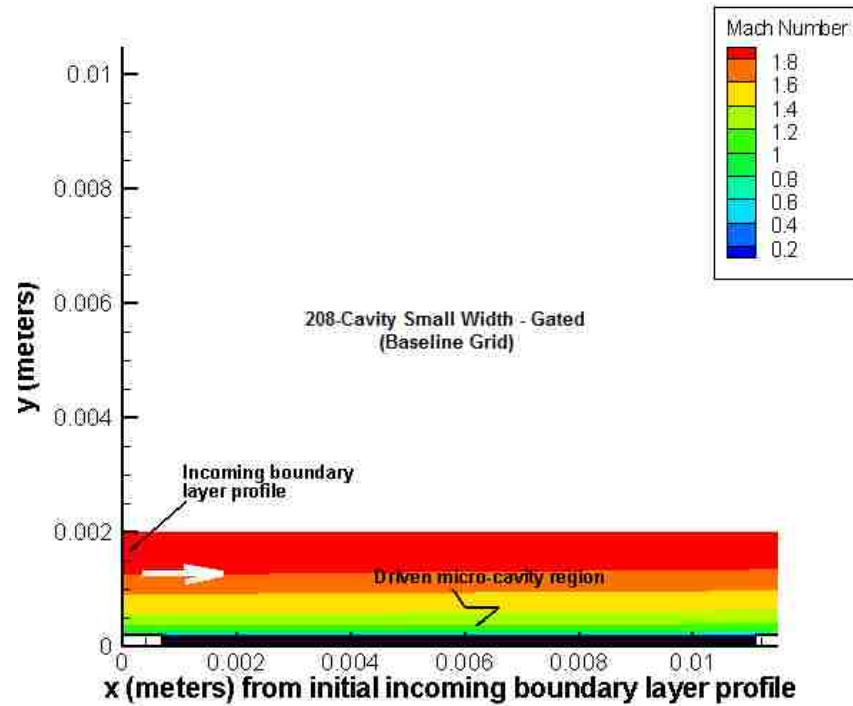
Figure 4.1. Mach Number Contours from VULCAN Showing the Incoming Flow Over the 208-Cavity Small Width Mach 2 Test Case

The simulation for the 208-cavity (small width) region begin with a non-time accurate solution with a CFL beginning at 0.1, stepping up to 0.5 after 10,000 iterations, and then ramping to 1.0 until 20,000 iterations were reached. This is the same CFL scheme used in the 52-cavity cases. After approximately 400,000 iterations, the solution converged with a fixed drag value of 7.0451 N. The complete time history for the gated 208-cavity small width region simulation is given in Figure 4.2.
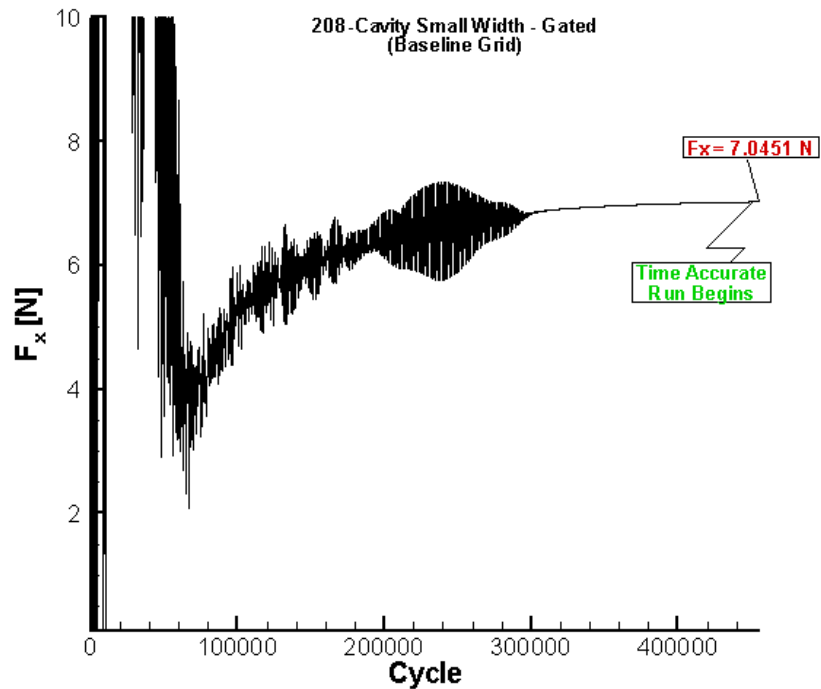
Figure 4.2. Drag Time History Plot for the Gated 208-Cavity Mach 2 Test Case

At 400,000 iterations the simulation was switched to use a time-accurate scheme as shown in Figure 4.2. No difference in the resulting drag value was observed. This is the same behavior (time accurate simulations yielding the same drag values as simulations using local time-stepping, for cases that converged to a steady fixed drag value) that was exhibited in the previous 52-cavity Mach 2 cases.

Pressure contours for the converged simulation are presented in Figure 4.3. The gated 208-cavity case does not have the weak pressure waves originating from each gate location as seen in the gated 52-cavity small width case, at least at the level of resolution of the contours shown. However, the overall trend of increasing pressures match the behaviors noted in previous cases. Again, the local area of highest pressure occurs at the end of the cavity region, on the downstream top wall of the last cavity, where the flow re-

establishes on the trailing flat plate section downstream of the micro-cavity region; this

region is shown enlarged in Figure 4.4.
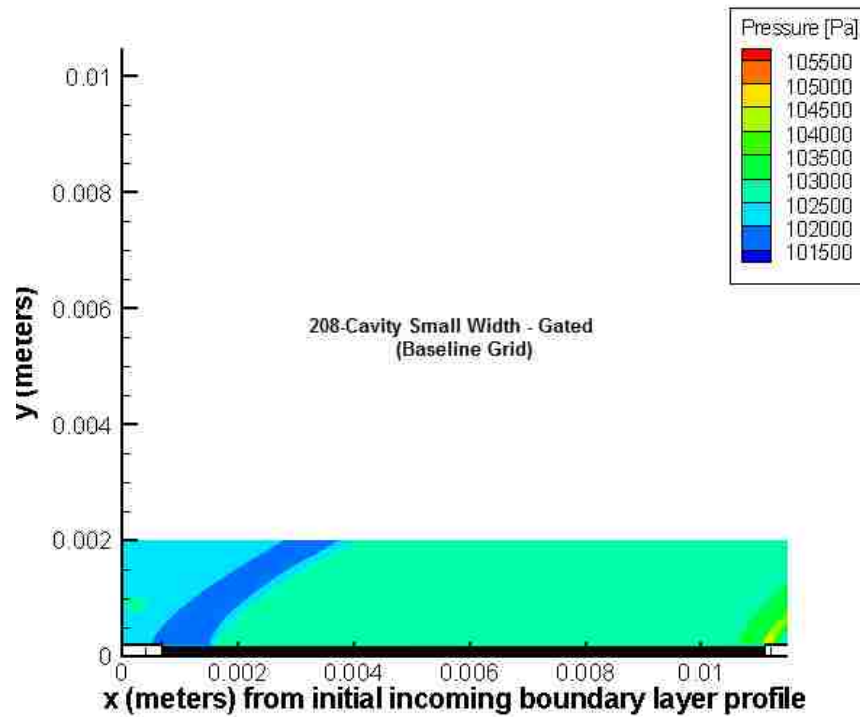
Figure 4.3. Pressure Contours for the Gated 208-Cavity
Small Width Mach 2 Test Case
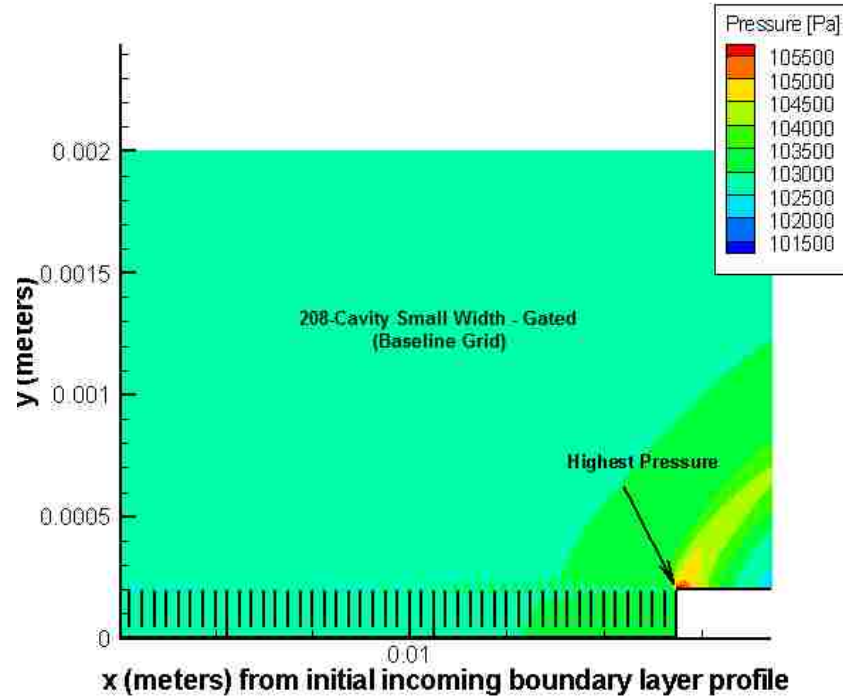
Figure 4.4. Pressure Contours for the Gated 208-Cavity Small Width Case
Enlarged for Detail at the End of the Cavity Region

A small jet of reversed flow is present passing through the cavity wall
perforations, as shown in Figure 4.5. This area corresponds to a negative u-velocity of a
magnitude of about 6 m/s or about 1% of the free-stream velocity, the same magnitude as
seen in the 52-cavity gated case in Section 3. While the magnitude of the reversed flow
jet is very small, it represents an area of negative velocity and therefore actually
contributes very slightly to overall thrust. Streamtraces in Figure 4.5 for an upstream
region from first cavity to first gate show a single and very well-structured flow vortex
that extends throughout all the cavities enclosed by the first gate.
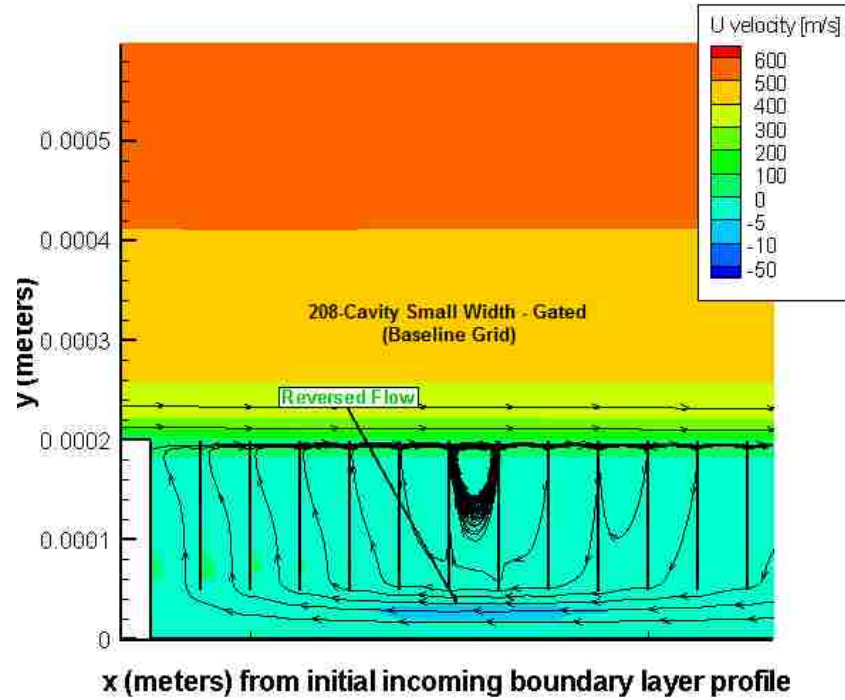
Figure 4.5. U-Velocity Contours and Flow Streamtraces Indicating Reversed Flow in the Cavities Bounded by the First Gate

Further inspection of the flow slightly downstream shows that the region containing cavities between the first gate and the second gate of this flow does not contain a region of reversed flow, shown in Figure 4.6. Instead, the magnitude of the positive u-velocity of flow passing through the perforations in that area is greater than that of flow in other areas of the cavity region. This behavior matches that of the gated 52-cavity case as well. Continuing downstream through the cavity region, flow between gates alternate between reversed and non-reversed flow. The strength of the non-reversed flow decreases with distance downstream.
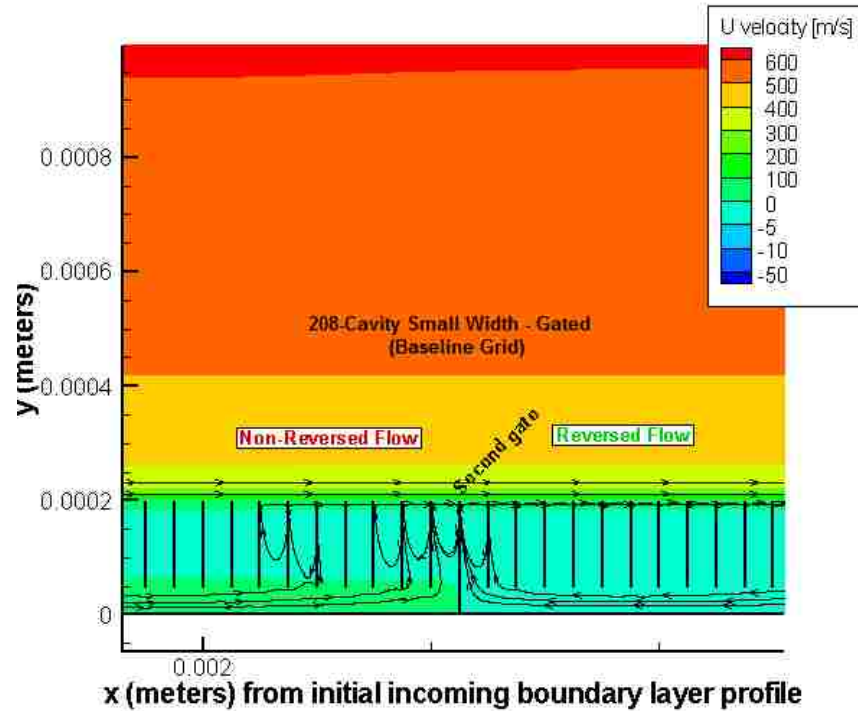
Figure 4.6. U-Velocity Contours and Flow Streamtraces Indicating Both
Reversed and Non-Reversed Flow Near the Second Gate

The distribution of cumulative viscous and pressure drag forces acting on the domain with micro-cavities is shown in Figure 4.7. Overall skin friction drag within the overall micro-cavity region is -0.0011 N, hence representing a contribution to thrust, rather than drag, although extremely small. The actual drag is therefore attributed to the pressure forces acting on the vertical cavity walls. This overall drag force within the cavity region is 6.396 N. Pressure drag shows the same linearly-increasing trend as noted in the 52 cavity case and increases at a rate of 608.424 N/m from beginning to end of the micro-cavity region. This is within 5% of the ~576 N/m relationship observed for the gated 52-cavity small width test case.
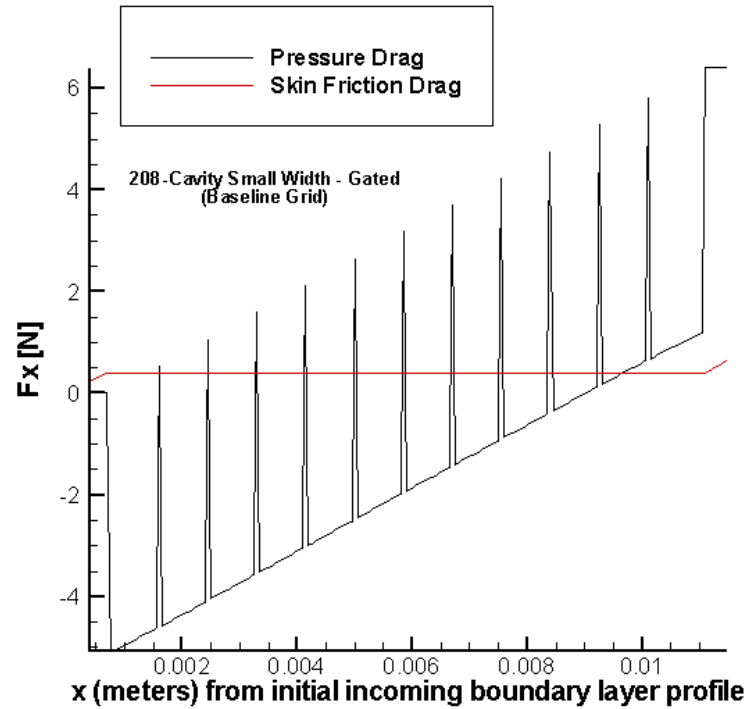
Figure 4.7. Breakdown of the Contributions of Skin Friction and Pressure Forces to Total Drag Over the Gated 208-Cavity Small Width Mach 2 Test Case

Drag totals for the gated 208-cavity test case are presented in Table 4.1. Compared to a reference flat plate of equal length of the cavity region, the micro-cavities exhibit a drag reduction of 16.218%. Note, however, that while for this particular cavity region (with a length of 0.0104 m over the cavities themselves the driven micro-cavities still demonstrate a positive effect on reducing the overall drag, eventually there will be a length (for a set cavity spacing and input conditions) where a reference flat plate will outperform a geometry with embedded micro-cavities in terms of reduced drag. This is because the micro-cavity concept appears (in this study) to exhibit linearly increasing pressure drag, while a flat plate has an exponentially decaying (slowly decaying) skin friction drag (although the decay is very small as measured from a linear relationship).

Table 4.1. 208-Cavity Small Width Drag Results

Case	Viscous Drag [N]	Pressure Drag [N]	Total Drag [N]	Total Drag (Flat Plate) [N]	Drag Reduction [%]
Gated	-0.0011	6.396	6.385	7.621	16.218

5. FINE GRID CASE STUDY

In order to determine the effect of a more refined grid on the results obtained in this investigation, the following case study re-examines baseline grid test cases presented in Section 3 (21 x 21 nodes in each cavity) utilizing a fine grid with 41 x 41 nodes in each cavity (quadruple the grid points as the baseline grid). Due to the high computational expense associated with utilizing a fine grid, only two cases are considered in this section: gated and unperforated, for a free-stream Mach number of 2.0 and small-width cavity configuration. The same CFL and non-time accurate solution scheme used for the baseline grid results presented in Section 3 on the same configurations are used in these fine grid cases.

5.1. GATED FINE GRID RESULTS

The overall drag versus iteration history for the fine grid gated 52 (small-width) cavity simulation is given in Figure 5.1. This plot shows that the solution does not converge to a single value, as seen for the baseline grid cases presented in Section 3. Instead, the computed overall drag value (composed of contributions from skin friction on the upstream and downstream flat plate sections associated with the micro-cavity domain simulations and pressure drag within the micro-cavity region itself) exhibits significant oscillations. However these oscillations clearly bracket a fixed averaged (iteration-averaged) value. This sort of behavior will be referred to (for the purpose of discussion here) as "quasi-steady" convergence. The bottom plot shows a larger view of the detail region of the iteration history that is highlighted in red. The iteration-averaged drag value over the last 8000 iterations is 2.273 N. This drag value is actually within 2%

of the drag value found using the baseline grid for the gated 52-cavity small cavity width test case discussed in Section 3 (which exhibited steady convergence to a fixed value). As described earlier for other cases and seen in the plot, the time-accurate simulation (following the initial local time-stepping simulation) essentially gave the same oscillatory behavior about the same iteration-averaged drag value.
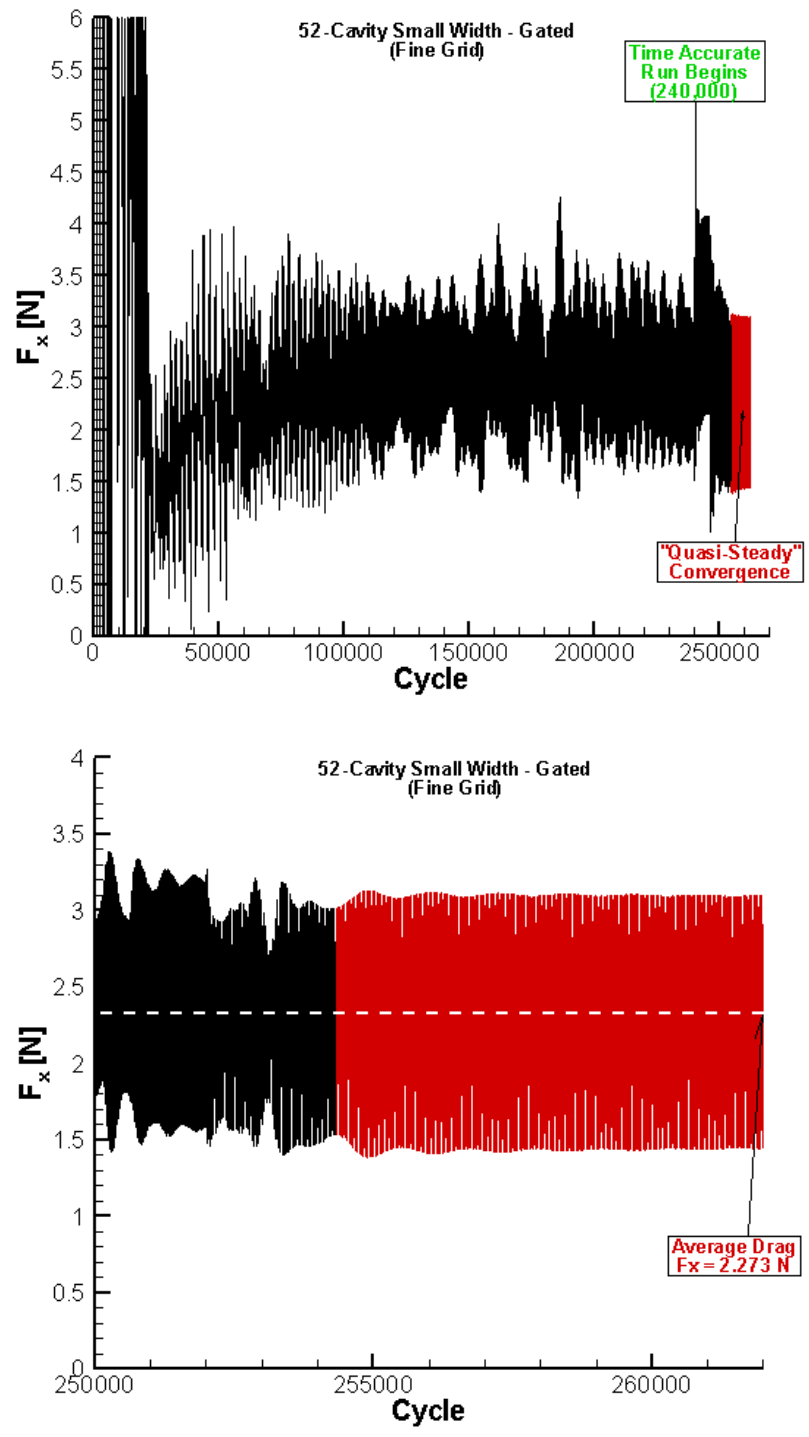
Figure 5.1. Time History Plot (Top) for the Gated 52-Cavity Small Width Mach 2
Test Case Using the 41 X 41 Node Fine Grid, Zoomed for Detail (Bottom)

A snap-shot of the pressure contours for the fine grid simulation at the end of the simulation run, presented in Figure 5.2, show (as expected due to the oscillatory behavior in drag) significantly more variability in pressure and inter-cavity interaction and vortex shedding associated with the cavity region than seen in the steady simulation using the baseline grid. Unlike the baseline grid simulation, in which the location of the highest pressure was seen at the last (downstream) cavity top right wall where the flow re-establishes on the downstream flat plate section, there are articulated repeating zones of higher pressures within the cavities themselves, clearly associated with cavity-to-cavity interactions and shedding of vortices. However, note that the magnitudes of the variations in pressure as seen in these contours are not very large, i.e., the contours, although distinct, actually represent an overall small change in pressure.
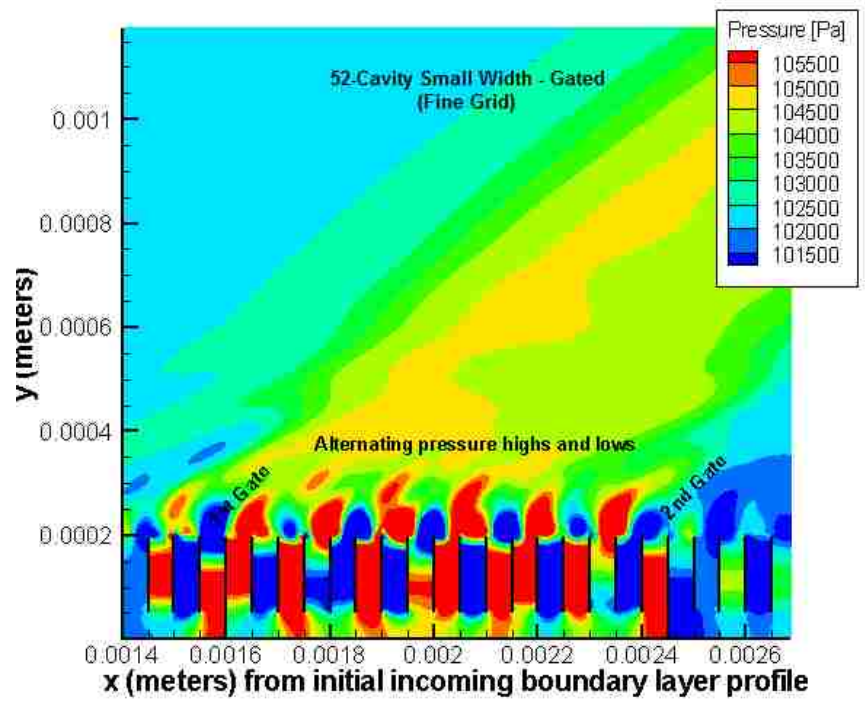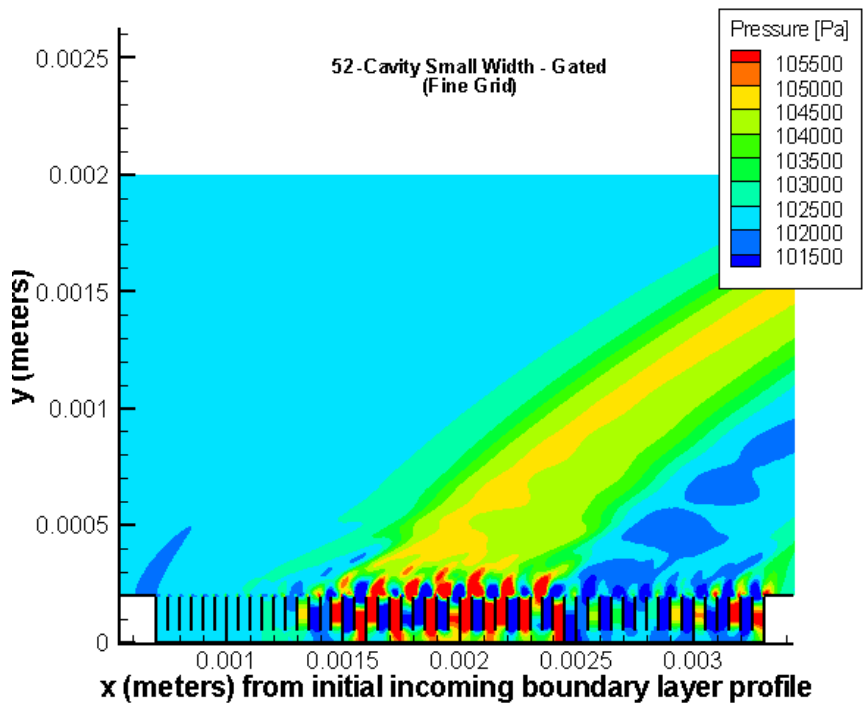
Figure 5.2. Pressure Contours for the Gated 52-Cavity Small Width Geometry Using the 41 x 41 Node Fine Grid (Top) and Enhanced View (Bottom) Over the Region Between Gates

The larger (zoomed) view of the pressure contours within the cavities in Figure 5.2 indicates a clearly defined alternating pattern of high and low pressurization within the cavities themselves, generally alternating between neighboring cavities, or cavity sets. These patterns of over-pressurized and under-pressurized fluid within the cavities are associated with vortex shedding and consequent over-pressurization and under-pressurization of the fluid directly above downstream adjacent cavities (see Figure 5.2). This effect results in a cyclic migration, or translation, of these zones of over-pressurization and under-pressurization along the cavity region, hence the oscillatory nature of the overall drag results about an averaged value.

U-velocity (axial velocity component) contours for this fine grid case (again, representing a time 'snap-shot' of the flow-field) are shown in Figure 5.3 for a portion of the cavity region. A reversed flow 'jet' upstream of the first gate is seen in the lower portion of the cavities, as also seen in the previously discussed baseline grid case. In general, however, there is much less structure and regularity of the flow due to the oscillations discussed above. There is indication of some reversed flow passing through perforations in the cavity vertical walls downstream of the first gate. This is in contrast to the visualization provided by the baseline grid velocity contours in Section 3, in which the flow appeared to be only moving in the downstream (positive x-direction) between the first and second gate.
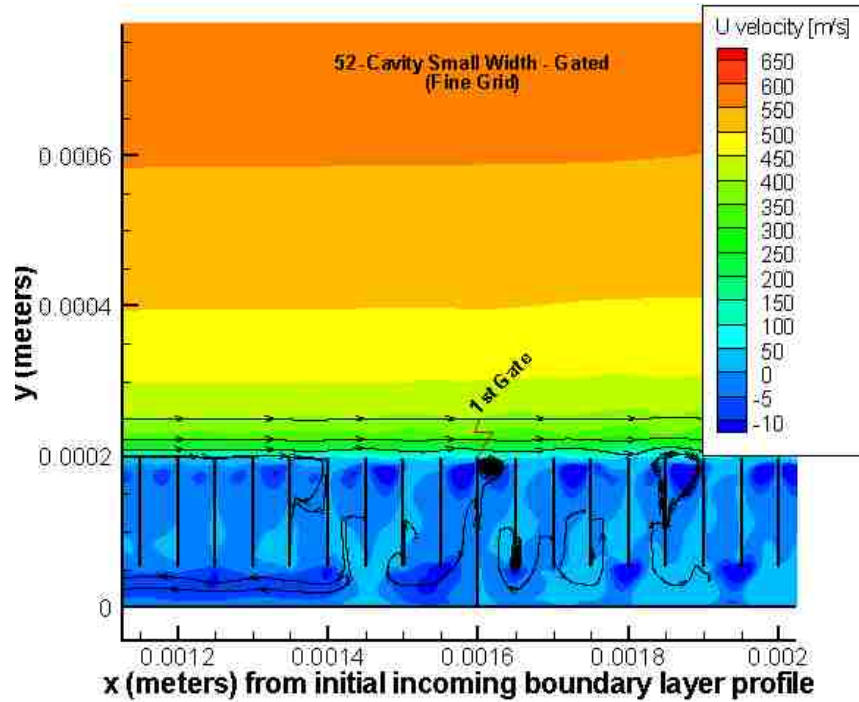
Figure 5.3. U-Velocity Contours of the Fine Grid Gated 52-Cavity
Small Width Mach 2 Test Case

The refinement in the grid for this case (from the baseline grid utilized for the same configuration discussed in Section 3) clearly indicates that the flow is destabilized both temporally and spatially from the baseline grid results predictions. The contours for the fine grid case presented here show upstream-to-downstream regular variability in pressurization between cavities and cavity regions, although pressurization changes are overall fairly small. These variations and associated temporal variability in drag are not seen in the base-line grid simulations shown earlier. This is a cause of concern and will be addressed as an important element for subsequent investigation for the concept studied here. However, it is significant that the iteration-averaged overall drag value for the oscillatory fine-grid simulation is almost the same as the steady baseline grid simulation.

5.2. UNPERFORATED FINE GRID RESULTS

The second fine grid test case for this section corresponded to the same geometry as described in section 5.1, except that the vertical cavity walls were completely unperforated. This time-accurate simulation was initialized using the flow-field obtained at the final iteration in the perforated case described above. The iteration history for overall drag is shown in Figure 5.4 for this case. This plot demonstrates that the flow-field for this case does not appear to reach the same degree of regularized "quasi-steady" convergence as exhibited for the perforated/ gated case. After 280,000 iterations, the time history begins to slightly repeat patterns, but is not as consistent in terms of showing fixed oscillations about an average as shown in the previous case. An iteration average over the last 10,000 iterations yields a drag value of 2.66 N, which is significantly higher than all other 52-cavity small width cases examined in this study.
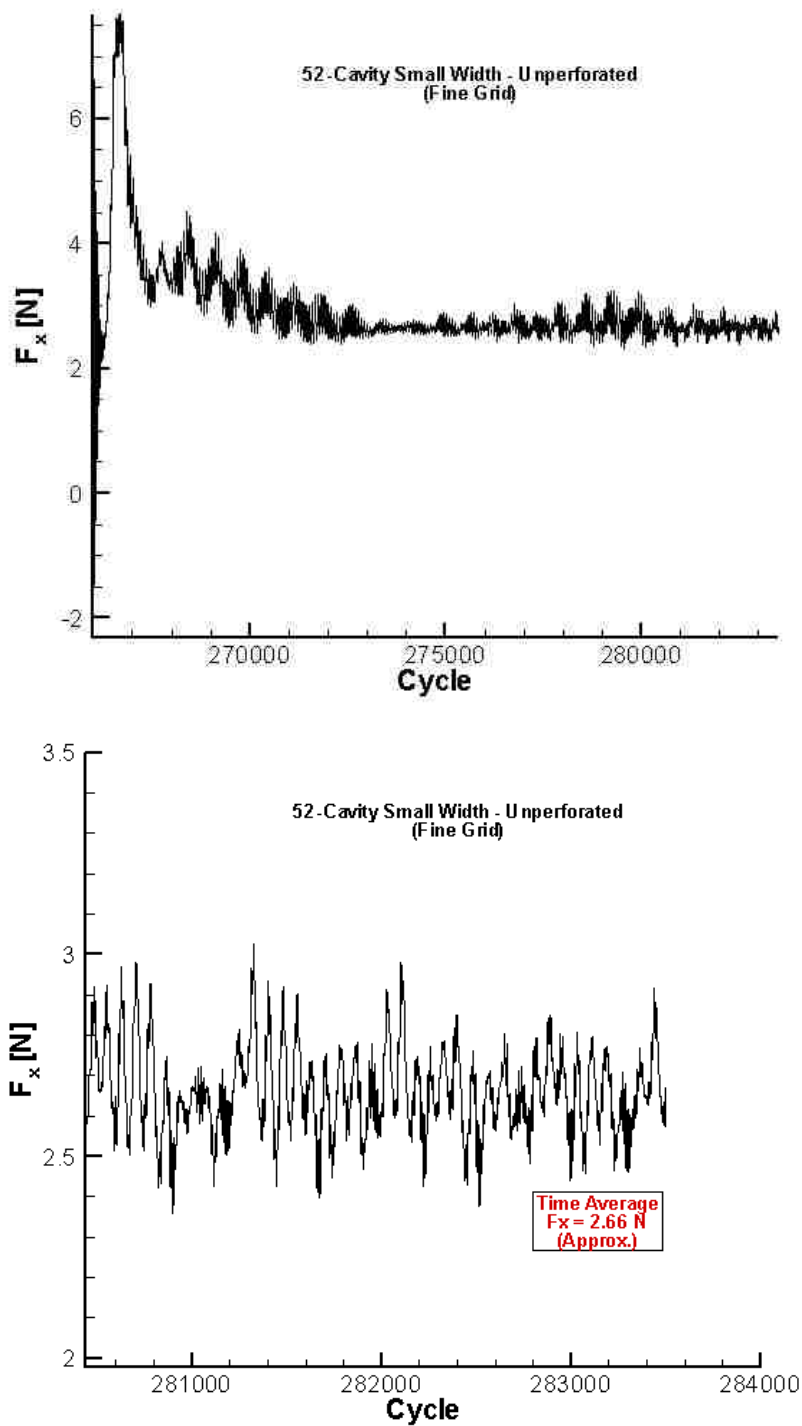
Figure 5.4. Time History Plot (Top) for Unperforated 52-Cavity Small Width
Mach 2 Test Case Using the 41 x 41 Node Fine Grid, Zoomed for Detail (Bottom)

Due to the fact that this fine-grid simulation for the unperforated wall configuration shows no clear convergence to either a fixed drag value or to a definite iteration-averaged value, it is difficult at this time to draw strong conclusions from these results. As no convergence issues were found with the unperforated case using the baseline grid, it cannot be determined with certainty from this case alone whether perforations in the cavity walls contribute to some stabilization of the flow-field. Further study is warranted.

6. CAVITY SPACING, SIZING, AND GRID REFINEMENT STUDY

Whereas the previous sections contain analysis of the physics and visualizations of the flow fields, this section analyzes purely drag reduction potential and flow-field steadiness. The primary focus is to provide information on the effect of the cavity region size, spacing between adjacent cavity walls, number of cavity walls and mesh sizing on the resulting stability of solutions and the total drag values. Simulations are conducted using mesh sequencing on three meshes: coarse, baseline (medium), and fine. Mesh sequencing strategy used for much of the current work takes an input number of nodes on a fine grid (in this case corresponding to 41 x 41 nodes in each cavity), then generates coarser meshes internally by removing every other node on the grid lines. The coarsest grid is then solved for a set number of iterations, and then values are interpolated up to the next finer level, solved again for a set number of iterations, and so forth.

All results in the current section are for elliptically-solved boundary layer regions which are underlaid by driven cavities, with these domains beginning 1.0 m downstream of the leading edge of a flat plate. Free-stream conditions correspond to a static pressure of 26,500 N/m^2 and a static temperature of 223.26 K. The test cases are divided into three general categories in terms of for both cavity physical scale and the free-stream Mach number used: Mach 1.2 flow over medium-width cavities, Mach 1.2 flow over small-width cavities, and Mach 3.0 flow over medium-width cavities.

6.1. MACH 1.2 MEDIUM CAVITY WIDTH

The first case study uses a free-stream Mach number of 1.2 and begins 1.0 m downstream of the leading edge of the flat plate. Figure 6.1 provides a schematic of the

tested geometry. Medium width cavities are modeled with perforated cavity walls with height of perforations of 0.00015 m. These medium width cavity cases correspond to a spacing of 0.000125 m between each cavity wall or cavity region (block) boundary (for cases with removed walls). Height of the overall cavity region is held constant at 0.0005 m, corresponding to a cavity height-to-boundary layer thickness of $H/\delta = 0.040164$. The leading and trailing edges fore and aft of the cavity region are 0.00175 m and 0.001 m in length, respectively. Length of the cavity region itself is given in terms of number of cavities (N cavities), e.g. "2 cavities" corresponds to an overall cavity region equal in length to two cavity widths. Five cases are presented for this geometry, all of which resulted in steady convergence to fixed drag values for all grid levels (and residual drops of seven and more orders of magnitude on all three grid levels). Configurations for these cases are outlined in Table 6.1.
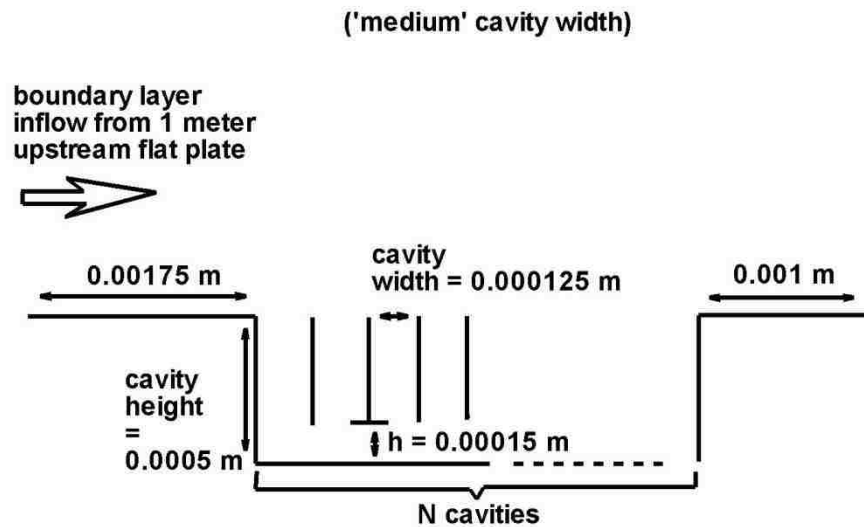
Figure 6.1. Micro-Cavity Region Geometry for Medium Cavity Width Test Case

Table 6.1. Test Case Configuration for Mach 1.2 Medium Cavity Width

Case	Cavities	Wall(s)
R1	2	0
R2	2	1
R3	4	1
R4	6	5
R5	8	7

Each case was run using the mesh sequencing scheme discussed previously. Figure 6.2 is a representative time history plot of drag for the 2-cavity cases R1 and R2. Each of the three meshes converges to a fixed drag value. There is a slight increase from the coarse grid in the baseline case, but for both cases, R1 and R2, no difference is seen between the baseline grid and the fine grid drag values.
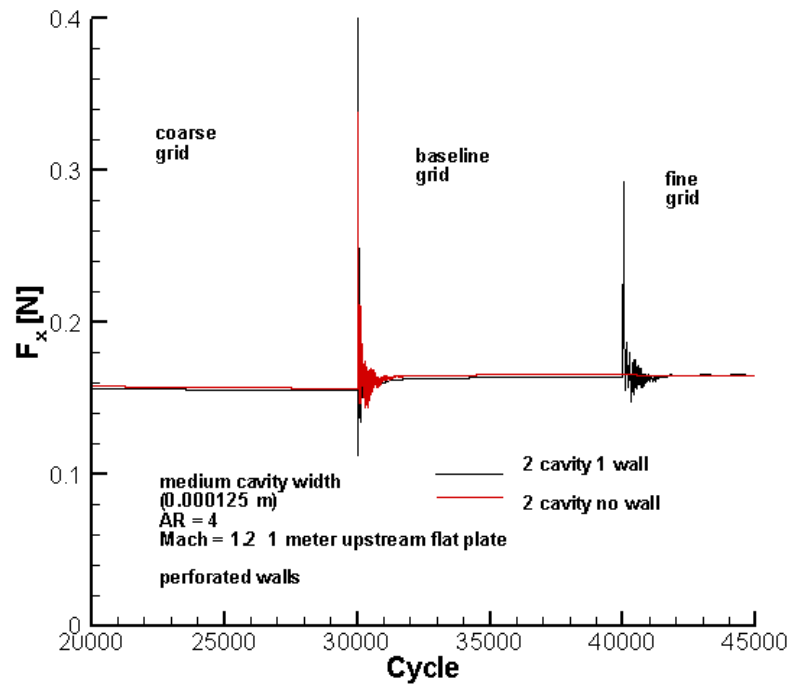
Figure 6.2. Mesh Sequenced Drag Time History Plot for Test Cases R1 and R2

Results that compare the drag characteristics of these cavity cases to reference (flat plate) skin friction drag over the same length of plate are tabulated in Table 6.2. For each of the configurations examined, a reference (unmodified flat plate) total skin friction drag was calculated that includes the leading edge region upstream of the cavity region, the trailing edge region downstream of the cavity region, and the cavity region itself; this is designated Total Drag (ref) in Table 6.2. Further, reference flat plate skin friction drag for only the leading and trailing edge regions in the elliptic domain was computed, designated as LE/TE Drag (ref) in Table 6.2. This allows determination of the reference flat plate skin friction drag for the length of the cavity region alone, designated as Cavity Drag (ref). This reference flat plate drag over the cavity region alone can then be directly

compared to the total drag obtained from the simulation results with cavities, for each case.

Table 6.2. Tabulated Drag Results for Mach 1.2 Medium Width Cavity Test Cases

Case	Total Drag (Ref) [N]	LE/TE Drag (Ref) [N]	Cavity Drag (Ref) [N]	Total Drag (Test) [N]	Cavity Drag (Test) [N]	Drag Reduction [%]
R1	0.177816	0.163	0.01482	0.1665	0.0089	39.95
R2	0.177816	0.163	0.01482	0.1653	0.0094	36.57
R3	0.192634	0.163	0.02963	0.1608	0.0225	24.06
R4	0.207452	0.163	0.04445	0.1601	0.03466	22.02
R5	0.22227	0.163	0.05927	0.1614	0.0484	18.34

The value for cavity drag (test) in Table 6.2 was taken to be only the resulting pressure drag in the region, as skin friction over the cavities was negligible. Figure 6.3 shows the comparisons of reference flat plate skin friction drag values for i) the entire test region (leading edge, trailing edge, and overall cavity region) and ii) the leading and trailing edges only to the results obtained from the VULCAN simulations for the plates with underlying micro-cavities. All five cases exhibited lower drag for the driven cavity configurations, as compared to the flat plate reference values.

**Mach 1.2   1 meter upstream flat plate   'medium width' cavities
(0.000125 m)**
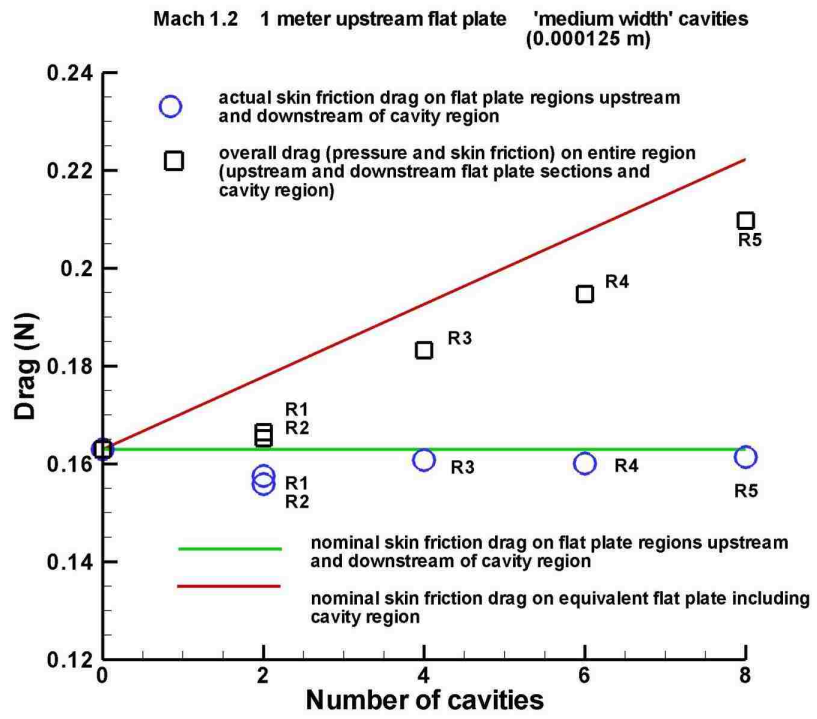
Figure 6.3. Reference-to-Test Drag Value Comparison for Test Cases R1-R5

The delta between the two drag values in Figure 6.3 corresponds to the drag over the cavity region alone, for each test case. The percentage in drag reduction is plotted for each test case in Figure 6.4. The best performing case is R2 (2-cavity, 1 wall) with a total of 39.95% reduction in drag compared to a flat plate of the same length. Each of the test cases exhibits at least an 18% drag reduction. Cases R1 and R2 show that for two cavities of equal length, the introduction of the cavity wall further reduces the total drag over the cavity region.
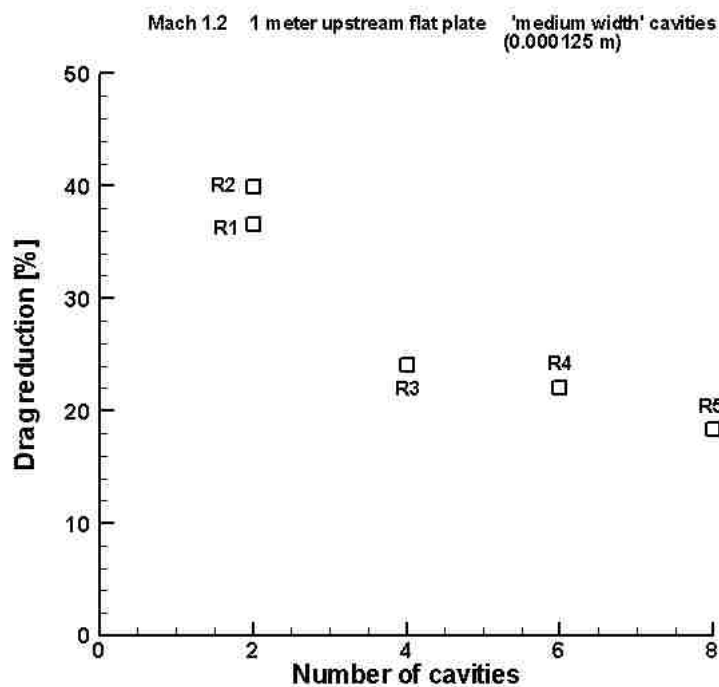
Figure 6.4. Overall Percentage of Drag Reduction for Cases R1-R5

In addition to cases R1-R5, a number of other cases with varied numbers of cavity walls were simulated in order to better develop a relationship between number of internal walls (for a given overall cavity region length) and drag; however, these cases did not exhibit convergence to a fixed drag value. A number of them, however, were quasi-steady solutions, oscillating around a given value, although some were completely divergent. A representative time meshed-sequenced time history plot for 8-cavity cases is given in Figure 6.5. Inspection of the coarse grid data indicates that drag does continue to decrease with increasing number of cavity walls; however the baseline and fine grid values show a general lack of convergence for nearly all cases, rendering further analysis on those cases extraneous. Only the 8-cavity, 7-wall case exhibits solid convergence to a

single value, indicating that increasing number of walls not only decreases drag, but contributes to stability in the solution.
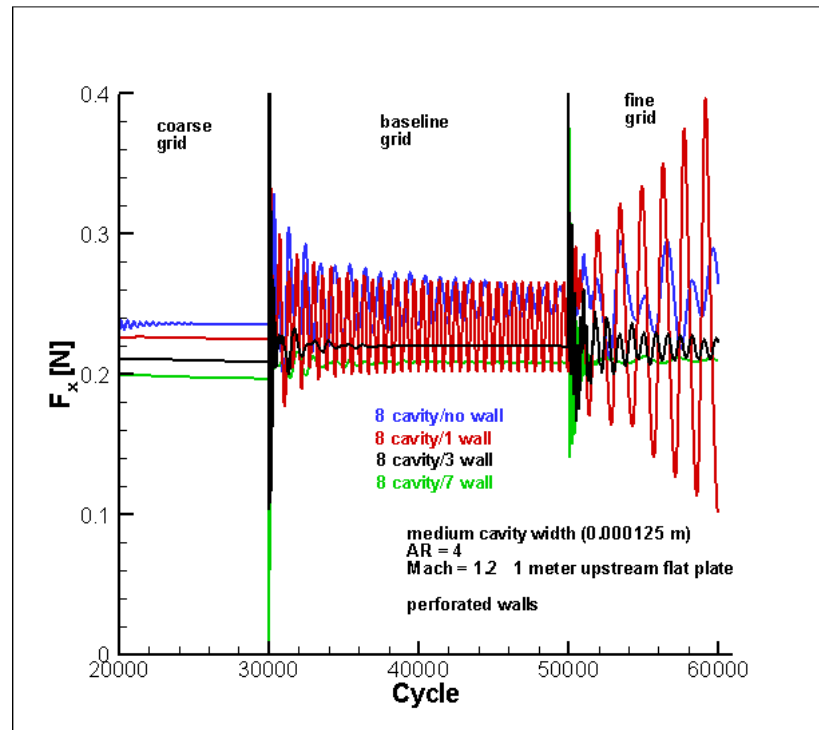
Figure 6.5. Mesh-Sequenced Time History Plot for 8-Cavity Configuration

Time behavior of all of the Mach 1.2 medium cavity width cases is presented in Figure 6.6. Cases are classified in one of three ways: steady (denoted by S), oscillatory (denoted by O), and unsteady (denoted by U). For a constant number of walls, unsteadiness becomes more prevalent as the number of cavities increased. Further, for a constant number of cavities, cases demonstrate greater stability with increasing number of walls.
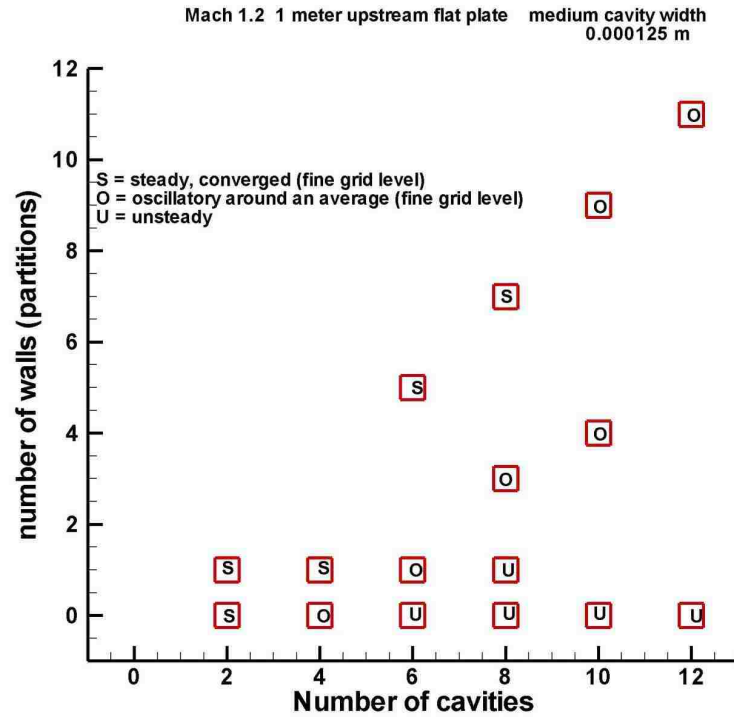
Figure 6.6. Level of Steadiness for All Mach 1.2 Medium Cavity Width Cases

6.2. MACH 1.2 SMALL CAVITY WIDTH

The second case study in this section examines flow over a similar geometry as the previous study, but with a reduced cavity width, height, and leading/trailing edge plate lengths. Free-stream Mach number is maintained at 1.2, free-stream temperature and pressure are kept at 223 K and 26,500 N/m^2, respectively. The 'small cavity width,' is used here, corresponding to individual cavity regions of width 0.00005 m (0.005 cm) and a cavity height of 0.0002 m. This corresponds to a cavity height-boundary layer thickness ratio of H/δ = 0.016066, meaning that the cavity region height is 1.6% of the boundary layer thickness. A schematic of the geometry dimensions is provided in Figure 6.7. The same incoming boundary layer profile and free-stream conditions used in the test cases in the previous section are used for the small cavity width test cases.
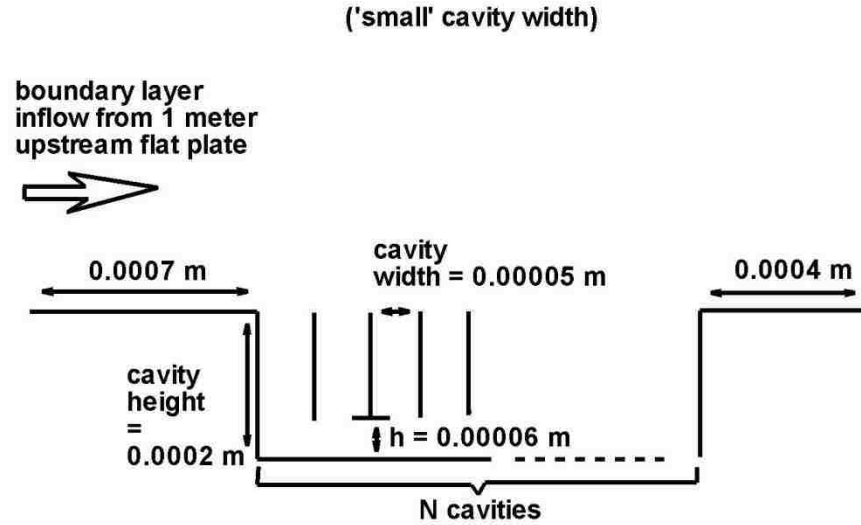
Figure 6.7. Micro-Cavity Region Geometry for Small Cavity Width Test Case

Two test cases are considered for the small cavity width configuration, outlined in Table 6.3. The term 'gates' refers to a cavity wall where h = 0 m, i.e., there is no perforation in the cavity wall. The gates are spaced at even intervals through the cavity region.

Table 6.3. Test Case Configuration for Mach 1.2 Small Cavity Width

Case	Cavities	Walls	Gates
S1	52	51	2
S2	208	207	11

Time history plots for the two cases are presented in Figure 6.8 and 6.9. Both cases converge to a fixed drag value. This value increases slightly with each refinement of the grid though the baseline and fine grid values differ only slightly. Increases from the

coarse grid to the baseline occurred in the previous case study for medium width cavities as well. This suggests that while the coarse grid is slightly underestimating the total drag value, with each grid refinement, the solution is asymptotically approaching a fixed value.
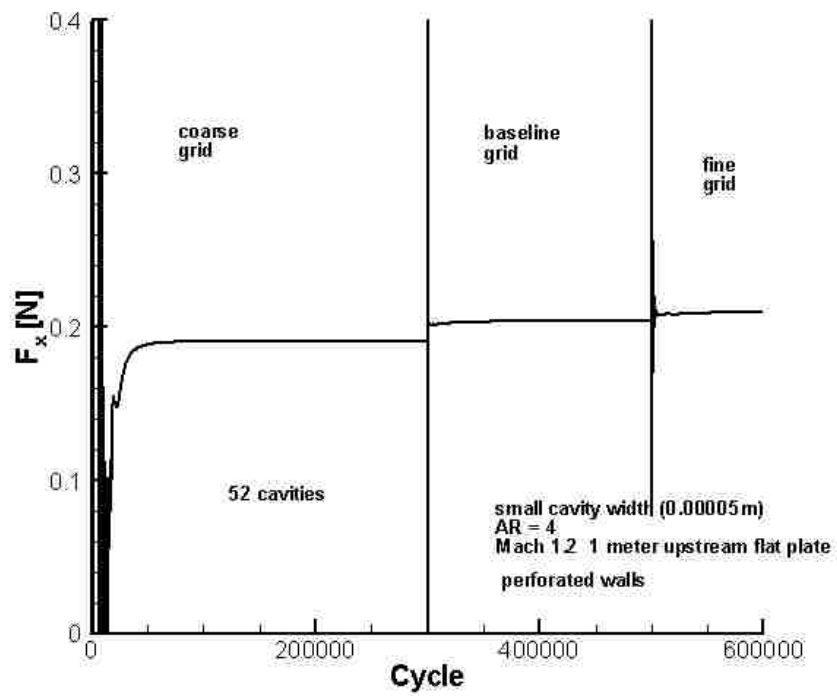
Figure 6.8. Case S1 Drag Time History Plot
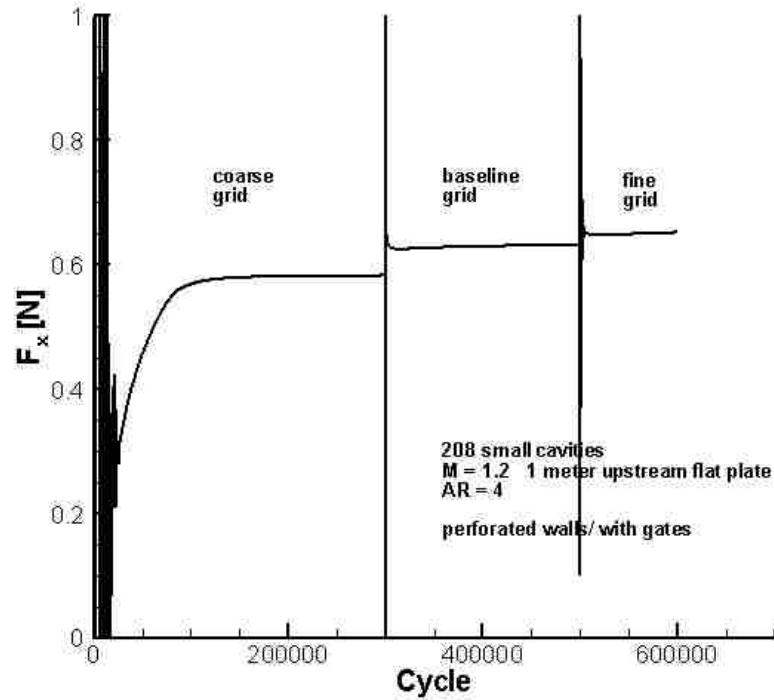
Figure 6.9. Case S2 Drag Time History Plot

Reference flat plate skin friction drag values for comparison are computed using the same procedure as previously described for the medium cavity width cases. The full tabulated results for the two test cases are given in Table 6.4. As with the R1-R5 cases, the skin friction over the cavity region itself was found to be negligible, so the cavity drag (test) value in Table 6.4 includes only the pressure drag obtained in the simulations.

Table 6.4. Tabulated Drag Results for Mach 1.2 Small Width Cavity Test Cases

Case	Total Drag (Ref) [N]	LE/TE Drag (Ref) [N]	Cavity Drag (Ref) [N]	Total Drag (Test) [N]	Cavity Drag (Test) [N]	Drag Reduction [%]
S1	0.2193064	0.0652	0.1541	0.2099	0.1437	6.749
S2	0.6816281	0.0652	0.61643	0.652	0.5859	4.953

Both test cases with micro-cavities performed better than the reference unmodified flat plate; however, the percentage reduction in drag was significantly less than that observed in the medium width test cases with the same incoming flow profile. S1 achieves nearly 7% reduction in drag while S2 achieves about 5%. Despite the reduced cavity width presented in Case S1 and S2, the number of cavities is high enough such that the overall length of the cavity region is greater than that of any of the R1-R5 cases. This further demonstrates the trend that as the number of cavities increase, the overall percentage of drag reduction decreases as seen in the 208-Cavity Mach 2 case presented in Section 4. Fundamentally speaking, this makes sense as the coefficient of friction, c_f, for a flat plate decreases with distance along the plate, while the pressure drag associated with cavities demonstrates approximately (at best) a linear increase with distance along the plate. Based on this observation, at some point, the reference flat plate skin friction drag will eventually reach a value low enough such that the benefit of the cavity region disappears. The characteristic of the linearity of the observed pressure drag in the micro-cavity regions will be discussed at length in a subsequent section.

6.3. MACH 3.0 MEDIUM CAVITY WIDTH

The third case study in this section uses the same medium cavity width geometry and grid as is presented in Figure 6.1, with free stream Mach number corresponding to 3.0 (recall that a fixed boundary layer profile is used at elliptic domain inflow, as obtained from an upstream 1 meter flat plate simulation) with a corresponding cavity height-to-boundary layer thickness ratio of $H/\delta = 0.043994$. Free-stream temperature and pressure values are 223 K and 26,500 N/m^2, respectively. A total of eight test cases are

presented for this configuration; these cases are listed in Table 6.5. Multiple parameters are varied in the Mach 3.0 test cases, including perforation height. Additionally, very fine mesh sizing, time accuracy, and unperforated configurations are investigated. Steady convergence was achieved for all of the test cases in which drag results are presented. Resulting drag values are tabulated in Table 6.6.

Table 6.5. Test Case Configuration for Mach 3.0 Medium Cavity Width

Case	Cavities	Walls	Notes
T1	12	11	
T2	12	11	Unperforated (h = 0 for all walls)
T3	12	11	h = 0.00025 m (50% of cavity height)
T4	12	11	Very fine grid (161 x 41 nodes in each cavity)
T5	12	11	Time accurate solution
T6	52	51	2 gates, equally spaced, 17th and 34th wall location
T7	52	51	
T8	52	51	Unperforated (h = 0 for all walls)

Table 6.6. Tabulated Drag Results for Mach 3.0 Medium Width Cavity Test Cases

Case	Total Drag (Ref) [N]	LE/TE Drag (Ref) [N]	Cavity Drag (Ref) [N]	Total Drag (Test) [N]	Cavity Drag (Test) [N]	Drag Reduction [%]
T1	0.6164	0.62975	0.3425	0.8944	0.278	18.832
T2	0.6286	0.62975	0.3425	0.9006	0.272	20.584
T3	0.6208	0.62975	0.3425	0.8956	0.2748	19.766
T4	0.6131	0.62975	0.3425	0.8866	0.2735	20.146
T5	0.6166	0.62975	0.3425	0.8961	0.2795	18.394
T6	0.6178	0.62975	1.4885	1.976	1.3582	8.754
T7	0.6034	0.62975	1.4885	1.9747	1.3713	7.874
T8	0.6347	0.62975	1.4885	1.9838	1.3491	9.365

Drag is reduced in all eight test cases compared to reference flat plates of equal length, ranging from 8% to over 20%. Case T1 and T5 are identical with respect to geometry and configuration. The only difference is that T5 is a time-accurate solution as opposed to the local time-stepping. Despite the change in the time scheme, no significant difference exists between the two results. The very fine grid (within the cavity regions) in T4 shows only a ~1% change in drag reduction compared to T1. It is significant that simulation using the very fine grid examined in this test case still converged to a fixed drag value, i.e., exhibited no oscillatory behavior. Best performance is obtained in the unperforated test cases in both the 12-cavity and 52-cavity cases (T2 and T8). Case T3 with perforations spanning 50% of the cavity height outperformed Case T1 with the original perforation height. Finally, the gated T6 case performs ~1% better than T7 which is completely ungated. Figure 6.10 shows graphically the percentage reductions for each test case.
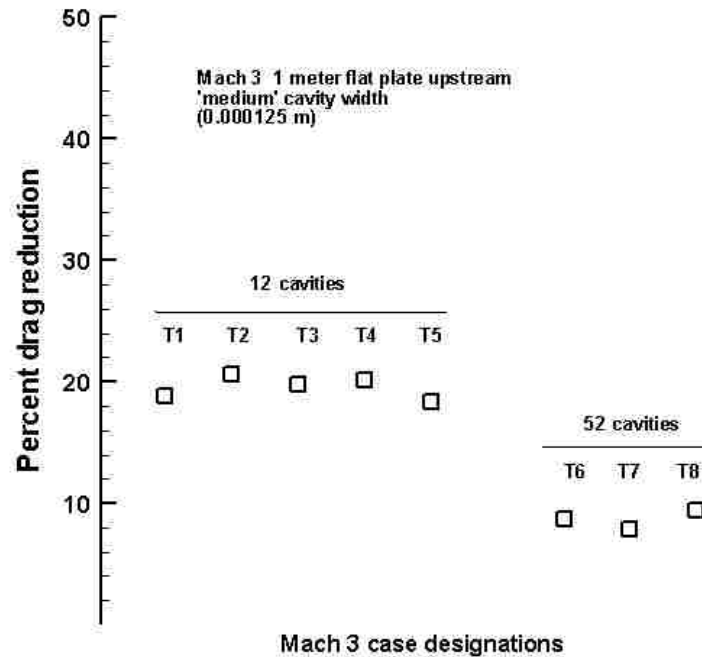
Figure 6.10. Overall Percentage of Drag Reduction for Cases T1-T8

The Mach 3.0 case study results in Figure 6.10 show the lower overall percentage of drag reduction for the 52-cavity cases vs. the 12-cavity case. This agrees with the previous trends seen in this work. Test cases T1-T8 provide further insight into the potential differences between gated, ungated, and unperforated cavity walls. Slightly higher differences in drag are present in these cases as opposed to Section 3 results. Further study on the perforations is needed to better ascertain the drag reduction potential and potential added stability provided for varied geometry and flow conditions.

7. SUMMARY AND CONCLUSIONS

In this investigation, the VULCAN CFD code was used to analyze fluid dynamic drag effects and flow details for driven micro-cavities downstream and beneath compressible turbulent boundary layer flows. This entailed the simulation of representative upstream flat plate boundary layers for various free-stream Mach numbers and upstream plate lengths. Boundary layers from these upstream simulations were then used as the inflow profiles for fully elliptic domains containing various configurations of embedded driven micro-cavities. These configurations consisted of embedded thin-walled cavities oriented transverse to the direction of the flow, which allowed two-dimensional simulations in the present study.

After initial upstream flat plate simulations were completed, a detailed study of the flow physics and drag performance was then conducted on a 52-cavity geometry with a baseline 21 x 21 node (in each cavity) grid using the inflow boundary layer profiles as generated over a 10 cm flat plate for free-stream Mach numbers of Mach 1.2 and Mach 2.0. The test configurations for this study were divided into three categories based on geometry of the cavity walls: gated (perforations through all vertical cavity walls, with the exception of two equally spaced non-perforated walls, both extending the entire cavity height), ungated (perforated vertical walls used throughout the entire cavity region), and unperforated (no perforations in any vertical cavity walls). The study showed that all three configurations yielded approximately an 18% reduction in overall drag as compared to a reference flat plate of equal length. Skin friction drag in all cases was reduced to near-zero, with most cases showing a negative drag contribution (a net gain in thrust). Pressure drag in the region with cavities increased linearly with axial distance.

Cavity wall perforations and gating were shown to have little impact on the net drag results for this case study. All cases exhibited essentially the same total drag value; distributions along the cavity region length for the separate contributions of skin friction drag and pressure drag were analyzed for all cases. Reversed flow jets penetrating through the perforations of the vertical walls were observed in both gated and ungated cases, contributing to improved skin friction drag reduction over the unperforated case; however, the pressure drag in these cases also increased, negating the improved skin friction reduction. Mach 2.0 cases all exhibited steady convergence to a fixed drag value for the baseline grid. No difference was observed in the fixed drag value achieved when switching between local time-stepping and time-accurate solution methodologies. Test cases with the reduced free-stream Mach number of 1.2 only showed steady convergence for one of the three test configurations; specifically the unperforated vertical wall case. Only quasi-steady convergence (oscillatory variance about a given drag value) was obtained for the gated and ungated cases, rendering meaningful analysis of the drag results difficult. Such unsteadiness issues further arose when refining the mesh (quadrupling the number of nodes) for the Mach 2.0 cases. Steady convergence to a fixed drag value was not obtained for any wall configuration in the 52-cavity geometries for these particular fine grid cases. These quasi-steady and non-convergent results require further study and analysis in future works as variability in stability/instability characteristics observed in this investigation is of concern in assessing degree of grid convergence using driven micro-cavities.

A parametric case study in terms of variations in cavity length, number of cavities, vertical wall spacing, and grid refinement was then conducted for turbulent

Mach 1.2 and Mach 3.0 flows, with the cavity region beginning 1 meter downstream of the leading edge of the flat plate. Compared to a reference flat plate, drag was reduced for the Mach 1.2 cases by as much as 40% for 2-cavity geometries. Drag reduction potential was found to decrease with increasing cavity number (corresponding to overall length of the cavity region for a given cavity width). Mach 3.0 cases using 52-cavity configurations exhibited drag reductions from 8-20% with the best performance shown in the unperforated case and ungated cases. This study showed that for a fixed number of cavity regions (corresponding to an overall length of the cavity region itself for a given geometry of individual cavity regions) the degree of steadiness of the solution improved with increasing number of vertical cavity walls. Further, the overall percentage of drag reduction from that of a reference flat plate decreased as the number of cavities, i.e. the length of overall region with micro-cavities, increased. Slight increases in overall drag were exhibited in the mesh sequencing strategy used for the parametric study as the grid became more refined through three grid levels (coarse, base-line, and fine). A number of test cases demonstrated a transition to quasi-steady oscillations about an average value of overall drag, as mesh refinement was increased.

This investigation indicates that all driven micro-cavity test geometries that converged to a fixed overall drag value were superior in terms of providing less overall drag when compared to a reference flat plate of the same length under the same flow conditions. Skin-friction drag was reduced to near-zero values in cavity regions for all test cases and, in most cases, showed net contributions to thrust, although these negative skin friction values were very small. The dominant source of drag over the cavity region was caused by pressure acting in the axial direction on vertical cavity walls. No

appreciable difference was observed in using local time-stepping vs. time-accurate solution schemes. Further study is needed to understand and possibly control or eliminate the divergent and oscillatory behavior exhibited in the reduced Mach number and in fine grid resolution cases and is the subject of ongoing work.

Other topics that need to be examined regarding the concept of driven micro-cavities include analysis of the feasibility of manufacturing and optimization of the concept. The feasibility of and/or costs associated with manufacturing representative micro-cavity geometries was not addressed in this investigation. For the purposes of the current analysis, vertical walls in the cavity region were taken to be infinitely thin. With respect to CFD simulations, this assumption allows for a preliminary fluids-based proof of concept for the driven micro-cavity technique; however, it has no practicality from the standpoint of manufacturability. Further studies could potentially examine the effects of finite thickness vertical cavity walls as well as the manufacturing capabilities required to generate the detailed micro-cavity geometries at the extremely small scales necessary. Systematic optimization of parameters such as cavity spacing, perforation height, etc. was also not done in this study. All test geometries used equally-spaced cavity walls, fixed aspect ratio, evenly-distributed gates, and uniform perforation heights. There remain a significant number of related concepts, or variations on the overall concept of driven micro-cavities, that need to be further examined. Such studies might include the effects of varied perforation heights and perforation patterns as well as optimization of gate locations and cavity spacing on the overall drag reduction performance.

APPENDIX A.

SAMPLE VULCAN INPUT DECK

```
$*******************************************************************$
$******************* Beginning of general control data **************$
$*******************************************************************$
$------------------ Parallel processing control data ---------------$
PROCESSORS               16.0   (No. of cpus to use)
MESSAGE MODE              0.0   (Message passing strategy: 0=stnd.,
1=buffered)
$----------------- Geometric model type ----------------------------$
TWOD                      1.0   (twod, axisym, threed)
$------------------ Grid file data ---------------------------------$
GRID FORMAT       3.0   (1=s.b.form, 2=s.b.bin., 3=m.b.form.,
4=m.b.bin.)
GRID                      0.0   (0=plot3d->3d ; plot2d->2d/axi, 1=plot3d-
>all)
gridvulcansqueeze.grd
GRID SCALING FACTOR  1.0   (Converts grid units to meters)
$------------------ Restart file data ------------------------------$
RESTART OUT              1.0
restartcavebar1.restart
RESTART OUT INTERVAL  500.0
$----------------- Output control data ----------------------------$
WARNING MESSAGES         0.0   (0=none, 1=wall funct., 2=temp. limit,
3=both )
PLOT ON                   3.0   (1=s.b.frm., 2=s.b.unfrm., 3=m.b.frm.,
4=m.b.unfrm.)
PLOT NODES               0.0   (Create PLOT3D files using data averaged to
the nodes)
PLOT FUNCTION            8.0   (Create PLOT3D function file containing
variables below)
DENSITY
VELOCITY
PRESSURE
TEMPERATURE
MACH NO.
LAM. VIS.
EDDY VIS. RATIO
GAMMA
$------------------ Gas thermo, diffusion, and reaction model data --$
GAS/THERMO MODEL    1.0   (0=CPG, 1=TPG, 2=n/a)
CHEMISTRY MODEL      0.0   (0=frozen, 1=finite rate, 2=n/a)
IMPLICIT CHEMISTRY   0.0   (0 or 1=analytical jacobian, 2=numerical
jacobian)
GLOBAL VISCOUS       0.0   (solve the Navier-Stokes equations)
$------------------ Transport model data --------------------------$
VISCOSITY MODEL      1.0   (1=Sutherlands law)
CONDUCTIVITY MODEL   0.0   (0=Prandtl no., 1=Wassilej's law)
UNIV. GAS CONST.      8314.34
NO. OF CHEMICAL SPECIES   2.0
/share/apps/Vulcan/Ver_6.2.0/Data_base/gas_mod.Lewis_3
N2       O2
0.7686   0.2314
$------------------ Reference condition data ----------------------$
ANGLE REF. FRAME     0.0   (0=alpha in xy plane, 1=alpha in xz plane)
ALPHA                     0.0   (angle of attack measured C.C.W in degrees)
NONDIM                    1.0   (0=non.dimen., 1=dimen. static, 2=dimen.
total)
MACH NO.                  2.0
```

```
STATIC TEMP.         288.0
STATIC PRESS.        101325.0
LAM. PRANDTL NO.     0.72
LAM. SCHMIDT NO.     0.22
TURB. PRANDTL NO.    0.90
TURB. SCHMIDT NO.    0.90
$------------------ Turbulence Model Data -------------------------$
TURB. MODEL
     MENTER-SST   (SPALART, MENTER, MENTER-SST, K-OMEGA)
     TURB. INTENSITY     0.01
     TURB. VISC. RATIO   0.10
     BOUSSINESQ REY. STRESS      0.0
     NO 2/3 RHOK IN REY. STRESS  0.0
$------------------ Runge-Kutta scheme coefficients ----------------$
NSTAGE               3.0    (no. of Runge-Kutta Stages)
0.333333333333, 0.5, 1.0
$------------------ Boundary and cut control ----------------------$
FLOWBCS              219.0  (no. of boundary conditions to be
specified)
CUTBCS               103.0  (no. of C(0) connectivity conditions to be
specified)
BCGROUPS             7.0    (no. of boundary condition groupings)
PATCHBCS             0.0    (no. of non-C(0) connectivity conditions to
be specified)
IGNITION SUB-BLOCKS  0.0    (no. of ignition sub-blocks)
BLOCKS               55.0   (no. of blocks)
BLOCK CONFIG.        55.0   (no. of lines of block configurations
input)
BLK I-STRESS J-STRESS K-STRESS   TURB   PLOT SOLVER REGION
1    T        T        N         Y         Y    E/A    1
2    T        T        N         Y         Y    E/A    1
3    T        T        N         Y         Y    E/A    1
4    T        T        N         Y         Y    E/A    1
5    T        T        N         Y         Y    E/A    1
6    T        T        N         Y         Y    E/A    1
7    T        T        N         Y         Y    E/A    1
8    T        T        N         Y         Y    E/A    1
9    T        T        N         Y         Y    E/A    1
10   T        T        N         Y         Y    E/A    1
11   T        T        N         Y         Y    E/A    1
12   T        T        N         Y         Y    E/A    1
13   T        T        N         Y         Y    E/A    1
14   T        T        N         Y         Y    E/A    1
15   T        T        N         Y         Y    E/A    1
16   T        T        N         Y         Y    E/A    1
17   T        T        N         Y         Y    E/A    1
18   T        T        N         Y         Y    E/A    1
19   T        T        N         Y         Y    E/A    1
20   T        T        N         Y         Y    E/A    1
21   T        T        N         Y         Y    E/A    1
22   T        T        N         Y         Y    E/A    1
23   T        T        N         Y         Y    E/A    1
24   T        T        N         Y         Y    E/A    1
25   T        T        N         Y         Y    E/A    1
26   T        T        N         Y         Y    E/A    1
27   T        T        N         Y         Y    E/A    1
28   T        T        N         Y         Y    E/A    1
```

```
29    T         T      N        Y          Y      E/A    1
30    T         T      N        Y          Y      E/A    1
31    T         T      N        Y          Y      E/A    1
32    T         T      N        Y          Y      E/A    1
33    T         T      N        Y          Y      E/A    1
34    T         T      N        Y          Y      E/A    1
35    T         T      N        Y          Y      E/A    1
36    T         T      N        Y          Y      E/A    1
37    T         T      N        Y          Y      E/A    1
38    T         T      N        Y          Y      E/A    1
39    T         T      N        Y          Y      E/A    1
40    T         T      N        Y          Y      E/A    1
41    T         T      N        Y          Y      E/A    1
42    T         T      N        Y          Y      E/A    1
43    T         T      N        Y          Y      E/A    1
44    T         T      N        Y          Y      E/A    1
45    T         T      N        Y          Y      E/A    1
46    T         T      N        Y          Y      E/A    1
47    T         T      N        Y          Y      E/A    1
48    T         T      N        Y          Y      E/A    1
49    T         T      N        Y          Y      E/A    1
50    T         T      N        Y          Y      E/A    1
51    T         T      N        Y          Y      E/A    1
52    T         T      N        Y          Y      E/A    1
53    T         T      N        Y          Y      E/A    1
54    T         T      N        Y          Y      E/A    1
55    T         T      N        Y          Y      E/A    1
REGION CONFIG.       1.0   (no. of regions the blocks are grouped into)
$******************* Region 1   control input
************************$
ROE    KAPPA     LIMITER     LIM-COEF        ENTRP(U)       ENTRP(U+a)
      3, 3, 3,  4, 4, 4,  2.0, 2.0, 2.0,  1.0, 1.0, 1.0,  1.0, 1.0, 1.0
FMGLVLS  NITSCG1  NITSCG2  NITSFG  #1ST-ORD.-C.G./ITER.  RES.;REL.,ABS.
   1      50000                        0            -10.0   -
10.0
MG-CYCLE   COARSE GRIDS  DQ-SMOOTH  DQ-CORR  DAMP-MEAN  DAMP-TURB
   I           0          0.25       0.50      1.0        0.5
TURB CONVECTION  DT RATIO  NON-EQUIL  POINT-IMP  COMP MODEL  CG WALL BC
    1ST            0.1       25.0        N          N          STW
SCHEME TIME STEP  IT-STATS  CFL-MIN  ADP-CFL  #CFL-VAL  VISC-DT  IMP-BC
REG-REST
 DAF  LOCAL        10        0.1       Y         5        Y        N
Y
   1   5000    10000  20000  800000
 0.1   0.1     0.5    1.0    1.0
!****************** End of general control data *****************!
BC GROUPS: NAME         TYPE         OPTION
           AIR-IN1      PROFILE      PHYSICAL
           AIR-IN2      PROFILE      PHYSICAL
           AIR-IN3      PROFILE      PHYSICAL
           AIR-IN4      PROFILE      PHYSICAL
           ADB-WALL     AWALL        PHYSICAL
           FARFIELD     EXTRAP       PHYSICAL
           OUTFLOW      EXTRAP       PHYSICAL
BC NAME  BLK  FACE  PLACE DIREC1 BEGIN  END  DIREC2 BEGIN  END  IN-
ORDER
AIR-IN1   1    I    MIN    J     1     46    K    MIN   MAX      0
```

```
outbackmarchbase1.prf                    J      MIN   MAX    K      MIN   MAX
AIR-IN2     1    I    MIN    J    46    91    K      MIN   MAX    0
outbackmarchbase2.prf                    J      MIN   MAX    K      MIN   MAX
AIR-IN3     1    I    MIN    J    91    136   K      MIN   MAX    0
outbackmarchbase3.prf                    J      MIN   MAX    K      MIN   MAX
AIR-IN4     1    I    MIN    J    136   MAX   K      MIN   MAX    0
outbackmarchbase4.prf                    J      MIN   MAX    K      MIN   MAX
ADB-WALL    1    J    MIN    I    MIN   MAX   K      MIN   MAX    0
ADB-WALL    2    J    MIN    I    MIN   MAX   K      MIN   MAX    0
ADB-WALL    3    J    MIN    I    MIN   MAX   K      MIN   MAX    0
ADB-WALL    4    J    MIN    I    MIN   MAX   K      MIN   MAX    0
ADB-WALL    5    J    MIN    I    MIN   MAX   K      MIN   MAX    0
ADB-WALL    6    J    MIN    I    MIN   MAX   K      MIN   MAX    0
ADB-WALL    7    J    MIN    I    MIN   MAX   K      MIN   MAX    0
ADB-WALL    8    J    MIN    I    MIN   MAX   K      MIN   MAX    0
ADB-WALL    9    J    MIN    I    MIN   MAX   K      MIN   MAX    0
ADB-WALL    10   J    MIN    I    MIN   MAX   K      MIN   MAX    0
ADB-WALL    11   J    MIN    I    MIN   MAX   K      MIN   MAX    0
ADB-WALL    12   J    MIN    I    MIN   MAX   K      MIN   MAX    0
ADB-WALL    13   J    MIN    I    MIN   MAX   K      MIN   MAX    0
ADB-WALL    14   J    MIN    I    MIN   MAX   K      MIN   MAX    0
ADB-WALL    15   J    MIN    I    MIN   MAX   K      MIN   MAX    0
ADB-WALL    16   J    MIN    I    MIN   MAX   K      MIN   MAX    0
ADB-WALL    17   J    MIN    I    MIN   MAX   K      MIN   MAX    0
ADB-WALL    18   J    MIN    I    MIN   MAX   K      MIN   MAX    0
ADB-WALL    19   J    MIN    I    MIN   MAX   K      MIN   MAX    0
ADB-WALL    20   J    MIN    I    MIN   MAX   K      MIN   MAX    0
ADB-WALL    21   J    MIN    I    MIN   MAX   K      MIN   MAX    0
ADB-WALL    22   J    MIN    I    MIN   MAX   K      MIN   MAX    0
ADB-WALL    23   J    MIN    I    MIN   MAX   K      MIN   MAX    0
ADB-WALL    24   J    MIN    I    MIN   MAX   K      MIN   MAX    0
ADB-WALL    25   J    MIN    I    MIN   MAX   K      MIN   MAX    0
ADB-WALL    26   J    MIN    I    MIN   MAX   K      MIN   MAX    0
ADB-WALL    27   J    MIN    I    MIN   MAX   K      MIN   MAX    0
ADB-WALL    28   J    MIN    I    MIN   MAX   K      MIN   MAX    0
ADB-WALL    29   J    MIN    I    MIN   MAX   K      MIN   MAX    0
ADB-WALL    30   J    MIN    I    MIN   MAX   K      MIN   MAX    0
ADB-WALL    31   J    MIN    I    MIN   MAX   K      MIN   MAX    0
ADB-WALL    32   J    MIN    I    MIN   MAX   K      MIN   MAX    0
ADB-WALL    33   J    MIN    I    MIN   MAX   K      MIN   MAX    0
ADB-WALL    34   J    MIN    I    MIN   MAX   K      MIN   MAX    0
ADB-WALL    35   J    MIN    I    MIN   MAX   K      MIN   MAX    0
ADB-WALL    36   J    MIN    I    MIN   MAX   K      MIN   MAX    0
ADB-WALL    37   J    MIN    I    MIN   MAX   K      MIN   MAX    0
ADB-WALL    38   J    MIN    I    MIN   MAX   K      MIN   MAX    0
ADB-WALL    39   J    MIN    I    MIN   MAX   K      MIN   MAX    0
ADB-WALL    40   J    MIN    I    MIN   MAX   K      MIN   MAX    0
ADB-WALL    41   J    MIN    I    MIN   MAX   K      MIN   MAX    0
ADB-WALL    42   J    MIN    I    MIN   MAX   K      MIN   MAX    0
ADB-WALL    43   J    MIN    I    MIN   MAX   K      MIN   MAX    0
ADB-WALL    44   J    MIN    I    MIN   MAX   K      MIN   MAX    0
ADB-WALL    45   J    MIN    I    MIN   MAX   K      MIN   MAX    0
ADB-WALL    46   J    MIN    I    MIN   MAX   K      MIN   MAX    0
ADB-WALL    47   J    MIN    I    MIN   MAX   K      MIN   MAX    0
ADB-WALL    48   J    MIN    I    MIN   MAX   K      MIN   MAX    0
ADB-WALL    49   J    MIN    I    MIN   MAX   K      MIN   MAX    0
ADB-WALL    50   J    MIN    I    MIN   MAX   K      MIN   MAX    0
```

```
ADB-WALL    51    J    MIN    I    MIN    MAX    K    MIN    MAX    0
ADB-WALL    52    J    MIN    I    MIN    MAX    K    MIN    MAX    0
ADB-WALL    53    J    MIN    I    MIN    MAX    K    MIN    MAX    0
ADB-WALL    54    J    MIN    I    MIN    MAX    K    MIN    MAX    0
ADB-WALL    55    J    MIN    I    MIN    MAX    K    MIN    MAX    0
FARFIELD    1     J    MAX    I    MIN    MAX    K    MIN    MAX    0
FARFIELD    2     J    MAX    I    MIN    MAX    K    MIN    MAX    0
FARFIELD    3     J    MAX    I    MIN    MAX    K    MIN    MAX    0
FARFIELD    4     J    MAX    I    MIN    MAX    K    MIN    MAX    0
FARFIELD    5     J    MAX    I    MIN    MAX    K    MIN    MAX    0
FARFIELD    6     J    MAX    I    MIN    MAX    K    MIN    MAX    0
FARFIELD    7     J    MAX    I    MIN    MAX    K    MIN    MAX    0
FARFIELD    8     J    MAX    I    MIN    MAX    K    MIN    MAX    0
FARFIELD    9     J    MAX    I    MIN    MAX    K    MIN    MAX    0
FARFIELD    10    J    MAX    I    MIN    MAX    K    MIN    MAX    0
FARFIELD    11    J    MAX    I    MIN    MAX    K    MIN    MAX    0
FARFIELD    12    J    MAX    I    MIN    MAX    K    MIN    MAX    0
FARFIELD    13    J    MAX    I    MIN    MAX    K    MIN    MAX    0
FARFIELD    14    J    MAX    I    MIN    MAX    K    MIN    MAX    0
FARFIELD    15    J    MAX    I    MIN    MAX    K    MIN    MAX    0
FARFIELD    16    J    MAX    I    MIN    MAX    K    MIN    MAX    0
FARFIELD    17    J    MAX    I    MIN    MAX    K    MIN    MAX    0
FARFIELD    18    J    MAX    I    MIN    MAX    K    MIN    MAX    0
FARFIELD    19    J    MAX    I    MIN    MAX    K    MIN    MAX    0
FARFIELD    20    J    MAX    I    MIN    MAX    K    MIN    MAX    0
FARFIELD    21    J    MAX    I    MIN    MAX    K    MIN    MAX    0
FARFIELD    22    J    MAX    I    MIN    MAX    K    MIN    MAX    0
FARFIELD    23    J    MAX    I    MIN    MAX    K    MIN    MAX    0
FARFIELD    24    J    MAX    I    MIN    MAX    K    MIN    MAX    0
FARFIELD    25    J    MAX    I    MIN    MAX    K    MIN    MAX    0
FARFIELD    26    J    MAX    I    MIN    MAX    K    MIN    MAX    0
FARFIELD    27    J    MAX    I    MIN    MAX    K    MIN    MAX    0
FARFIELD    28    J    MAX    I    MIN    MAX    K    MIN    MAX    0
FARFIELD    29    J    MAX    I    MIN    MAX    K    MIN    MAX    0
FARFIELD    30    J    MAX    I    MIN    MAX    K    MIN    MAX    0
FARFIELD    31    J    MAX    I    MIN    MAX    K    MIN    MAX    0
FARFIELD    32    J    MAX    I    MIN    MAX    K    MIN    MAX    0
FARFIELD    33    J    MAX    I    MIN    MAX    K    MIN    MAX    0
FARFIELD    34    J    MAX    I    MIN    MAX    K    MIN    MAX    0
FARFIELD    35    J    MAX    I    MIN    MAX    K    MIN    MAX    0
FARFIELD    36    J    MAX    I    MIN    MAX    K    MIN    MAX    0
FARFIELD    37    J    MAX    I    MIN    MAX    K    MIN    MAX    0
FARFIELD    38    J    MAX    I    MIN    MAX    K    MIN    MAX    0
FARFIELD    39    J    MAX    I    MIN    MAX    K    MIN    MAX    0
FARFIELD    40    J    MAX    I    MIN    MAX    K    MIN    MAX    0
FARFIELD    41    J    MAX    I    MIN    MAX    K    MIN    MAX    0
FARFIELD    42    J    MAX    I    MIN    MAX    K    MIN    MAX    0
FARFIELD    43    J    MAX    I    MIN    MAX    K    MIN    MAX    0
FARFIELD    44    J    MAX    I    MIN    MAX    K    MIN    MAX    0
FARFIELD    45    J    MAX    I    MIN    MAX    K    MIN    MAX    0
FARFIELD    46    J    MAX    I    MIN    MAX    K    MIN    MAX    0
FARFIELD    47    J    MAX    I    MIN    MAX    K    MIN    MAX    0
FARFIELD    48    J    MAX    I    MIN    MAX    K    MIN    MAX    0
FARFIELD    49    J    MAX    I    MIN    MAX    K    MIN    MAX    0
FARFIELD    50    J    MAX    I    MIN    MAX    K    MIN    MAX    0
FARFIELD    51    J    MAX    I    MIN    MAX    K    MIN    MAX    0
FARFIELD    52    J    MAX    I    MIN    MAX    K    MIN    MAX    0
```

```
FARFIELD   53  J  MAX  I  MIN  MAX  K  MIN  MAX  0
FARFIELD   54  J  MAX  I  MIN  MAX  K  MIN  MAX  0
FARFIELD   55  J  MAX  I  MIN  MAX  K  MIN  MAX  0
OUTFLOW    55  I  MAX  J  MIN  MAX  K  MIN  MAX  0
ADB-WALL    3  I  MIN  J  MIN  21   K  MIN  MAX  0
ADB-WALL    3  I  MAX  J  6    21   K  MIN  MAX  0
ADB-WALL    4  I  MIN  J  6    21   K  MIN  MAX  0
ADB-WALL    4  I  MAX  J  6    21   K  MIN  MAX  0
ADB-WALL    5  I  MIN  J  6    21   K  MIN  MAX  0
ADB-WALL    5  I  MAX  J  6    21   K  MIN  MAX  0
ADB-WALL    6  I  MIN  J  6    21   K  MIN  MAX  0
ADB-WALL    6  I  MAX  J  6    21   K  MIN  MAX  0
ADB-WALL    7  I  MIN  J  6    21   K  MIN  MAX  0
ADB-WALL    7  I  MAX  J  6    21   K  MIN  MAX  0
ADB-WALL    8  I  MIN  J  6    21   K  MIN  MAX  0
ADB-WALL    8  I  MAX  J  6    21   K  MIN  MAX  0
ADB-WALL    9  I  MIN  J  6    21   K  MIN  MAX  0
ADB-WALL    9  I  MAX  J  6    21   K  MIN  MAX  0
ADB-WALL   10  I  MIN  J  6    21   K  MIN  MAX  0
ADB-WALL   10  I  MAX  J  6    21   K  MIN  MAX  0
ADB-WALL   11  I  MIN  J  6    21   K  MIN  MAX  0
ADB-WALL   11  I  MAX  J  6    21   K  MIN  MAX  0
ADB-WALL   12  I  MIN  J  6    21   K  MIN  MAX  0
ADB-WALL   12  I  MAX  J  6    21   K  MIN  MAX  0
ADB-WALL   13  I  MIN  J  6    21   K  MIN  MAX  0
ADB-WALL   13  I  MAX  J  6    21   K  MIN  MAX  0
ADB-WALL   14  I  MIN  J  6    21   K  MIN  MAX  0
ADB-WALL   14  I  MAX  J  6    21   K  MIN  MAX  0
ADB-WALL   15  I  MIN  J  6    21   K  MIN  MAX  0
ADB-WALL   15  I  MAX  J  6    21   K  MIN  MAX  0
ADB-WALL   16  I  MIN  J  6    21   K  MIN  MAX  0
ADB-WALL   16  I  MAX  J  6    21   K  MIN  MAX  0
ADB-WALL   17  I  MIN  J  6    21   K  MIN  MAX  0
ADB-WALL   17  I  MAX  J  6    21   K  MIN  MAX  0
ADB-WALL   18  I  MIN  J  6    21   K  MIN  MAX  0
ADB-WALL   18  I  MAX  J  6    21   K  MIN  MAX  0
ADB-WALL   19  I  MIN  J  6    21   K  MIN  MAX  0
ADB-WALL   19  I  MAX  J  6    21   K  MIN  MAX  0
ADB-WALL   20  I  MIN  J  6    21   K  MIN  MAX  0
ADB-WALL   20  I  MAX  J  MIN  21   K  MIN  MAX  0
ADB-WALL   21  I  MIN  J  MIN  21   K  MIN  MAX  0
ADB-WALL   21  I  MAX  J  6    21   K  MIN  MAX  0
ADB-WALL   22  I  MIN  J  6    21   K  MIN  MAX  0
ADB-WALL   22  I  MAX  J  6    21   K  MIN  MAX  0
ADB-WALL   23  I  MIN  J  6    21   K  MIN  MAX  0
ADB-WALL   23  I  MAX  J  6    21   K  MIN  MAX  0
ADB-WALL   24  I  MIN  J  6    21   K  MIN  MAX  0
ADB-WALL   24  I  MAX  J  6    21   K  MIN  MAX  0
ADB-WALL   25  I  MIN  J  6    21   K  MIN  MAX  0
ADB-WALL   25  I  MAX  J  6    21   K  MIN  MAX  0
ADB-WALL   26  I  MIN  J  6    21   K  MIN  MAX  0
ADB-WALL   26  I  MAX  J  6    21   K  MIN  MAX  0
ADB-WALL   27  I  MIN  J  6    21   K  MIN  MAX  0
ADB-WALL   27  I  MAX  J  6    21   K  MIN  MAX  0
ADB-WALL   28  I  MIN  J  6    21   K  MIN  MAX  0
ADB-WALL   28  I  MAX  J  6    21   K  MIN  MAX  0
ADB-WALL   29  I  MIN  J  6    21   K  MIN  MAX  0
```

CUT NAME	BLK	FACE	PLACE	DIREC1	BEGIN	END	DIREC2	BEGIN	END	IN-ORDER
ADB-WALL	29	I	MAX	J	6	21	K	MIN	MAX	0
ADB-WALL	30	I	MIN	J	6	21	K	MIN	MAX	0
ADB-WALL	30	I	MAX	J	6	21	K	MIN	MAX	0
ADB-WALL	31	I	MIN	J	6	21	K	MIN	MAX	0
ADB-WALL	31	I	MAX	J	6	21	K	MIN	MAX	0
ADB-WALL	32	I	MIN	J	6	21	K	MIN	MAX	0
ADB-WALL	32	I	MAX	J	6	21	K	MIN	MAX	0
ADB-WALL	33	I	MIN	J	6	21	K	MIN	MAX	0
ADB-WALL	33	I	MAX	J	6	21	K	MIN	MAX	0
ADB-WALL	34	I	MIN	J	6	21	K	MIN	MAX	0
ADB-WALL	34	I	MAX	J	6	21	K	MIN	MAX	0
ADB-WALL	35	I	MIN	J	6	21	K	MIN	MAX	0
ADB-WALL	35	I	MAX	J	6	21	K	MIN	MAX	0
ADB-WALL	36	I	MIN	J	6	21	K	MIN	MAX	0
ADB-WALL	36	I	MAX	J	6	21	K	MIN	MAX	0
ADB-WALL	37	I	MIN	J	6	21	K	MIN	MAX	0
ADB-WALL	37	I	MAX	J	MIN	21	K	MIN	MAX	0
ADB-WALL	38	I	MIN	J	MIN	21	K	MIN	MAX	0
ADB-WALL	38	I	MAX	J	6	21	K	MIN	MAX	0
ADB-WALL	39	I	MIN	J	6	21	K	MIN	MAX	0
ADB-WALL	39	I	MAX	J	6	21	K	MIN	MAX	0
ADB-WALL	40	I	MIN	J	6	21	K	MIN	MAX	0
ADB-WALL	40	I	MAX	J	6	21	K	MIN	MAX	0
ADB-WALL	41	I	MIN	J	6	21	K	MIN	MAX	0
ADB-WALL	41	I	MAX	J	6	21	K	MIN	MAX	0
ADB-WALL	42	I	MIN	J	6	21	K	MIN	MAX	0
ADB-WALL	42	I	MAX	J	6	21	K	MIN	MAX	0
ADB-WALL	43	I	MIN	J	6	21	K	MIN	MAX	0
ADB-WALL	43	I	MAX	J	6	21	K	MIN	MAX	0
ADB-WALL	44	I	MIN	J	6	21	K	MIN	MAX	0
ADB-WALL	44	I	MAX	J	6	21	K	MIN	MAX	0
ADB-WALL	45	I	MIN	J	6	21	K	MIN	MAX	0
ADB-WALL	45	I	MAX	J	6	21	K	MIN	MAX	0
ADB-WALL	46	I	MIN	J	6	21	K	MIN	MAX	0
ADB-WALL	46	I	MAX	J	6	21	K	MIN	MAX	0
ADB-WALL	47	I	MIN	J	6	21	K	MIN	MAX	0
ADB-WALL	47	I	MAX	J	6	21	K	MIN	MAX	0
ADB-WALL	48	I	MIN	J	6	21	K	MIN	MAX	0
ADB-WALL	48	I	MAX	J	6	21	K	MIN	MAX	0
ADB-WALL	49	I	MIN	J	6	21	K	MIN	MAX	0
ADB-WALL	49	I	MAX	J	6	21	K	MIN	MAX	0
ADB-WALL	50	I	MIN	J	6	21	K	MIN	MAX	0
ADB-WALL	50	I	MAX	J	6	21	K	MIN	MAX	0
ADB-WALL	51	I	MIN	J	6	21	K	MIN	MAX	0
ADB-WALL	51	I	MAX	J	6	21	K	MIN	MAX	0
ADB-WALL	52	I	MIN	J	6	21	K	MIN	MAX	0
ADB-WALL	52	I	MAX	J	6	21	K	MIN	MAX	0
ADB-WALL	53	I	MIN	J	6	21	K	MIN	MAX	0
ADB-WALL	53	I	MAX	J	6	21	K	MIN	MAX	0
ADB-WALL	54	I	MIN	J	6	21	K	MIN	MAX	0
ADB-WALL	54	I	MAX	J	MIN	21	K	MIN	MAX	0
CUT NAME	BLK	FACE	PLACE	DIREC1	BEGIN	END	DIREC2	BEGIN	END	IN-ORDER
CUT_1	1	I	MAX	J	MIN	MAX	K	MIN	MAX	0
CUT_1	2	I	MIN	J	MIN	MAX	K	MIN	MAX	0
CUT_2	2	I	MAX	J	MIN	MAX	K	MIN	MAX	0
CUT_2	3	I	MIN	J	21	MAX	K	MIN	MAX	0

CUT_3	3	I	MAX	J	21	MAX	K	MIN	MAX	0
CUT_3	4	I	MIN	J	21	MAX	K	MIN	MAX	0
CUT_4	4	I	MAX	J	21	MAX	K	MIN	MAX	0
CUT_4	5	I	MIN	J	21	MAX	K	MIN	MAX	0
CUT_5	5	I	MAX	J	21	MAX	K	MIN	MAX	0
CUT_5	6	I	MIN	J	21	MAX	K	MIN	MAX	0
CUT_6	6	I	MAX	J	21	MAX	K	MIN	MAX	0
CUT_6	7	I	MIN	J	21	MAX	K	MIN	MAX	0
CUT_7	7	I	MAX	J	21	MAX	K	MIN	MAX	0
CUT_7	8	I	MIN	J	21	MAX	K	MIN	MAX	0
CUT_8	8	I	MAX	J	21	MAX	K	MIN	MAX	0
CUT_8	9	I	MIN	J	21	MAX	K	MIN	MAX	0
CUT_9	9	I	MAX	J	21	MAX	K	MIN	MAX	0
CUT_9	10	I	MIN	J	21	MAX	K	MIN	MAX	0
CUT_10	10	I	MAX	J	21	MAX	K	MIN	MAX	0
CUT_10	11	I	MIN	J	21	MAX	K	MIN	MAX	0
CUT_11	11	I	MAX	J	21	MAX	K	MIN	MAX	0
CUT_11	12	I	MIN	J	21	MAX	K	MIN	MAX	0
CUT_12	12	I	MAX	J	21	MAX	K	MIN	MAX	0
CUT_12	13	I	MIN	J	21	MAX	K	MIN	MAX	0
CUT_13	13	I	MAX	J	21	MAX	K	MIN	MAX	0
CUT_13	14	I	MIN	J	21	MAX	K	MIN	MAX	0
CUT_14	14	I	MAX	J	21	MAX	K	MIN	MAX	0
CUT_14	15	I	MIN	J	21	MAX	K	MIN	MAX	0
CUT_15	15	I	MAX	J	21	MAX	K	MIN	MAX	0
CUT_15	16	I	MIN	J	21	MAX	K	MIN	MAX	0
CUT_16	16	I	MAX	J	21	MAX	K	MIN	MAX	0
CUT_16	17	I	MIN	J	21	MAX	K	MIN	MAX	0
CUT_17	17	I	MAX	J	21	MAX	K	MIN	MAX	0
CUT_17	18	I	MIN	J	21	MAX	K	MIN	MAX	0
CUT_18	18	I	MAX	J	21	MAX	K	MIN	MAX	0
CUT_18	19	I	MIN	J	21	MAX	K	MIN	MAX	0
CUT_19	19	I	MAX	J	21	MAX	K	MIN	MAX	0
CUT_19	20	I	MIN	J	21	MAX	K	MIN	MAX	0
CUT_20	20	I	MAX	J	21	MAX	K	MIN	MAX	0
CUT_20	21	I	MIN	J	21	MAX	K	MIN	MAX	0
CUT_21	21	I	MAX	J	21	MAX	K	MIN	MAX	0
CUT_21	22	I	MIN	J	21	MAX	K	MIN	MAX	0
CUT_22	22	I	MAX	J	21	MAX	K	MIN	MAX	0
CUT_22	23	I	MIN	J	21	MAX	K	MIN	MAX	0
CUT_23	23	I	MAX	J	21	MAX	K	MIN	MAX	0
CUT_23	24	I	MIN	J	21	MAX	K	MIN	MAX	0
CUT_24	24	I	MAX	J	21	MAX	K	MIN	MAX	0
CUT_24	25	I	MIN	J	21	MAX	K	MIN	MAX	0
CUT_25	25	I	MAX	J	21	MAX	K	MIN	MAX	0
CUT_25	26	I	MIN	J	21	MAX	K	MIN	MAX	0
CUT_26	26	I	MAX	J	21	MAX	K	MIN	MAX	0
CUT_26	27	I	MIN	J	21	MAX	K	MIN	MAX	0
CUT_27	27	I	MAX	J	21	MAX	K	MIN	MAX	0
CUT_27	28	I	MIN	J	21	MAX	K	MIN	MAX	0
CUT_28	28	I	MAX	J	21	MAX	K	MIN	MAX	0
CUT_28	29	I	MIN	J	21	MAX	K	MIN	MAX	0
CUT_29	29	I	MAX	J	21	MAX	K	MIN	MAX	0
CUT_29	30	I	MIN	J	21	MAX	K	MIN	MAX	0
CUT_30	30	I	MAX	J	21	MAX	K	MIN	MAX	0
CUT_30	31	I	MIN	J	21	MAX	K	MIN	MAX	0
CUT_31	31	I	MAX	J	21	MAX	K	MIN	MAX	0

```
CUT_31    32    I    MIN    J    21     MAX    K    MIN    MAX    0
CUT_32    32    I    MAX    J    21     MAX    K    MIN    MAX    0
CUT_32    33    I    MIN    J    21     MAX    K    MIN    MAX    0
CUT_33    33    I    MAX    J    21     MAX    K    MIN    MAX    0
CUT_33    34    I    MIN    J    21     MAX    K    MIN    MAX    0
CUT_34    34    I    MAX    J    21     MAX    K    MIN    MAX    0
CUT_34    35    I    MIN    J    21     MAX    K    MIN    MAX    0
CUT_35    35    I    MAX    J    21     MAX    K    MIN    MAX    0
CUT_35    36    I    MIN    J    21     MAX    K    MIN    MAX    0
CUT_36    36    I    MAX    J    21     MAX    K    MIN    MAX    0
CUT_36    37    I    MIN    J    21     MAX    K    MIN    MAX    0
CUT_37    37    I    MAX    J    21     MAX    K    MIN    MAX    0
CUT_37    38    I    MIN    J    21     MAX    K    MIN    MAX    0
CUT_38    38    I    MAX    J    21     MAX    K    MIN    MAX    0
CUT_38    39    I    MIN    J    21     MAX    K    MIN    MAX    0
CUT_39    39    I    MAX    J    21     MAX    K    MIN    MAX    0
CUT_39    40    I    MIN    J    21     MAX    K    MIN    MAX    0
CUT_40    40    I    MAX    J    21     MAX    K    MIN    MAX    0
CUT_40    41    I    MIN    J    21     MAX    K    MIN    MAX    0
CUT_41    41    I    MAX    J    21     MAX    K    MIN    MAX    0
CUT_41    42    I    MIN    J    21     MAX    K    MIN    MAX    0
CUT_42    42    I    MAX    J    21     MAX    K    MIN    MAX    0
CUT_42    43    I    MIN    J    21     MAX    K    MIN    MAX    0
CUT_43    43    I    MAX    J    21     MAX    K    MIN    MAX    0
CUT_43    44    I    MIN    J    21     MAX    K    MIN    MAX    0
CUT_44    44    I    MAX    J    21     MAX    K    MIN    MAX    0
CUT_44    45    I    MIN    J    21     MAX    K    MIN    MAX    0
CUT_45    45    I    MAX    J    21     MAX    K    MIN    MAX    0
CUT_45    46    I    MIN    J    21     MAX    K    MIN    MAX    0
CUT_46    46    I    MAX    J    21     MAX    K    MIN    MAX    0
CUT_46    47    I    MIN    J    21     MAX    K    MIN    MAX    0
CUT_47    47    I    MAX    J    21     MAX    K    MIN    MAX    0
CUT_47    48    I    MIN    J    21     MAX    K    MIN    MAX    0
CUT_48    48    I    MAX    J    21     MAX    K    MIN    MAX    0
CUT_48    49    I    MIN    J    21     MAX    K    MIN    MAX    0
CUT_49    49    I    MAX    J    21     MAX    K    MIN    MAX    0
CUT_49    50    I    MIN    J    21     MAX    K    MIN    MAX    0
CUT_50    50    I    MAX    J    21     MAX    K    MIN    MAX    0
CUT_50    51    I    MIN    J    21     MAX    K    MIN    MAX    0
CUT_51    51    I    MAX    J    21     MAX    K    MIN    MAX    0
CUT_51    52    I    MIN    J    21     MAX    K    MIN    MAX    0
CUT_52    52    I    MAX    J    21     MAX    K    MIN    MAX    0
CUT_52    53    I    MIN    J    21     MAX    K    MIN    MAX    0
CUT_53    53    I    MAX    J    21     MAX    K    MIN    MAX    0
CUT_53    54    I    MIN    J    21     MAX    K    MIN    MAX    0
CUT_54    54    I    MAX    J    21     MAX    K    MIN    MAX    0
CUT_54    55    I    MIN    J    MIN   MAX    K    MIN    MAX    0
CUT_55     4    I    MAX    J    MIN    6     K    MIN    MAX    0
CUT_55     5    I    MIN    J    MIN    6     K    MIN    MAX    0
CUT_56     5    I    MAX    J    MIN    6     K    MIN    MAX    0
CUT_56     6    I    MIN    J    MIN    6     K    MIN    MAX    0
CUT_57     6    I    MAX    J    MIN    6     K    MIN    MAX    0
CUT_57     7    I    MIN    J    MIN    6     K    MIN    MAX    0
CUT_58     7    I    MAX    J    MIN    6     K    MIN    MAX    0
CUT_58     8    I    MIN    J    MIN    6     K    MIN    MAX    0
CUT_59     8    I    MAX    J    MIN    6     K    MIN    MAX    0
CUT_59     9    I    MIN    J    MIN    6     K    MIN    MAX    0
```

CUT_60	9	I	MAX	J	MIN	6	K	MIN	MAX	0
CUT_60	10	I	MIN	J	MIN	6	K	MIN	MAX	0
CUT_61	10	I	MAX	J	MIN	6	K	MIN	MAX	0
CUT_61	11	I	MIN	J	MIN	6	K	MIN	MAX	0
CUT_62	11	I	MAX	J	MIN	6	K	MIN	MAX	0
CUT_62	12	I	MIN	J	MIN	6	K	MIN	MAX	0
CUT_63	12	I	MAX	J	MIN	6	K	MIN	MAX	0
CUT_63	13	I	MIN	J	MIN	6	K	MIN	MAX	0
CUT_64	13	I	MAX	J	MIN	6	K	MIN	MAX	0
CUT_64	14	I	MIN	J	MIN	6	K	MIN	MAX	0
CUT_65	14	I	MAX	J	MIN	6	K	MIN	MAX	0
CUT_65	15	I	MIN	J	MIN	6	K	MIN	MAX	0
CUT_66	15	I	MAX	J	MIN	6	K	MIN	MAX	0
CUT_66	16	I	MIN	J	MIN	6	K	MIN	MAX	0
CUT_67	16	I	MAX	J	MIN	6	K	MIN	MAX	0
CUT_67	17	I	MIN	J	MIN	6	K	MIN	MAX	0
CUT_68	17	I	MAX	J	MIN	6	K	MIN	MAX	0
CUT_68	18	I	MIN	J	MIN	6	K	MIN	MAX	0
CUT_69	18	I	MAX	J	MIN	6	K	MIN	MAX	0
CUT_69	19	I	MIN	J	MIN	6	K	MIN	MAX	0
CUT_70	19	I	MAX	J	MIN	6	K	MIN	MAX	0
CUT_70	20	I	MIN	J	MIN	6	K	MIN	MAX	0
CUT_71	21	I	MAX	J	MIN	6	K	MIN	MAX	0
CUT_71	22	I	MIN	J	MIN	6	K	MIN	MAX	0
CUT_72	22	I	MAX	J	MIN	6	K	MIN	MAX	0
CUT_72	23	I	MIN	J	MIN	6	K	MIN	MAX	0
CUT_73	23	I	MAX	J	MIN	6	K	MIN	MAX	0
CUT_73	24	I	MIN	J	MIN	6	K	MIN	MAX	0
CUT_74	24	I	MAX	J	MIN	6	K	MIN	MAX	0
CUT_74	25	I	MIN	J	MIN	6	K	MIN	MAX	0
CUT_75	25	I	MAX	J	MIN	6	K	MIN	MAX	0
CUT_75	26	I	MIN	J	MIN	6	K	MIN	MAX	0
CUT_76	26	I	MAX	J	MIN	6	K	MIN	MAX	0
CUT_76	27	I	MIN	J	MIN	6	K	MIN	MAX	0
CUT_77	27	I	MAX	J	MIN	6	K	MIN	MAX	0
CUT_77	28	I	MIN	J	MIN	6	K	MIN	MAX	0
CUT_78	28	I	MAX	J	MIN	6	K	MIN	MAX	0
CUT_78	29	I	MIN	J	MIN	6	K	MIN	MAX	0
CUT_79	29	I	MAX	J	MIN	6	K	MIN	MAX	0
CUT_79	30	I	MIN	J	MIN	6	K	MIN	MAX	0
CUT_80	30	I	MAX	J	MIN	6	K	MIN	MAX	0
CUT_80	31	I	MIN	J	MIN	6	K	MIN	MAX	0
CUT_81	31	I	MAX	J	MIN	6	K	MIN	MAX	0
CUT_81	32	I	MIN	J	MIN	6	K	MIN	MAX	0
CUT_82	32	I	MAX	J	MIN	6	K	MIN	MAX	0
CUT_82	33	I	MIN	J	MIN	6	K	MIN	MAX	0
CUT_83	33	I	MAX	J	MIN	6	K	MIN	MAX	0
CUT_83	34	I	MIN	J	MIN	6	K	MIN	MAX	0
CUT_84	34	I	MAX	J	MIN	6	K	MIN	MAX	0
CUT_84	35	I	MIN	J	MIN	6	K	MIN	MAX	0
CUT_85	35	I	MAX	J	MIN	6	K	MIN	MAX	0
CUT_85	36	I	MIN	J	MIN	6	K	MIN	MAX	0
CUT_86	36	I	MAX	J	MIN	6	K	MIN	MAX	0
CUT_86	37	I	MIN	J	MIN	6	K	MIN	MAX	0
CUT_87	38	I	MAX	J	MIN	6	K	MIN	MAX	0
CUT_87	39	I	MIN	J	MIN	6	K	MIN	MAX	0
CUT_88	39	I	MAX	J	MIN	6	K	MIN	MAX	0

```
CUT_88    40  I  MIN  J  MIN  6  K  MIN  MAX  0
CUT_89    40  I  MAX  J  MIN  6  K  MIN  MAX  0
CUT_89    41  I  MIN  J  MIN  6  K  MIN  MAX  0
CUT_90    41  I  MAX  J  MIN  6  K  MIN  MAX  0
CUT_90    42  I  MIN  J  MIN  6  K  MIN  MAX  0
CUT_91    42  I  MAX  J  MIN  6  K  MIN  MAX  0
CUT_91    43  I  MIN  J  MIN  6  K  MIN  MAX  0
CUT_92    43  I  MAX  J  MIN  6  K  MIN  MAX  0
CUT_92    44  I  MIN  J  MIN  6  K  MIN  MAX  0
CUT_93    44  I  MAX  J  MIN  6  K  MIN  MAX  0
CUT_93    45  I  MIN  J  MIN  6  K  MIN  MAX  0
CUT_94    45  I  MAX  J  MIN  6  K  MIN  MAX  0
CUT_94    46  I  MIN  J  MIN  6  K  MIN  MAX  0
CUT_95    46  I  MAX  J  MIN  6  K  MIN  MAX  0
CUT_95    47  I  MIN  J  MIN  6  K  MIN  MAX  0
CUT_96    47  I  MAX  J  MIN  6  K  MIN  MAX  0
CUT_96    48  I  MIN  J  MIN  6  K  MIN  MAX  0
CUT_97    48  I  MAX  J  MIN  6  K  MIN  MAX  0
CUT_97    49  I  MIN  J  MIN  6  K  MIN  MAX  0
CUT_98    49  I  MAX  J  MIN  6  K  MIN  MAX  0
CUT_98    50  I  MIN  J  MIN  6  K  MIN  MAX  0
CUT_99    50  I  MAX  J  MIN  6  K  MIN  MAX  0
CUT_99    51  I  MIN  J  MIN  6  K  MIN  MAX  0
CUT_100   51  I  MAX  J  MIN  6  K  MIN  MAX  0
CUT_100   52  I  MIN  J  MIN  6  K  MIN  MAX  0
CUT_101   52  I  MAX  J  MIN  6  K  MIN  MAX  0
CUT_101   53  I  MIN  J  MIN  6  K  MIN  MAX  0
CUT_102   53  I  MAX  J  MIN  6  K  MIN  MAX  0
CUT_102   54  I  MIN  J  MIN  6  K  MIN  MAX  0
CUT_103    3  I  MAX  J  MIN  6  K  MIN  MAX  0
CUT_103    4  I  MIN  J  MIN  6  K  MIN  MAX  0
```

APPENDIX B.

FORTRAN DRAG FORCE DECOMPOSITION

POST PROCESSING CODE

```fortran
      program loads_post_gated_52_baseline
c
      parameter(icav=55)
      implicit double precision (a-h,o-z)
      dimension rpsumcav(icav),rpsumtot(icav),
     1vissum(icav),vissumtot(icav)
      dimension xsave(icav)
c
c
      open(7,file='vulcan.loads.tec')
      rewind(7)
c
c
      rpsum=0.
      vis=0.
c
c
      do 1000 i=1,55
c
      irun=20
c
      if(i.eq.1.or.i.eq.2) irun=20
      if(i.eq.55) irun=20
      iside=3
      if(i.eq.1.or.i.eq.2.or.i.eq.55) iside=1
c
      rpsumcav(i)=0.
      vissum(i)=0.
c
      do 1444 jj=1,iside
c
      jstart=6
c
      if(jj.eq.1) jstart=1
      if(i.eq.3.and.jj.eq.2) jstart=1
      if(i.eq.54.and.jj.eq.3) jstart=1
      if(i.eq.20.and.jj.eq.3) jstart=1
      if(i.eq.21.and.jj.eq.2) jstart=1
      if(i.eq.37.and.jj.eq.3) jstart=1
      if(i.eq.38.and.jj.eq.2) jstart=1
      read(7,*) idum1,idum2,idum3,idum4
      do 999 j=jstart,irun
c
      read(7,*) xdum1,xdum2,xdum3,xdum4,rp,xdum6,xdum7,
     1xdum8,xdum9
      rpsumcav(i)=rpsumcav(i)+rp
      vissum(i)=vissum(i)+xdum7
 999  continue
c
 1444 continue
c
      rpsum=rpsum+rpsumcav(i)
      vis=vis+vissum(i)
      rpsumtot(i)=rpsum
      vissumtot(i)=vis
      xsave(i)=xdum1
 1000 continue
```

```
c
      do 2000 i=1,55
      write(8,*) i,xsave(i),rpsumcav(i),vissum(i),
     1rpsumtot(i),vissumtot(i)
 2000 continue
c
      stop
      end
```

BIBLIOGRAPHY

[1]   Lang, A.W., Motta, P., Hidalgo, P., Westcott, M., "Bristled Shark Skin: A Microgeometry for Boundary Layer Control," *Bioinspiration & Biomimetics*, 2008.

[2]   Lang, A.W., Hildalgo, P., "Cavity Flow Characterization of the Bristled Shark Skin Microgeometry," AIAA Paper 2009-1107, January 2009.

[3]   Hao, P., Wong, C., Yao, Z., Zhu, K., "Laminar Drag Reduction in Hydrophobic Microchannels," *Chemical Engineering Technology*, Vol. 32, No. 6, 2008, pp. 912-918.

[4]   Walsh, M.J., "Riblets." *Viscous Drag Reduction in Boundary Layers*, edited by D.M. Bushnell and J.N. Hefner, Progress in Astronautics and Aeronautics, Vol. 123, pp. 203-261.

[5]   Duan, L., Choudhari, M.M., "Effects of Riblets on Skin Friction and Heat Transfer in High-Speed Turbulent Boundary Layers," AIAA Paper 2012-1108.

[6]   Hwang, D.P., "An Experimental Study of Turbulent Skin Friction Reduction in Supersonic Flow Using a Microblowing Technique," NASA TM-209632, December 1999.

[7]   Zhuang, Z., Alvi, F.S., Alkislar, M.B., Shih, C., "Supersonic Cavity Flows and Their Control," *AIAA Journal*, Vol. 44, No. 9, September 2006, pp. 2118-2128.

[8]   Lazar, E., Elliott, G., Glumac, N., "Control of the Shear Layer Above a Supersonic Cavity Using Energy Deposition," *AIAA Journal*, Vol. 46, No. 12, December 2008, pp. 2987-2997.

[9]   Wang, C.Y., "Flow Over A Surface with Parallel Grooves," *Physics of Fluids*, Vol. 15, No. 5, May 2003, 1114-1121.

[10]   Huang, P.C., Vafai, K., "Flow and Heat Transfer Control Over and External Surface Using a Porous Block Array Arrangement," *International Journal of Heat Mass Transfer¸* Vol. 36, No. 16, 1993, pp. 4019-4032.

[11]   Hwang, D.P., "Experimental Study of Characteristics of Micro-Hole Porous Skins for Turbulent Skin Friction Reduction," *ICAS Congress*, 2002, pp. 2101.1-2101-9.

[12]   Ekoto, I.W., Bowersox, R.D.W., Beutner, T., Goss, L., "Supersonic Boundary Layers with Periodic Surface Roughness," *AIAA Journal*, Vol. 46, No. 2, February 2008, pp. 486-497.

[13]   Lang, A.W., Melnick, M.B., "Momentum Increase in Wall Adjacent Flow Via Hexagonal Embedded Cavities," AIAA Paper 2010-914, January 2010.

[14]   Lang, A.W, *United States Patent*, *US 2011/0274875 A1*, November 10, 2011.

[15]   Gatski, T.B., Grosch, C.E., "Embedded Cavity Drag in Steady Laminar Flow," *AIAA Journal*, Vol. 23, No. 7, July 1985, pp. 1028-1037.

[16]   Umazume et al., *United States Patent, US 6,363,972 B1*, April 2, 2002.

[17]   Madi Arous, F., Mataoui, A., Bouahmed, Z., "Influence of Upstream Flow Characteristics on the Reattachment Phenomenon in Shallow Cavities," *Thermal Science*, Vol. 15, No. 3, 2011, pp. 721-734.

[18]   Lang, A.W., Hidalgo, P., "Boundary Layer Formation Over D-Type Roughness Geometries," AIAA Paper 2008-506, January 2008.

[19]   Leibenguth, C.M., "Drag Reduction Over a Low Reynolds Number Cavity Surface," Master's Thesis, Department of Aerospace Engineering, University of Alabama, 2012.

[20]   http://vulcan-cfd.larc.nasa.gov/, VULCAN Home Page, November 2010.

[21]   Menter, F.R., "Two-Equation Eddy-Viscosity Turbulence Models for Engineering Applications," *AIAA Journal*, Vol. 32, No. 8, August 1994, pp. 1598-1605.

[22]   Liggett, N.D., Smith, M.J., "Cavity Flow Assessment Using Advanced Turbulence Modeling," AIAA Paper 2010-1200, January 2010.

[23]   Schetz, J.A., "Boundary Layer Analysis," Prentice Hall, 1993.

[24]   Schlichting, H., "Boundary Layer Theory," McGraw-Hill, 1960.

[25]   Anderson, J.D., "Modern Compressible Flow," McGraw-Hill, 1990.

VITA

Thomas Ryan Rehmeier was born November 14, 1989 in Saint Louis, Missouri. He grew up in Jefferson City, Missouri and attended Jefferson City High School where he graduated Salutatorian in 2008. Thereafter he began attending Missouri University of Science and Technology in Rolla, Missouri graduating Summa Cum Laude in May 2012 with a Bachelor of Science degree in Aerospace Engineering. Thomas remained in Rolla for graduate school, working under Dr. D.W. Riggins. During that time he was a Graduate Teaching Assistant for Introduction to Engineering Design. He began working for The Boeing Company in Saint Louis, Missouri as an Aerodynamics Engineer in May 2013 and graduated with a Master of Science in Aerospace Engineering in August 2013.

During his time in Rolla, Thomas served as President of the S&T Student Chapter of the American Institute of Aeronautics and Astronautics (AIAA) and was member of the honor societies of Sigma Gamma Tau, Tau Beta Pi, Kappa Mu Epsilon, and Phi Kappa Phi.